Self-Powered Infrared Detection in Low-Dimensional Carbon Assemblies

by

Mingyu Zhang

A thesis

presented to the University of Waterloo

in fulfillment of the

thesis requirement for the degree of

Doctor of Philosophy

in

Systems Design Engineering

Waterloo, Ontario, Canada, 2019

Examining Committee Members

External: Nazir Kherani
Professor, Electrical and Computer Engineering
University of Toronto

Internal-external: Dayan Ban
Professor, Electrical and Computer Engineering
University of Waterloo

Internal-external: Safieddin Safavi-Naeini
Professor, Electrical and Computer Engineering
University of Waterloo

Internal: Ning Jiang
Assistant Professor, Systems Design Engineering
University of Waterloo

Supervisor: John T.W. Yeow
Professor, Systems Design Engineering
University of Waterloo

Author's Declaration

I hereby declare that I am the sole author of this thesis. This is a true copy of the thesis, including any required final revisions, as accepted by my examiners.

I understand that my thesis may be made electronically available to the public.

Abstract

Room-temperature mid-infrared photodetection meet upcoming demands including real-time health condition monitoring, low-cost industrial inspection and distributive sensing for Internet-of-Things. Photo-thermoelectric (PTE) effect is a bandgap limitless photodetection mechanism which utilizes photons induced thermoelectric effect at material interfaces. The 1/f noise and shot noise in dark current can be significantly reduced in a zero-biased PTE detector. Carbon nanotubes (CNTs) and graphene are emerging low-dimensional materials with excellent PTE properties. Besides the strong and broadband light-matter interaction, their increased electrical to thermal conductivity ratio σ/κ and electron density-of-states dependence on energy $dg(E)/dE$ also lead to enhanced thermoelectric conversion efficiency.

In this thesis, we present two self-powered PTE detection architectures. In the first one, vertical photo-thermoelectric effect of an anti-reflecting carbon nanotube forest (CNTF) is employed in a broadband mid-infrared detector. 99.4% average reflection suppression in the CNTF at 2.5~25 μm spectral range enables responsivity of 6 V W^{-1} and detectivity of 2.2×10^{7} cm $Hz^{1/2}$ W^{-1} under very weak illumination power, rendering sensitive weak infrared photodetection in real life. Top-electrode material, thickness and patterns are systematically studied related to the PTE response, and further improvement is possible by increasing the CNTF height and reducing the photosensitive area. In the second architecture, CNTs/Poly vinyl alcohol (PVA) composite based planar photodetector with asymmetric metallic electrodes is investigated. PTE voltage response is optimized via

mixing 25 wt.% CNTs into PVA matrix attributed to the enhanced phonon scattering at CNTs/PVA interfaces. Moreover, crystallization of PVA around CNTs networks contributes to a rather stable photoresponse (variation < 4 %) under significant bending down to a 3.5 mm radius. This flexible, wearable photodetector also proves preliminary passive imaging of human body radiation. Finally, a unique and facile fabrication technique is demonstrated for the integration of a flexible, semi-transparent photodetector based on graphene nanoplatelets/PEDOT: PSS composite. This photodetector exhibits enhanced PTE response, high flexibility, and good optical transparency at a low loading of graphene.

Acknowledgement

First, I would like to express my gratitude to my supervisor, Prof. John Yeow, for giving me the opportunity to join his lab, and the complete trust and freedom to let me work on the research project I am fully interested in. Without your financial support for everything and the great resources, all of my work would never be possible. I have also learnt from you always planning work ahead of time and how to think critically as an engineer and PhD. I truly appreciate Prof. Dayan Ban for letting me use the Infrared and THz light sources in his lab, your generosity and kindness are what I do not take for granted. I would also like to thank the other members of my committee - Prof. Safieddin Safavi-Naeini and Prof. Ning Jiang for being there when I need help. I sincerely thank Prof. Nazir Kherani for agreeing to be the external examiner for my defense.

I would like to thank the amazing Quantum NanoFab team Dr. Nathan Nelson-Fitzpatrick, Dr. Greg Holloway, and Dr. Lino Eugene. You are so knowledgeable and always being supportive with my cleanroom work. Nathan, you have been a great mentor to me since I knew nothing about cleanroom fabrication. Whenever I meet with hard problems, I can always get the most detailed suggestions from you in the first time.

To my colleagues, I am always reminded how lucky I am to meet the most helpful and adorable you guys. Dr. Fred Sun, thank you for helping me settled in the lab in the beginning. As our lab manager, you make me understand what an excellent researcher and engineer means. Your knowledge in electronics and electricity is incredible, and you constantly brought up with brilliant short-cuts to my engineering problems. Dr. Albert

Chen, thank you for often taking to me about my research and life in your break time, and teaching me how to socialize and deal with people in a new culture. I always owe you a cup of coffee for that. Dr. Siyuan Chen, thanks for being a nice colleague and good friend to me whenever I am in need of help, and I won't forget those hard days we work together for the radiation shielding project. I would like to thank Chen Chen and Zhou Zheng for doing SEM characterizations for me. It is those chats, jokes, and laughers with you that has added so much fun in my daily PhD life. Eli, even though you have not been here for long, I enjoyed chatting with you during work breaks. I would like to thank other lab members Limin, Nash, Champika, Yibei, Zhenhao, Yunhan (apologies to those whose names I might have missed), and some friends in other lab, Yue, Xiaoliang, Chao, Demin, Penghui, for the help and support in the journey with you.

To my parents, thank you for raising me up and teaching me to be a good person. Without your unconditional love and support all these years, anything would not be possible in my life.

2019.7.6, Niagara Falls

Mingyu Zhang

Table of Contents

List of Tables

List of Figures

Chapter 1 Introduction

1.1 Contribution and thesis organization

My first contribution is having developed a highly flexible, polymer based mid-infrared photodetector with quite stable photoresponse under significant bending deformation. The core material (CNTs/PVA composite) of this detector is manufactured by solution processes and the electrodes are patterned by low-cost non-lithographic methods. An optimized photoresponse is found in propriate CNTs loading and room temperature imaging of passive human radiation from fingers have been achieved.

My second contribution is having created a novel photo-thermoelectric detection architecture by integrating a broadband anti-reflection blackbody absorber. 99.4% reflection suppression is observed in the self-assembled carbon nanotubes forest (CNTF) in 2.5~25 μm spectral range and produces an unoptimized photo detectivity of 2.2×10^{7} cm $Hz^{1/2}$ W^{-1} with non-lithographic fabrication methods. This detector architecture exhibits exceptional sensitivity towards weak, unfocused, and broadband infrared illumination as low as 6.8 μW mm^{-2} akin to realistic world. The material, thickness, and pattern of the top-electrode layer are systematically investigated regarding the PTE effect, and further improvement is demonstrated possible by increasing CNTF height and decreasing the photo-sensitive area.

My third contribution is having developed a flexible and semi-transparent polymer based mid-infrared detector. A low loading of graphene nanoplatelets (3 wt.%) within the

PEDOT: PSS matrix has not only contributed to an improved photo detectivity 1.4×10^{7} cm $Hz^{1/2}$ W^{-1} compared to our first generation - CNTs/PVA composite, but also yielded a high optical transparency of the device with thinner composite film and electrodes. The strong interaction between graphene and PEDOT: PSS leads to the low graphene loading and the good flexibility in the composite film. This self-powered, low-cost, flexible and semitransparent detectors could find applications in wearable technologies and autonomous driving assistants.

Below is a list of refereed journal publications where I am the primary author. In these work, I am responsible for all the designs, fabrications, measurements, data analysis, and manuscript writing. The co-authors have helped to review the manuscript and provided revision advices.

1. Mingyu Zhang, and John Yeow, "Nanotechnology-Based Terahertz Biological Sensing: A review of its current state and things to come," *IEEE Nanotechnology Magazine* 10 (3), 30-38.
2. Mingyu Zhang, and John Yeow, "Flexible Polymer–Carbon Nanotube Composite with High-Response Stability for Wearable Thermal Imaging," *ACS applied materials & interfaces*, 10 (31), 26604-26609.
   (This work is presented in Chapter 4.)
3. Mingyu Zhang, Dayan Ban, and John Yeow, "Large-area and Broadband Thermoelectric Infrared Detection in A Carbon Nanotube Black-body Absorber," Revised and re-submitted to *Nature Communications*.
   (This work is presented in Chapter 3.)
4. Mingyu Zhang, and John Yeow, "A Flexible, Scalable, and Self-powered Mid-infrared Detector based on Transparent PEDOT: PSS/Graphene Composite", To be submitted to *Carbon*.
   (This work is presented in Chapter 5.)

This thesis will be presented as follows. Chapter 1 introduces the light absorbing materials used in my work - CNTs, graphene, and their polymer composites, the utilized photodetection mechanism - photo-thermoelectric effect (including the advancements of using low-dimensional materials), and the review of different mid-wave infrared (MWIR, 3–5 μm) and long-wave infrared (LWIR, 8–12 μm) photodetectors as well as discussions on the noise. Chapter 2 provides the synthesis methods and characterization results of CNTF, CNTs/PVA composite, and PEDOT: PSS/graphene composite. Chapter 3 presents the photo-thermoelectric architecture based on the vertically aligned anti-reflecting carbon nanotubes forest. The investigations on the top-electrode layer thickness, material, patterns have been discussed. The further photoresponse improvement is also indicated by optimizing the physical dimensions of CNTF. Chapter 4 presents the development and photoresponse characterization of CNTs/PVA composted based detectors in terms of CNTs content, composite channel length and input power density. The detector bending properties are investigated and room temperature passive imaging of human body has been demonstrated. Chapter 5 describes the characterizations of PEDOT: PSS/graphene composite based detectors. The photoresponse correlations with graphene nanoplatelets loading and composite film thickness are revealed. Bending properties and optical transparency results have been included and practical applications of as-fabricated detectors are shown. Chapter 6 summarizes the achievements of all works and proposes future works.

1.2 Introduction to low-dimensional carbons

Carbon, congener element of silicon, has appealed great attention in recent decades since the discovery of its low-dimensional allotropes - fullerene (0-D), carbon nanotube (1-D), and graphene (2-D) in 1985, 1991,[1] and 2004,[2] respectively. Low-dimensional carbon assemblies exhibit a variety of superior properties beyond traditional materials such as the exceptional electrical conductivity, the excellent mechanical strength,[3] the high thermal conductivity,[4] and good chemical stability.

1.2.1 Graphene

As the pioneer of 2D materials, graphene is typically referred as the single (0.34 nm thick) or few layers hexagonal carbon atoms exfoliated from graphite. Due to the unique lattice structure, electrons in the delocalized π orbital can move freely as massless Dirac Fermions similar to light waves,[5] leading to an extremely high carrier mobility in theory (~15,000 $cm^2 V^{-1} s^{-1}$). Single-layer graphene exhibits semi-metallic property because its conduction band touches the valence band at the Dirac point (as shown in Figure 1-1b), creating the zero-bandgap structure. This property also extends the light absorption spectrum of graphene into a very broad range - from the short-wavelength ultraviolet to the long-wavelength range beyond terahertz and microwaves. As the number of graphite layers increases, or as the lateral physical dimension decreases to the nanoscale, graphene shows a gradually opened bandgap and starts to behave like a semiconductor.

a **b**

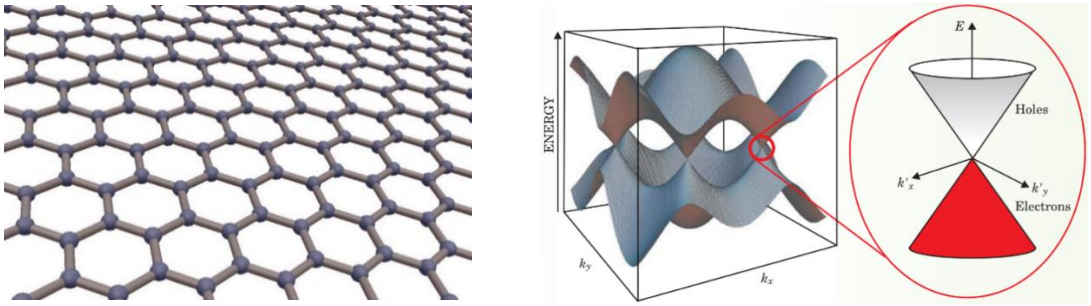

Figure 1-1. a, Graphene sketch. **b**, Energy dispersion diagram of graphene. Figure adapted from ref. [6].

The extraordinary room-temperature carrier mobility (for both electrons and holes in intrinsic graphene),[7] the high thermal conductivity ~3000 W m K^{-1}, the excellent Young's modulus ~1 TPa,[8] the ideal optical transparency ~97.8%, and the availability of being doped via simple chemical or electrical techniques have made graphene quite promising in future electronic and optoelectronic applications, possibly including transparent conductors, solar cells, light emitting diodes, photodetectors, saturable absorbers and ultrafast lasers, touch screens, flexible smart windows, etc. as shown in Figure 1-2.[9]

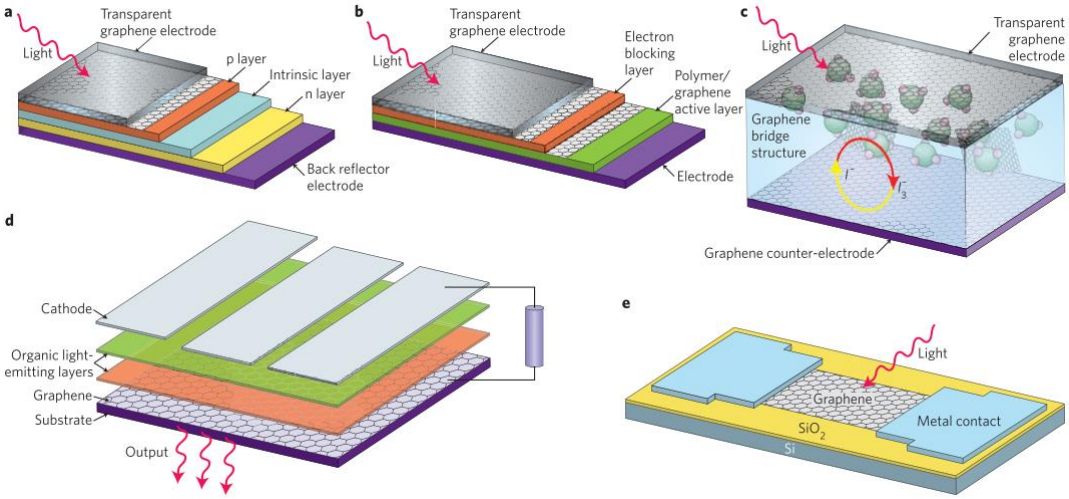

Figure 1-2. Graphene based optoelectronic devices. **a-c**, Schematics of inorganic, organic, and dye-sensitized solar cells. **d**, Schematic of an organic light emitting diode. **e**, Schematic of a photodetector.[9]

1.2.2 Carbon Nanotubes

Carbon nanotubes (CNTs) can be regarded as the cylinder structure rolled up from a graphene layer along a specific axis. Therefore, CNTs share many similar physical properties with graphene. CNTs typically consist of one rolled-up graphite wall (single-walled CNTs, or SWNTs) or several coaxial graphite walls (multi-walled CNTs, or MWNTs) with the total diameter ranging from a few nanometers to a hundred nanometers. The electrical properties of CNTs are determined by the chirality (the way graphene layer is rolled up) and the tube diameter. As shown in Figure 1-3a, the charity of CNTs can be determined by $\vec{C}_k = n\vec{a}_1 + m\vec{a}_2$. If $n = m$, the CNTs are referred as armchair type (Figure 1-3b) where relatively straight electron transporting paths exist along the tube axis which enable a high electrical conductivity. If $m = 0$, the CNTs are referred as zigzag type (Figure 1-3c), which are less conductive because the electron transport paths are generally more

twisted. CNTs are found to exhibit metallic behavior only when $(n-m)/3$ is an integer. Otherwise, CNTs are semiconductors with the bandgap inversely proportional to the overall diameter.[10] Statistically, 1/3 portion of the all the carbon nanotubes are metallic and 2/3 portion of the carbon nanotubes are semiconducting (with bandgaps of 0~2 eV). MWNTs are therefore mostly metallic because some of these tube walls could be metallic.

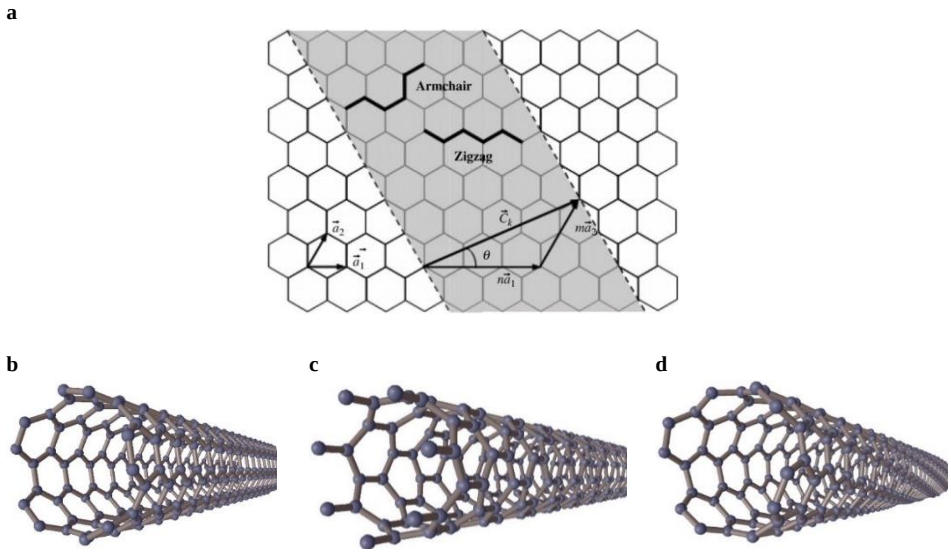

Figure 1-3. a, Schematic diagram of the chiral vector and the chiral angle.[11] **b-d**, Sketch of carbon nanotubes armchair type, zigzag type, and chiral type.

Theoretical thermal conductivity of individual carbon nanotube is κ = 6600 W m^{-1} K^{-1}.[12] But due to the presence of bundling effect and defects, chemical vapor deposition synthesized CNTs bundle or sheet usually has a thermal conductivity of $\kappa_{\parallel}$ = 50~200 W m^{-1} K^{-1} along tube axis, and the ratio of $\kappa_{\parallel}/\kappa_{\perp}$ is in the range of 3~30 varied with tube interspace and misalignment.[13], [14] The experimentally measured electrical

conductivity varies with the tube density and defect degrees. The resistance of aligned CNTs are found to be ten to hundreds of Ohms/square.[13]–[15] The electron mobility of CNTs differs significantly with the morphologies and fabrication methods, as shown in Figure 1-4. By virtue of the high electrical conductivity, carrier mobility, and strong light absorption, a variety of electronic and optoelectronic devices have been developed based on CNTs. CNTs have been utilized as the light absorbing[16], [17] and electrode materials[18] in new-generation solar cells, as the conducing channel material in field-effect transistors,[19], [20] or as molecules absorbing and electronic actuating material in chemical and biological sensors.[21], [22]

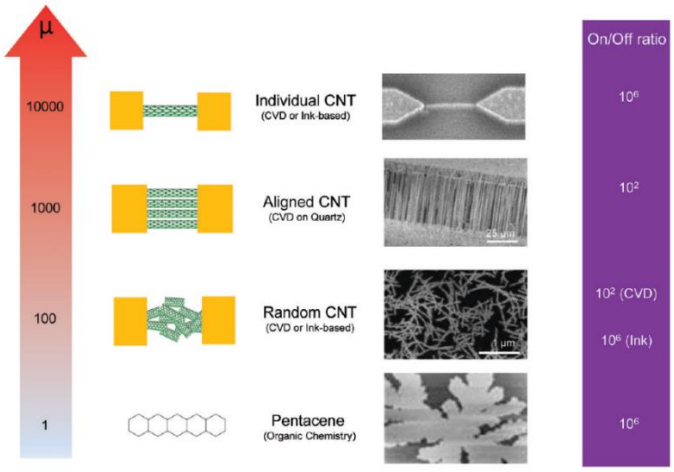

Figure 1-4. The mobility and on/off ratio trends in CNTs based transistors due to the different morphologies and fabrication techniques.[23]

1.2.3 Carbon-polymer nanocomposites

The excellent electrical, thermal and mechanical properties of CNTs and graphene we talk about are mostly in the microscopic scale, i.e. per unit volume. Therefore, it requires propriate assembling strategies to successfully translate their outstanding nanoscale

properties into macroscale performance that can be utilized in realistic applications. One of the widely adopted strategies is to combine CNTs and graphene with other materials in the form of alloys, blends, composites or hybrid materials. The idea of incorporating CNTs or graphene as fillers into a variety of polymer matrices have greatly advanced the development of nanomaterials by introducing facile and low-cost processing of conventional polymers into the material production.[24]–[26]

A composite consists of two material components: the filler and the matrix. While CNTs and graphene with nano-/micro- domains serve as the fillers, the matrix materials could be various polymer materials: the electrically conductive polymers such as poly(3,4-ethylenedioxythiophene) polystyrene sulfonate (PEDOT:PSS),[27]–[29] Polyaniline (PANI),[30] or the insolating polymers such as poly(vinyl acetate) (PVAc),[31] poly (methyl methacrylate) (PMMA),[32] poly vinyl alcohol (PVA),[33], [34] poly (vinylidene fluoride) (PVDF),[35] etc.

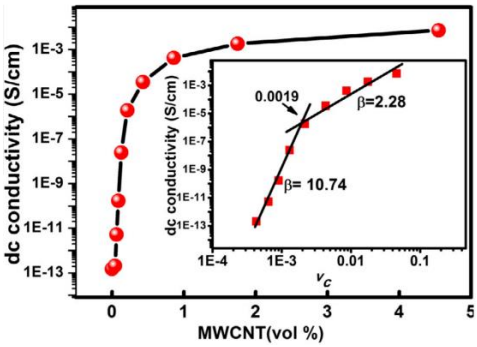

Figure 1-5. The electrical conductivity versus multiwall carbon nanotubes (MWCNT) (vol.%) loadings in polypropylene copolymer/MWCTs composites. Inset shows the log plot of conductivity as a function of v_c.[36]

The addition of CNTs or graphene into insolating polymers lead to the onset and almost continuous tunability of the electrical conduction due to the formation of 3D network among polymer matrix. The electrical conduction mechanism is carrier transport via intra-molecular hopping/tunnelling between the dispersed filler particles. The minimum filler loading when the continuous conducting network starts to form is referred as the percolation threshold.[26] The correlation of electrical conductivity and the volume fraction of filler follows a power law function:

$$\sigma=\sigma_0(v-v_c)^t \tag{1-1}$$

where σ is the electrical conductivity of the composite, σ_0 is the characteristic conductivity, v is the volume fraction of filler, v_c is the volume fraction at the percolation threshold, and t is the critical exponent. The percolation threshold in CNT/polymer nanocomposites can be affected by many parameters such as filler functionalization, aspect ratio, dispersion, alignment, etc. Due to self-aggregation of the 1D shaped CNTs and the π-π stacking between graphene flakes, the percolation threshold is always higher than the theoretical filler loading value. For the same filler loading, CNTs often show higher electrical conductivity than graphene.[25] As shown in Figure 1-5, the electrical conductivity could be improved by several orders of magnitude after the filler incorporation.

The thermal conductivity and thermal stability (glass transition temperature T_g) can also be improved after incorporating low-dimensional carbon fillers into polymers and found to increase with filler loading fraction.[25] However, due to the presence of numerous grain boundaries and interfaces among the filler/matrix composite, phonon scattering is enhanced, so the increase in thermal conductivity is not as significant as the

increase in electrical conductivity when the filler loading is increased. Usually only a few times thermal conductivity improvement is obtained at relatively high CNTs or graphene loading.[37], [38]

The improvement of mechanical strength after CNTs or graphene incorporation is another important application of nanocomposite. A CNTs/epoxy composite showed an increase of 4.2 to 35% in tensile strength compared to bare epoxy.[25] For aligned CNTs array/epoxy composite, a Young's modulus of 15.0 GPa and a tensile strength of 104 MPa were reported along the CNTs alignment direction, which are several times higher than the bare epoxy.[39] As expected, the tensile strength is found to increase with the loading of graphene filler, shown in Figure 1-6.

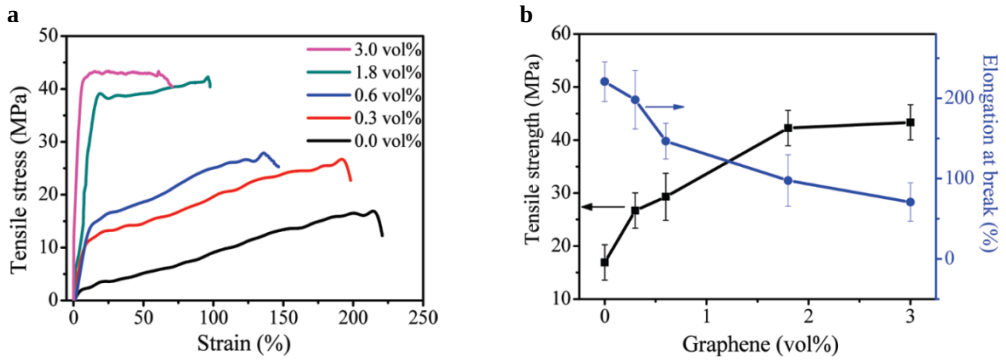

Figure 1-6. a, A typical stress-strain plots of the composites with various graphene loadings. **b**, Tensile strength and elongation beak of graphene/PVA composites with various graphene loadings.[40]

1.3 Introduction in photo-thermoelectric effect

The photo-thermoelectric (PTE) effect in photodetectors consists of two consecutive processes: 1) the low-energy incident photons induced intra-band or inter-band excitations in the carbon nanomaterials; 2) the hot-carriers gradient (temperature gradient) induced

thermoelectric conversion, as a result of the artificial asymmetries of Seebeck coefficient and thermal conduction along carrier transporting direction.

1.3.1 Light and matter interaction

While inter-band transition contributes to the main light absorption mechanism in the visible and near-infrared region in graphene, for long-wave infrared and THz waves, the intra-band transition, also termed as free carrier response, dominates this process due to the relatively low photon energies.[41]

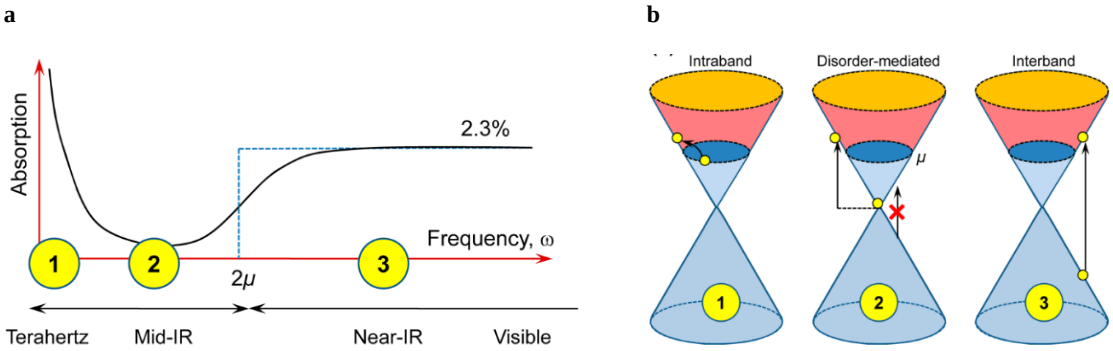

Figure 1-7. a, A typical light absorption spectrum in doped graphene. **b**, Illustration of optical transition processes for different light wavelengths, and μ is the chemical potential.[42]

Figure 1-7 illustrates the light absorption spectrum in doped graphene from visible to terahertz range and the various optical transitions. At visible and near-infrared regimes, the experimentally measured light absorption in graphene is frequency-independent and close to $\pi\alpha \approx 2.3\%$, where $\alpha = \frac{e^2}{\hbar c}$ is the fine structure constant.[43] The light absorption in the long-wave infrared and terahertz range where the frequency $\omega < 2E_F$ can be described by the Drude model. The optical conductivity and DC conductivity are[42], [44]

$$\tilde{\sigma}_{\text{intra}} = \frac{iD}{\pi(\omega + i\Gamma)} \tag{1-2}$$

$$\sigma_{DC} = \frac{D}{\pi\Gamma} \tag{1-3}$$

where $D = \frac{e^2 E_F}{\hbar^2}$ is the Drude weight, ω is angular frequency of electromagnetic waves, and $\Gamma = \frac{1}{\tau}$ is the phenomenal scattering rate. (E_F is Fermi energy, $\hbar$ is reduced Plank constant, τ is electron scattering time). For mid-infrared waves, reduced absorption is expected due to the Pauli blocking, and disorders plays an important role in the optical transitions in doped graphene.[45]

The light-matter interaction in CNTs is similar to that in graphene but differs in several ways. One is that macroscale CNTs assemblies usually consist of metallic tubes with zero bandgap like graphene as well as semi-conductive tubes with small bandgaps. The second is that CNTs is one-dimensional which leads to resonant absorption in certain light frequencies when the phases of plasmon and light wave are matched. Two absorption mechanisms have been proposed by Kampfrath et al. to explain the far-infrared light interaction with CNTs, as illustrated in Figure 1-8.[46] In a broad infrared wavelength range of 2~667 μm, the Drude-Lorentz model was employed by Ugawa et al. to describe the dielectric constant[47] of a freestanding CNTs film as

$$\varepsilon(\omega) = \varepsilon_c - \frac{{\omega_p}^2}{\omega(i\gamma + \omega)} - \sum_j \frac{{\Omega_{pj}}^2}{(\omega^2 - {\omega_j}^2) + i\Gamma_j\omega} \tag{1-4}$$

Where ε_c stands for the frequency-independent dielectric constant, ω_p is the plasma frequency, γ is the relaxation rate of the charge carriers, and ω_j, Γ_j, Ω_{pj} are the center frequency, spectral width, and oscillator strength of the Lorentz oscillators.[47] The second term in this equation is Drude term which describes the free electron response and is utilized to characterize the optical properties of metals at relatively low frequencies. The third term is the Lorentz term that presents the contribution from Lorentzian oscillators due to inter-band transitions in dielectric materials and metals at relatively high frequencies.[48]

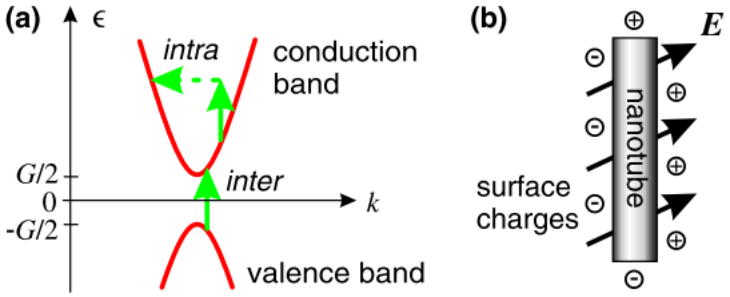

Figure 1-8. a, The optical transition mechanism in carbon nanotubes a band diagram - the inter-band transition across the band gap and the impurity-assisted intra-band transition. **b**, The plasmon resonance absorption mechanism in a carbon nanotube.[46]

In contrast to the isotropic absorption observed in single-layer graphene,[49] a high optical anisotropy exists in aligned CNTs thin-film and patterned graphene ribbons. The light absorption in CNTs is larger when the electric field of incident waves is parallel to the CNTs alignment and is smaller when the electric field is perpendicular to the CNTs alignment.[50], [51] Wang et al. extracted the plasma frequency $\frac{\omega_p}{2\pi}$ in aligned CNTs film to be 13.1 THz and 39.3 THz in $E_\perp$ and $E_{||}$ directions, respectively, falling between doped semiconductors and perfect metals. Due to the larger free electron density and conductivity

along the CNTs alignment direction, the higher plasma frequency in $E_{||}$ direction leads to enhanced plasmonic absorption and free carrier excitation.[50], [51]

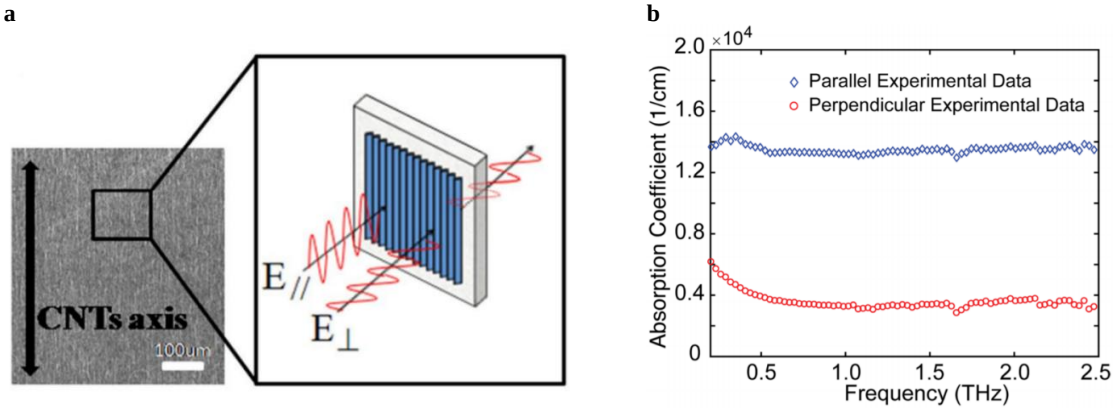

Figure 1-9. a, The absorption coefficient spectra for aligned CNT films at a few THz. **b**, A carbon nanotube polarization sensitive THz detector working at 1~3 THz.[50]

It is noteworthy that vertically aligned CNTs are regarded as "world's darkest substance" due to the extremely high light absorption properties throughout a broadband spectrum. Ultralow reflectance of 0.01~0.02 was observed in the 0.2~200 μm wavelength range, as shown in Figure 1-10.[52], [53] This black body behavior is considered to originate from the unique forest structure as an assembly of nanotubes which are sparsely distributed and vertically aligned.[53] Advanced optical and photonic devices including but not limited to photodetectors,[52] solar cells,[54] solar steam generation[55] are possible by using the outstanding light absorption properties.

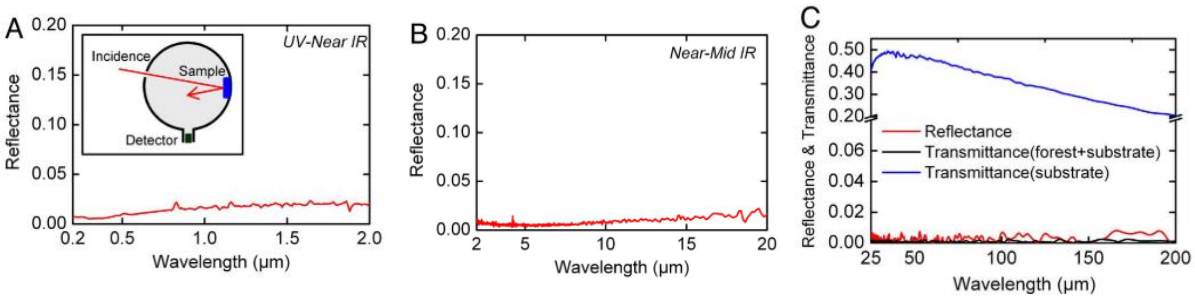

Figure 1-10. Reflectance and transmittance spectra of the vertically aligned SWNTs.[53]

1.3.2 Thermoelectric effect

The thermoelectric effect includes three separately identified effects: Seebeck effect, Peltier effect, and Thomson effect. Discovered by Thomas Johann Seebeck in 1821, Seebeck effect which is the reversed phenomenon of Peltier effect indicates a presence of temperature gradient can induce an electric field. The simplest application of Seebeck effect in our daily life is the thermocouple where two pieces of metal materials are connected for the temperature measurement. The temperature difference can be determined by the electric voltage measured at two ends of the circuit

$$V = \int_{T1}^{T2} \left[S_B(T) - S_A(T) \right] dT \tag{1-5}$$

S stands for Seebeck coefficient of the material which can be measured by

$$S(T) = -\frac{\Delta V}{\Delta T} \tag{1-6}$$

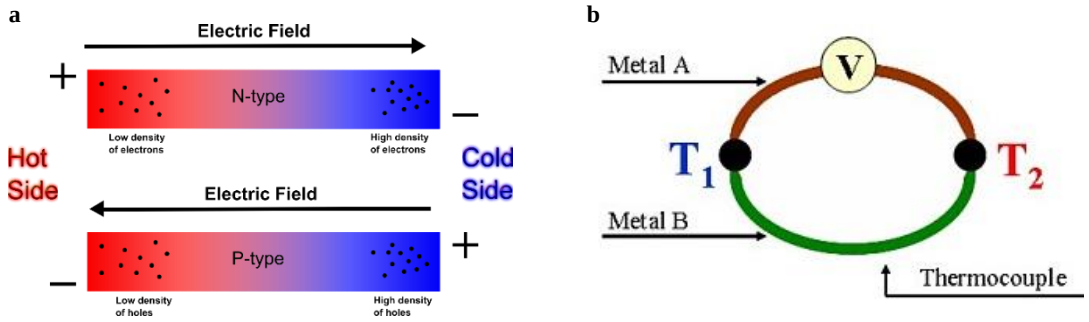

Figure 1-11. Schematic of thermoelectric effect and Seebeck effect. [56]

As illustrated in Figure 1-11a, the Seebeck effect originates from temperature gradient induced non-uniformity of carrier density: the carrier density is higher in cold-side compared to the hot-side due to less carrier thermal movement and scattering. This carrier density gradient creates an electric field pointing from cold-side to hot-side within P-type materials (which have positive *S*), and from hot-side to cold-side within N-type materials (which have negative *S*). The equilibrium state is achieved until the thermoelectric voltage has been built up to compensate the thermodynamics.

The Seebeck coefficient can be described by Mott relation in degenerate systems such as metals and heavily doped semiconductors[57], [58]

$$S = L\frac{T}{\sigma}\frac{d\sigma}{dE_F} \tag{1-7}$$

$$S = \frac{8L}{h^2}m^*T\left(\frac{\pi}{3n}\right)^{2/3} \tag{1-8}$$

where $L = \pi^2 k_B{}^2 / 3e^2$ is the Lorentz number, E_F is Fermi energy, k_B is Boltzmann constant, m^* is the effective mass of the carrier, and n is the carrier concentration. Mott relation reveals that Seebeck coefficient is correlated to the electrical conductivity and its variation

with Fermi energy. As the material electric conductivity ($\sigma = e\mu n$) are mostly influenced by Fermi electrons, the carrier mobility μ and carrier concentration n will change after the free carrier excitation which lead to the term $d\sigma / dE_F$.[57] The correlation $S \propto m^* n^{-2/3}$ indicated in equation (1-8) explains why n-type materials generally have larger S than p-type materials - due to the higher effective mass m^* for electrons, and why the semiconductors have larger S than metals - due to the lower carrier concentration n for semiconductors. For materials with strong electron-phonon coupling, the phonon drag effect also contributes to the Seebeck coefficient. In the presence of a temperature gradient, electrons can be dragged by the diffusing phonons and thus exhibit a higher effective mass thus a larger S.[59], [60] The electrical, thermal conductivities and Seebeck coefficients of some representative materials have been listed in Table 1-1.

Table 1-1. Electrical conductivity, thermal conductivity, and Seebeck coefficient of some representative materials.

Materials	Au	Al	Ni	Cr	Ti	Bi_2Te_3	Si
Electrical conductivity $\times 10^5\ \Omega^{-1}\ cm^{-1}$	4.4	3.7	1.4	0.78	0.23	0.01	0.0028
Thermal conductivity $W\ mK^{-1}$	315	237	90.5	90.3	21.9	1.6	145
Seebeck coefficient $\mu V\ K^{-1}$	1.9	-1.7	-19.5	22	9.1	200	450

In addition to the large Seebeck coefficient, a finite temperature gradient ∇T has to be applied to the device according to equation (1-5) for efficient thermoelectric conversion. The overall efficiency of a TE material is characterised by a dimensionless figure of merit ZT value defined as

$$ZT \approx \frac{S^2 \sigma T}{\kappa} \tag{1-9}$$

where S is Seebeck coefficient, σ is electrical conductivity, and κ is thermal conductivity, and the term $S^2\sigma$ is often referred as power factor. One always expects a large $S^2\sigma$ to maintain high carrier mobility, and a low κ to retain sufficient thermal gradient[61]. The best ZT value is found in heavily doped semiconductors because insulators have poor electrical conductivity and meals usually have low Seebeck coefficient.

As an inherent property, the electrical and thermal conductivity are strongly correlated in many materials especially in metals, through the Wiedemann–Franz law $L = \kappa_e / \sigma T$, where κ_e is electron thermal conductivity and $L = \pi^2 k_B{}^2 / 3e^2$ is known as the Lorenz number. Wiedemann–Franz law reveals that the thermal transport and the electrical currents are carried by the same fermionic quasiparticles in metals, and thus their ZT values are intrinsically restrained from being further improved. However, while electrons dominate the electrical and thermal transport in metals, phonons contribute to the thermoelectric effect additionally in semiconductors.[62] For semiconductors, a major contribution to the thermal conductivity comes from phonons with a minor portion coming from electrons. The advantage is that the ZT value can be improved by artificially suppressing the phonon induced thermal conductivity without causing too much reduction in the electrical conductivity. This can be achieved by creating interfaces in composites or alloys to enhance phonon scattering.[63]–[65]

1.3.3 Enhanced thermoelectric effect in nanostructures

Low-dimensional materials based nanostructures generally have better *ZT* values than the bulk counterparts due to higher Seebeck coefficient and lower thermal conductivity. One intrinsic benefit brought by low dimensionality is the increase in $d\sigma/dE_F$ which improves the Seebeck coefficient. For 3D, 2D, 1D, and 0D materials, the electrical conductivity σ is proportional to the carrier concentration *n* which further scales with the density of states (DOS) *g*(*E*) near the Fermi level, as shown in equation (1-10) to (1-13).[66]

$$\sigma_{3D} \propto n_{3D} \propto g_{3D}(E) \propto E_F^{\,1/2} \tag{1-10}$$

$$\sigma_{2D} \propto n_{2D} \propto g_{2D}(E) \propto E_F^{\,0} \tag{1-11}$$

$$\sigma_{1D} \propto n_{1D} \propto g_{1D}(E) \propto E_F^{\,-1/2} \tag{1-12}$$

$$\sigma_{0D} \propto n_{0D} \propto g_{0D}(E) \propto \delta E_F \tag{1-13}$$

Figure 1-12 clearly illustrates that with decreasing dimensions, the DOS changes more significantly as a function of E_F. This leads to the intrinsically enhanced Seebeck coefficient in low-dimensional material based nanostructures due to the higher $d\sigma/dE_F$.

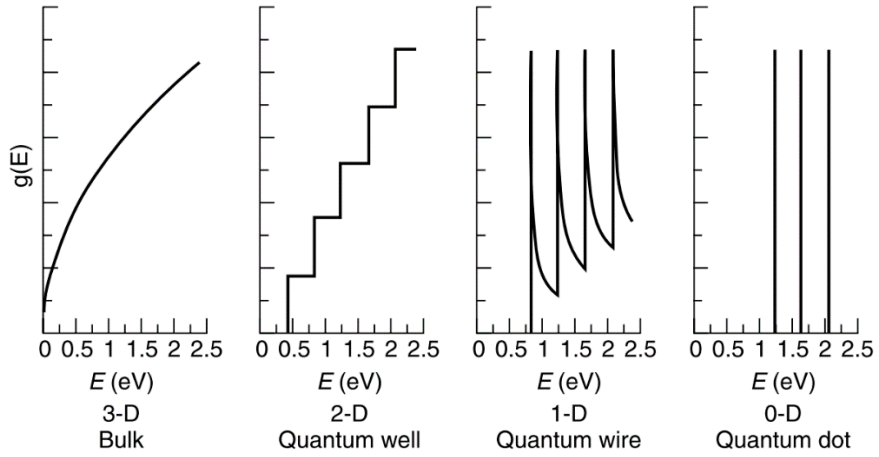

Figure 1-12. Energy dependence of electronic density of states in 3-, 2-, 1- and 0- dimensional materials.[66]

Several other strategies can also be employed to enhance the Seebeck coefficient of nanostructures including the energy filtering effect, the semimetal-semiconductor transition, and the carrier-pocket engineering.

The energy filtering effect can be understood as follows: the numerous interfaces within nanostructures act as small potential barriers that preferentially filter the low-energy carriers and pass higher-energy carriers through the interfaces.[67] This effect contributes to a larger asymmetry in the energy differential conductivity, i.e. the term $d\sigma / dE_F$ shown in equation (1-7). The reduction of electrical conductivity induced by energy barriers is more than compensated by the enhancement of Seebeck coefficient, which leads to an increase in the power fact $S^2\sigma$.[68]

The phenomenon of semimetal-semiconductor transitions happens when the physical size of a semimetal is significantly reduced to the nanoscale, e.g. in nanowires and nanoribbons. The semimetal energy bands split into discrete sub-bands due to the reduced

energy states in quantum confinement direction. As shown in Figure 1-13a, the highest occupied molecular orbital (HOMO) moves up and the lowest unoccupied molecular orbital (LUMO) moves down when the diameter of a Bismuth (Bi) nanowires decrease, leading to a gradually opened energy bandgap.[69] Similarly, Han et.al experimentally demonstrated that the graphene bandgap scales inversely with the ribbon width and obtained a quantitative fit $E_{gap} = \alpha / (W - W^*)$, where E_{gap} is the bandgap, W is the ribbon width, α=0.2 eV nm, and W^*=16 nm, as shown in Figure 1-13b. Through the semimetal-semiconductor transition, higher Seebeck coefficient and ZT value can be achieved.

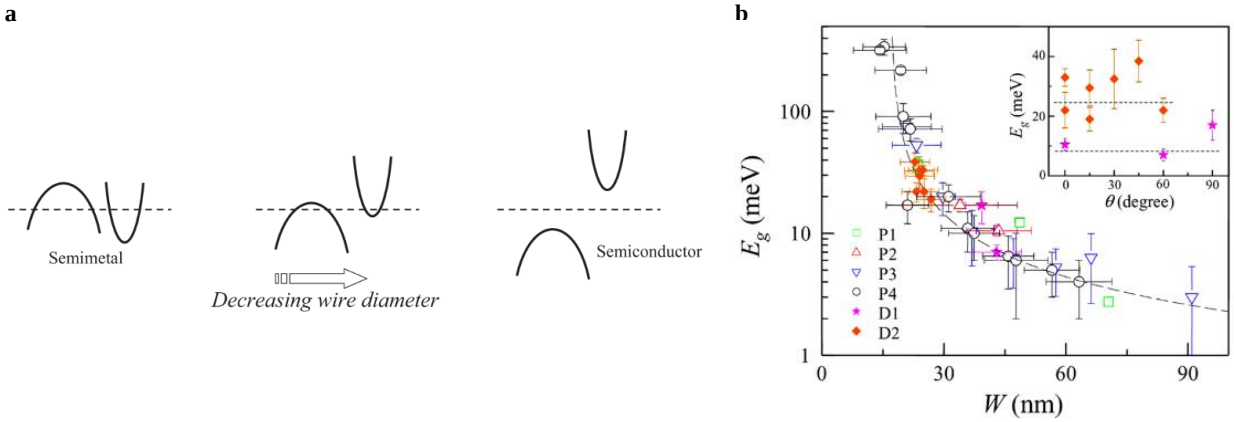

Figure 1-13. a, Schematic of Bismuth nanowire band structures with decreasing nanowire diameters.[68] **b**, The correlation between bandgap E_{gap} and ribbon width W in graphene.[70]

The rational of carrier-pocket engineering is to spatially confine two types of carriers with the same sign in the quantum well material and the barrier material separately, in order to achieve higher Seebeck coefficient. The concept was originally developed in GaAs/AlAs superlattice where the Γ-point electrons are restrained in GaAs quantum wells and X-point electrons are restrained in the AlAs barriers.[71]

Apart from improved Seebeck coefficient, a prominent effect that contributes to the high *ZT* value in nanostructures is the reduced thermal conductivity.[68] Intensive interfaces among nanoscale domains in nanostructured materials have scattered phonons more effectively than the electrons and lead to higher *ZT* values. This strategy has been widely applied in nanocomposite systems.[72]–[74]

1.4 Recent advances in infrared photodetectors

The electromagnetic spectrum consists of a broad wavelength range spanning from the radio wave, microwave, infrared, visible, ultraviolet, X-rays and gamma rays, as shown in Figure 1-14. Modern quantum theories state that the electromagnet waves exhibit both particle properties and wave properties at the same time. The quantized energy *E* of this particle, which is referred as photon, is correlated to the frequency of the wave by the equation $E = h\nu$ where *h* is the Planck constant. The developments of photodetection technologies have been playing a critical part in the modern sciences and technologies for man kinds, such as the radio wave probing for radio communication and radars, the microwave detection for 3G/4G Wi-Fi and mobile communication, the visible light detection for high-definition cameras in our daily life, the X-rays detection for biomedical imaging, disease diagnosis and physical therapy.

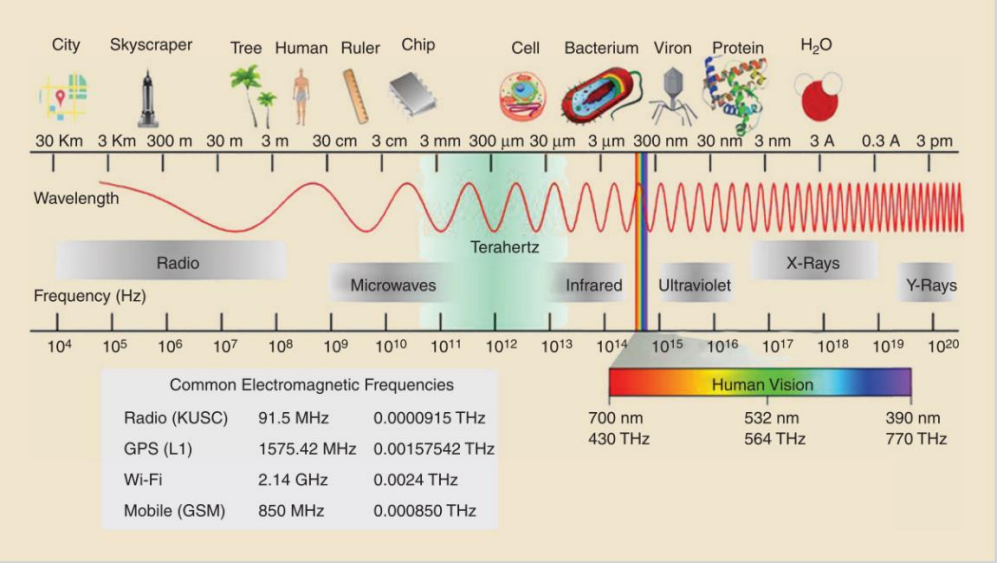

Figure 1-14. The electromagnetic spectrum. (Image courtesy of Caltech—funding by NSF.)

However, the photodetection technologies in mid-infrared and far-infrared (terahertz) range fall behind other wavelengths due to the lack of efficient detection mechanisms at room temperature. The photon energy is too low to fit the bandgap of most semiconductors and the electromagnetic wave frequency is too high for the response of electronic devices. For a long time, the fabrication complexity and high operating cost have limited MWIR and LWIR detectors only to military applications such as night vision and heat-seeking missiles, as well as scientific research purposes such as astronomy and Fourier transform infrared spectrometers. However, with the development of miniaturized, low-cost, and sensitive photodetectors working at room temperature, there are growing opportunities for civilian applications such as distributive sensors in Internet-of-things, biomedical thermal imaging,[75], [76] autonomous driving assistants,[77] and non-destructive industrial inspection.[78], [79]

1.4.1 Review of MWIR and LWIR photodetectors

In contrast to the mature photoconductive and photovoltaic detection technologies for visible-light photodetectors, there is a variety of photodetection mechanisms for MWIR and LWIR photodetectors. They can be classified into two categories: photonic detectors and thermal detectors. Photonic detectors include mercury cadmium telluride (MCT) detectors, GaAs/AlGaAs quantum well detectors, type-II InAs/GaSb superlattice, etc. Thermal detectors mainly include superconductor detectors, bolometers, Golay cells, pyroelectric detectors, and thermoelectric detectors, etc. Photonic detectors usually have very fast response and quite high sensitivity, but they must be cooled to the condition $kT \ll h\upsilon$ to reduce thermal noise while thermal detectors are generally lower cost and have relatively lower but broadband photoresponse.

The radiation in the MWIR and LWIR regimes correspond to photon energy less than 0.7 eV.[80] For inter-band transition photonic detection, there are only a few material systems that can satisfy the small bandgap requirement, including the commercial mercury cadmium telluride (HgCdTe), the lead chalcogenide family (PbS, PbTe, PbSe) and the indium antimonide based family (InGaAsSb). However, the tunability of the absorption and detection wavelength can only be achieved by changing the composition between each element. Also, these materials suffer from high fabrication complexity, low production yield and high cost. Lately, the advent of colloidal quantum dots (CQD) based photodetectors has mitigated these drawbacks with the size-tunable optical features and facile fabrication as solution-processable materials.[81], [82] Tang et.al demonstrated a dual-band infrared photodetector by tuning the physical sizes of two stacked CQD layers

and achieve both short-wave infrared (SWIR, 1.5~2.5 μm) detection and MWIR detection in a single device.[81]

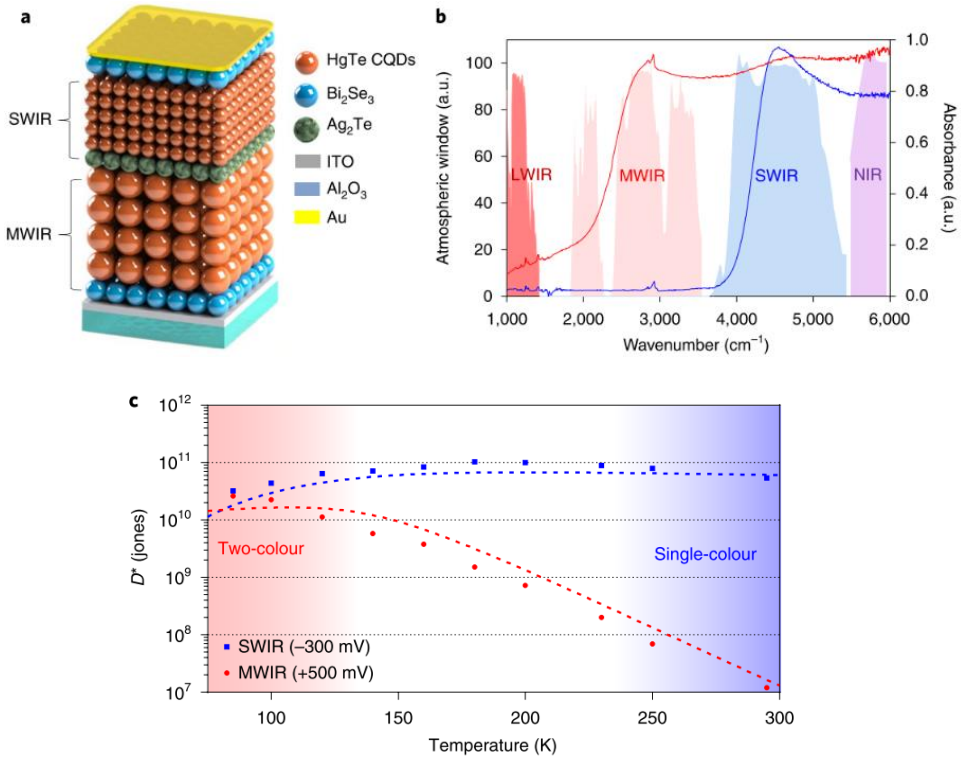

Figure 1-15. a, Illustration of the structure of a dual-band CQD imaging device. **b**, Optical absorption of SWIR and MWIR HgTe CQDs used to fabricate the dual-band device. The sizes of the SWIR and MWIR CQDs are 6 nm and 9 nm, respectively. **c**, Specific detectivity as a function of temperature under bias. Dashed lines are the calculated results.[82]

Another photonic detection methodology is the bandgap-limitless intra-band transition utilized for quantum-well infrared photodetectors (QWIP). A QWIP consists of periodically alternating GaAs/AlGaAs thin layers grown by molecular beam epitaxy (MBE) or metalorganic chemical vapor deposition (MOCVD). The thicknesses and doping concentrations of these semiconductor layers are precisely controlled in atomic level to engineer the conduction sub-bands energy splitting which is equivalent to a specific photon

energy. The detectivity of QWIP can reach 10^{10}~10^{11} cm $Hz^{1/2}$ W^{-1} under liquid nitrogen cooling (~77 K) and degrades with the temperature increase as shown in Figure 1-16a, b.[83] Palaferri et.al integrated a patch antenna array into the QWIP which effectively slowed down the decrease of the detectivity at elevated temperature (Figure 1-16c, d).[84] They attributed this improvement to both the enhancement of responsivity and the strong suppression of the dark current owing to the antenna effect.

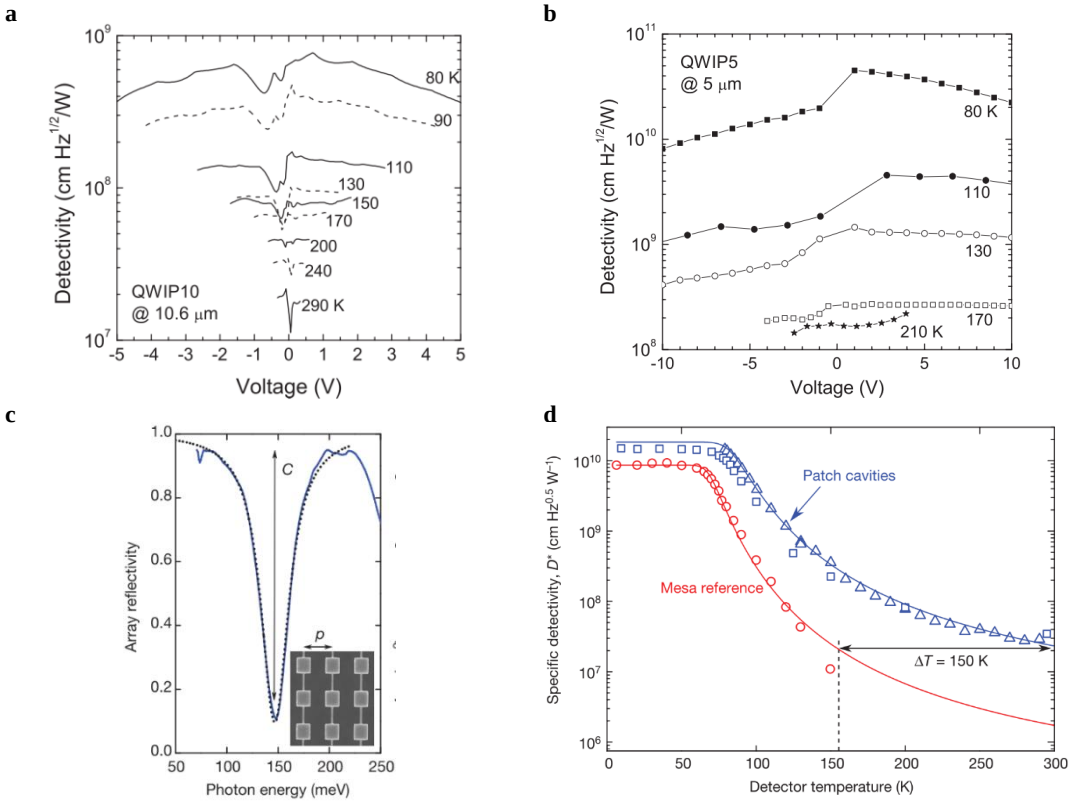

Figure 1-16. a, QWIP detectivity at 10.6 μm at various temperatures. **b**, QWIP detectivity at 5 μm at various temperatures. **d**, Specific detectivity D^* as a function of the temperature at a bias of 0.5 V for the mesa reference (red) and two array structures (blue). Reproduced from ref. [83], [84].

The most widely used thermal detectors are bolometers utilized in room-temperature thermal cameras. Usually each microbolometer in the focal plane array is made of

vanadium oxide or amorphous silicon heat resistor. Upon infrared illumination, the electrical resistance change due to phonon vibrations will be measured and processed into temperature values.[85] There is another type of bolometers called hot-electron bolometers which measures the resistance change of nanomaterials or superconducting materials under cooling conditions below 10 K. At cryogenic temperature, the electron-phonon coupling becomes much weaker and the electrical resistance could be strongly correlated to the electron temperature.[86] Hot-electron bolometers usually have extremely high sensitivity with the noise equivalent power (NEP) in the 10^{-15}~10^{-19} W $Hz^{-1/2}$ range.

More lately, the development of thermoelectric detectors has been largely advanced by the research on nanomaterials due to stronger light-matter interaction and enhanced thermoelectric conversion efficiency. The key concept of thermoelectric detectors is to create asymmetry of related physical properties in the device. Current photo-thermoelectric architectures mostly fall into two types - the light absorbing p-n junctions[87]–[89] and dissimilar electrodes based detectors.[90]–[94] The photoresponse of p-n junction thermoelectric detectors originates from the Seebeck coefficient difference of the p-type (positive *S*) and n-type (negative *S*) materials at presence of a temperature gradient in the vicinity of the junction induced by infrared illumination, as shown in Figure 1-17a, b.

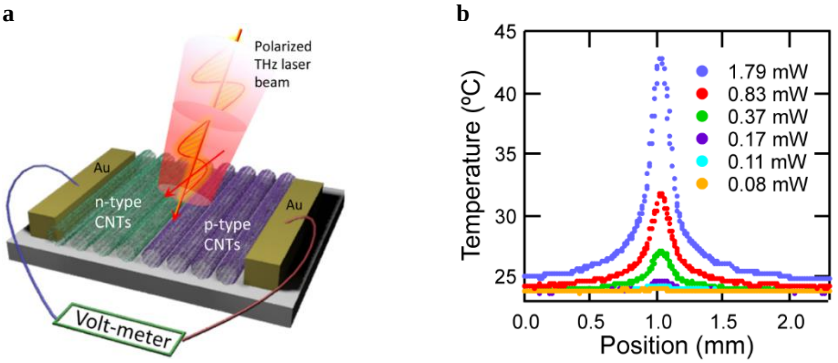

Figure 1-17. a, A schematic diagram of the detector consisting of the junction of a partially p-doped and partially n-doped CNT film. **b**, Temperature profile along the CNT film channel under laser illumination at different power densities.[51]

Dissimilar electrodes can also generate significant amount of photoresponse attributing to the differential thermoelectric effect at two kinds of electrode/channel interfaces. The dissimilar electrode combinations could be Sc/Pd,[95] Au/Cr,[91] and Al/Ti,[90] deposited on an infrared absorbing thin-film such as graphene and CNT. Diverse electrode combinations could yield different thermoelectric response as the result of different Seebeck coefficient offsets and the thermal gradient across the detector channel.[90], [96] In addition, the integration of plasmon resonant electrodes into this architecture have also been demonstrated (as shown in Figure 1-18b) to effectively improve the light absorption at certain wavelengths.[89], [91]

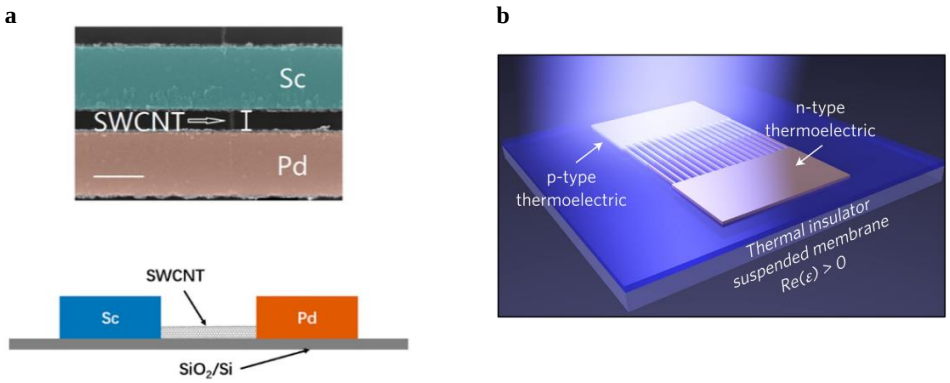

Figure 1-18. a, A schematic diagram of dissimilar electrodes based detector.[94] **b**, A plasmonic resonance enhanced thermoelectric photodetector.[89]

There is another thermoelectric structure which simply contains two identical electrodes and an infrared absorbing channel. But localized and focused illumination on one of the electrode/channel interfaces is required for photodetection functionality and this type of detectors is also bulky.[97]–[100]

1.4.2 Noises in photodetectors

Noises are very important consideration in photodetectors and the noise levels are different in different kinds of optoelectronic devices. The evaluation of noises is critical in determining the photodetector performance. The mainly considered noises in photodetectors include shot noise, Johnson-Nyquist noise, and flicker noise.

Shot noise, also known as quantum noise, is due to the fact that electrical currents are carried by discrete charges which transport and arrive randomly and discontinuously. The quantum nature of photons also gives rise to a statistical randomness of their arrivals onto the detector surface and contributes to the fluctuation of electron-hole pair generation.[101] The shot noise can be evaluated by

$$i_{sh} = \sqrt{2eI_{DC}\Delta f} \tag{1-14}$$

where e is the electron charge, I_{DC} is the average DC current, and Δf is the instrument bandwidth. Since the shot noise level increases with the current in circuit, high-voltage biased photodetectors often suffer from large shot noises.

Johnson-Nyquist noise (thermal noise) is the random voltage fluctuation existing in all electronic devices due to the thermodynamic motion of carriers. The Johnson-Nyquist noise level is expressed as

$$i_{JN} = \sqrt{\frac{4k_B T \Delta f}{R}} \tag{1-15}$$

where k_B is the Boltzmann constant, T is the temperature of the electronic device, and R is the resistance of the whole circuit.

Flicker noise is also referred as pink noise or $1/f$ noise as this kind of noise level is proportional to $1/f^a$ where $0 < a < 2$, and more significant in low frequency regime. Flicker noise is generally accepted to arise from the fluctuation of carrier number (in semiconductors) and mobility (in metals) due to the presence of defects and disorders as trapping and scattering sites.[102] The flicker noise in graphene and carbon nanotubes are found to scale with the current and temperature.[102], [103]

Considering that the photo-thermoelectric effect based photodetectors can operate under zero bias, i.e. self-power, the shot noise and flicker noise have been significantly reduced. The measured actual noise levels are found to approach the Johnson-Nyquist noise level limit.[89]–[91], [97] Therefore, reduced noise is another great merit for self-

powered infrared detectors besides being battery-free itself, and also the important reason for them to be capable of working under room temperature.

Chapter 2 Synthesis and characterization of low-dimensional carbon assemblies

There are a variety of synthesis methods of carbon nanotubes and graphene based materials, leading to various physical sizes, morphologies, number of graphite layers, composite materials, etc.

For carbon nanotubes synthesis, arc-discharge, laser ablation, and chemical vapor deposition are the three main methods. Arc-discharge and laser ablation can produce high crystalline CNTs with narrow tube diameter distributions, but the excessive by-products and high temperature (thousands of degrees Celsius) during the processes have hindered them from large-scale application.[104] Among the three, chemical vapor deposition (CVD) is the most widely adopted synthesis method due to the low set-up cost, high production yield, ease of scale-up, and control of CNTs architecture.[105] CVD allows the CNTs to grow in different forms such as powder, horizontally aligned thin-film,[106] vertically aligned forest,[107] etc., and on various substrate materials or predefined sites on a patterned substrate. The CVD growth of CNTs follows the vapor-liquid-solid growth pattern and generally comprises of plasma-enhanced CVD (PECVD) and thermal CVD.

2.1 Vertically aligned carbon nanotubes forest

Vertically aligned carbon nanotubes forest (CNTF) could be grown by thermal CVD or low-pressure CVD (LPCVD) machine. The process involves passing hydrocarbon

contained precursors to the catalyst layers sitting in a high temperature reactor (600℃ ~1100℃). The precursors consist of one hydrocarbon gas such as methane (CH_4), ethylene (C_2H_4) or acetylene (C_2H_2), and one reducing gas such as hydrogen (H_2) or ammonia (NH_3). Commonly used catalyst materials are nanometer thick transition metals such as iron (Fe), nickel (Ni), and cobalt (Co). Tip-growth model and base-growth model are the two growth mechanisms, as shown in Figure 2-1, depending on the interaction strength between the catalyst layer and substrate.

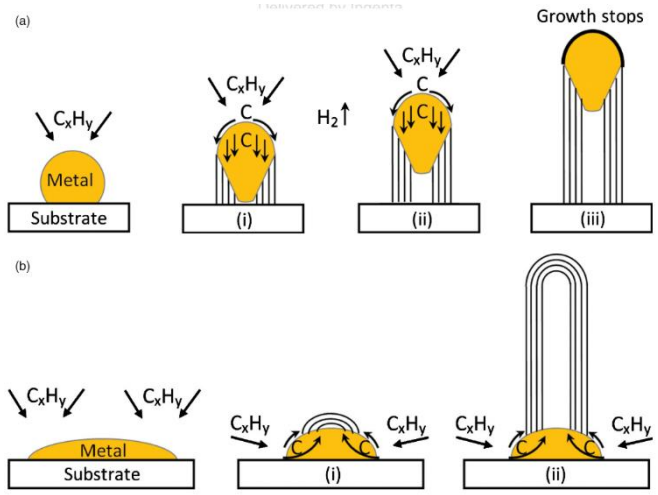

Figure 2-1. Two growth mechanisms of CNTs. **a**, the tip-growth model, **b**, the base-growth model.

The growth mechanism of CNTF follows the base-growth model which is composed of three steps:

1) The catalyst layer forms into nanoscale liquid-state droplets on the substrate through 'de-wetting' process at elevated temperature;
2) Hydrocarbon precursors get reduced and decompose into individual carbon atoms around the catalyst and then diffuse into the catalyst droplets;

3) When the catalyst droplets become supersaturated with carbons, the carbon atoms precipitate out of the particles and nucleate into carbon nanotubes. The nanotube diameter is the same as the catalyst droplets size.

The vertical alignment of individual CNT is achieved by the Van de Waals force between each closely standing nanotube as the density of the forest is quite high. The height of the CNTF span from tens of microns to millimeters scale depending on the catalytic activity. It is noteworthy that a small amount of water has been considered to enhance the catalytic activity and assist the growth of ultralong CNTF, creating a height of 2.5 millimeters.[108]

2.1.1 Catalyst layers preparation

In the following two sections, we present our synthesis method of CNTF.

The preparation of catalyst layers is critical as the thicknesses of each catalyst layer strongly influence the CNTF growth results. The top catalyst layer is a 0.8 nm Fe catalyst film deposited by magnetron sputtering (AJA Orion twin chamber). The thickness of Fe layer is of great importance since it determines the de-wetting droplet size and thereafter determines the CNTs diameter. In general, a thinner Fe catalyst layer produce SWNTs while thick Fe catalyst layer produce MWNTs. Underneath the Fe layer, there is 10 nm Al layer which acts as diffusion barrier preventing the Fe atoms from diffusing into the Si and provide proper wetting properties of the Fe droplets. Alternatively, Al_2O_3 could also be used instead of Al. A 20 nm Ti bottom electrode is sandwiched between the Al layer and

the doped Si substrate. Prior to this, the RCA cleaned Si substrate was previously back-side metallized with 5 nm Ti/20 nm Au using electron-beam evaporation.

2.1.2 Low pressure chemical vapor deposition of CNTF

The catalyst layers covered substrate is then put into a chemical vapor deposition reactor (Aixtron Black Magic 2 system). Prior to CNTF growth, the catalyst has to be annealed under 700 sccm (standard cubic centimeters per minute) H_2 in the reactor at 550℃ for 10 min to reduce the oxidized Fe_2O_3 back to Fe. More importantly, the nanoscale Fe thin-film starts to melt and becomes discontinuous islands and finally droplets during the annealing process. That iron could melt at such low temperature is because at nanoscale the melting point of metal is significantly reduced, as show in Figure 2-2.[109]

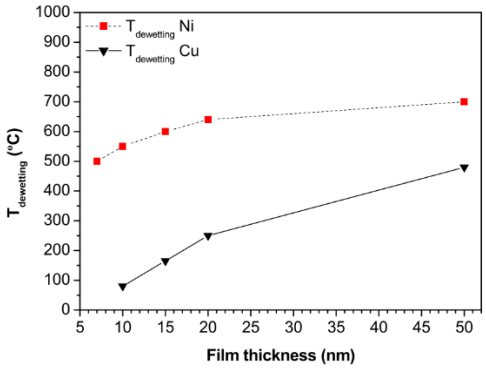

Figure 2-2. $T_{dewetting}$ as a function of different film thicknesses for Ni and Cu. Reproduced from ref.[109] The melting points of bulk Ni and Cu are 1455°C and 1085°C, respectively.

After annealing pre-treatment, the CNTF growth takes place at 660℃ and 15 mbar by introducing 10 sccm C_2H_2 flow as carbon stock while 700 sccm H_2 is kept serving as reducing gas. For a typical 30 min growth, the CNTF height is ~100 μm, and the average tube diameter is ~10 nm. After growth, the C_2H_2 and H_2 flows are shut off and 2000 sccm N_2 is introduced to protect the as-gown CNTF from oxidizing while the reactor chamber

cools down until 200°C. The scanning electron microscope (SEM) picture of as-grown CNTF is shown in Figure 2-3. Scanning electron microscopy (SEM) images of is taken in a JEOL JSM 7200F field emission SEM at 5 kV/10 kV voltage with 8~10 nA beam current.

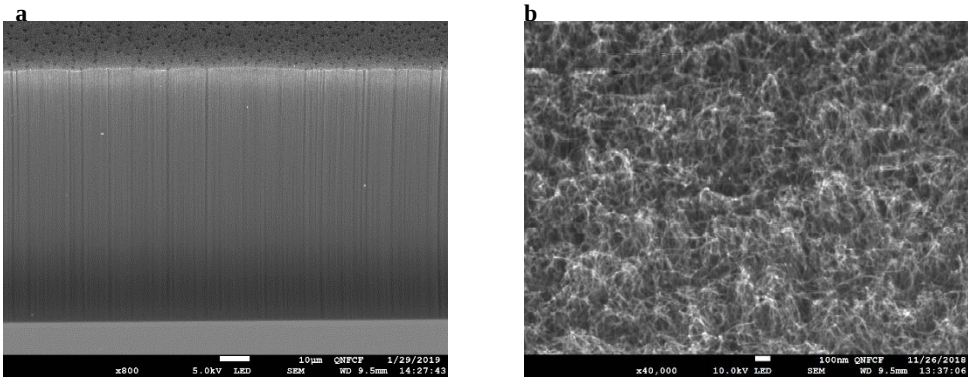

Figure 2-3. SEM pictures of as-grown CNTF on Si substrate. **a**, tilted view of CNTF, the scale bar is 10 μm. **b**, top view of CNTF, the scale bar is 100 nm.

2.2 Carbon nanotubes/poly vinyl alcohol nanocomposite

The fabrication of CNTs/polymer composites can be generally classified into two methods: mixing and in-situ polymerization, as shown in Figure 2-4. Depending on whether the polymer is soluble in solvents, the composite mixing can be either achieved by solution processing or melt mixing.

Solution processing is the most widely used composite fabrication technique. Firstly, CNTs are added into polymer dissolved solvent such as acetone or water. Next, CNTs and polymer chains are dispersed via a variety of methods including magnetic/mechanical stirring, ultrasonication, shear dispersion homogenization, etc. to make the CNTs uniformly distribute within the polymer matrix. Finally, the CNTs/polymer blend is

transferred onto a substrate by spin coating (uniform and thin films formed) or drop casting (thicker films formed) followed by natural or heated evaporation of the solvent material.

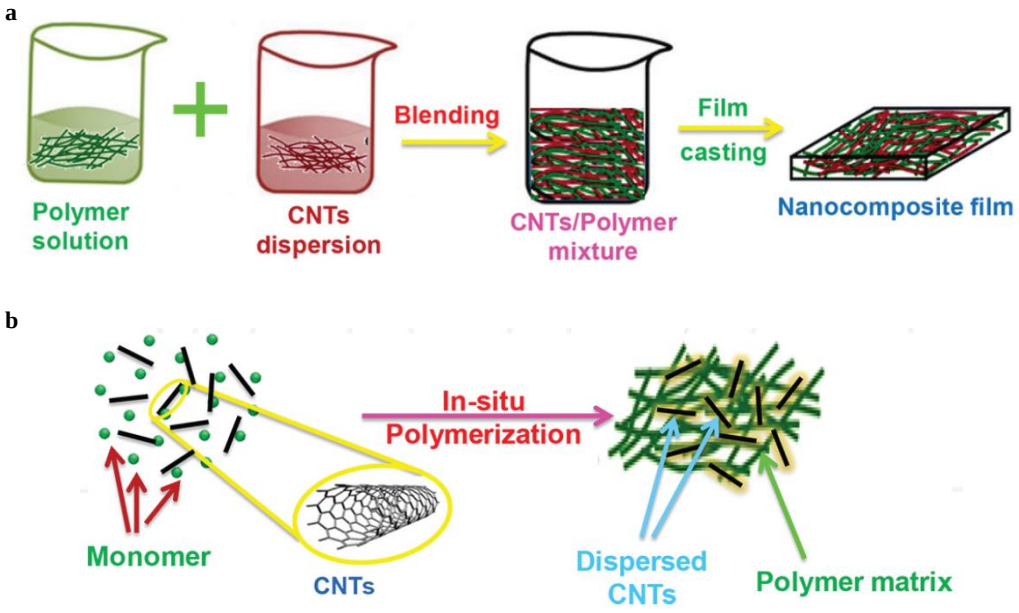

Figure 2-4. a, Solution processing schematic of CNTs/polymer composite. **b**, Monomers incorporation with CNTs and in-situ polymerizations.

2.2.1 Synthesis of CNTs/PVA composite

CNTs power and poly vinyl alcohol (PVA) composite is used as the photo-thermoelectric material in the 1st generation planar-structured photodetector.

To avoid CNT aggregation and bundling within the polymer matrix,[110] MWCNT with diameter < 8 nm, length 10~30 μm, and purity > 95% from Cheap Tubes Inc. is used in our work. The poly vinyl alcohol (Mw 100 000, 87% hydrolyzed) was purchased from Fischer Scientific. At first, 1g PVA powder was dissolved into 10 ml DI water by 2 hours at elevated temperature of 90°C and magnetic stirring. MWCNT was then added into PVA solution followed by 60 min ultrasonic bath and several hours magnetic stirring at room

temperature for efficient dispersion. Finally, the PVA/CNT homogeneous slurry was poured onto pre-cleaned glass or acrylic substrate for 48 hours slow drying. Due to the hydrophilic nature of PVA, dried composite film with typical thickness of 50~150 μm can be easily peeled off from the hydrophobic acrylic substrate, as shown in Figure 2-5.

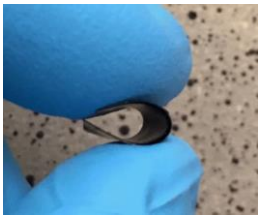

Figure 2-5. A flexible CNTs/PVA composite film peeled off from the substrate.

2.2.2 Characterization of CNTs/PVA composite

SEM pictures of PVA/CNT composites with different CNT contents are obtained in FEI Quanta Feg 250 ESEM at 10 kV voltage. Raman spectra and XRD patterns are investigated by Raman microscope Bruker Senterra with a 785 nm laser at 50 mW intensity, and Panalytical X'Pert PRO MRD HR X-Ray Diffraction System, repectively. Seebeck coefficients (measured by ULVAC-RIKO ZEM 3) for 40 wt.%, 50 wt.% and 60 wt.% CNT content composites are 27.3 μV K^{-1}, 22.5 μV K^{-1}, and 25.0 μV K^{-1}, respectively, consistent with device responsivity trend.

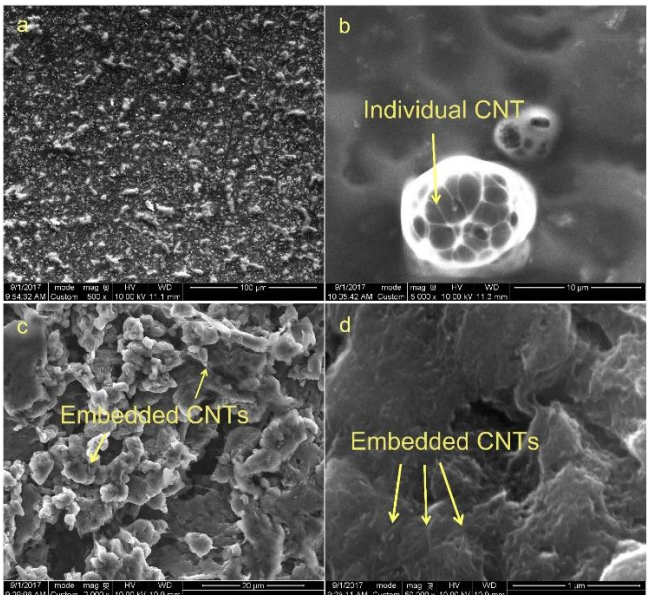

Figure 2-6. SEM pictures. **a**, 25 wt% CNTs/PVA composite. **b**, 15 wt% CNTs/PVA composite. **c**, **d**, 50 wt% CNTs/PVA composite.

The SEM pictures of CNTs/PVA composite with different CNT contents is shown in Figure 2-6. It can be found that the skeleton of CNTs is clearly revealed within the circular shape shown in Figure 2-6b created by high-energy electron beam as the PVA polymer has been burnt out. Figure 2-6c, d show that CNTs are dispersed and embedded within the polymer for the 50 wt.% CNTs content composite. Compared to the continuous-film morphology in low CNT content composite (Figure 2-6a, b), the 50 wt.% CNTs composite is porous due to the decreasing polymer content, causing the film to be more brittle.

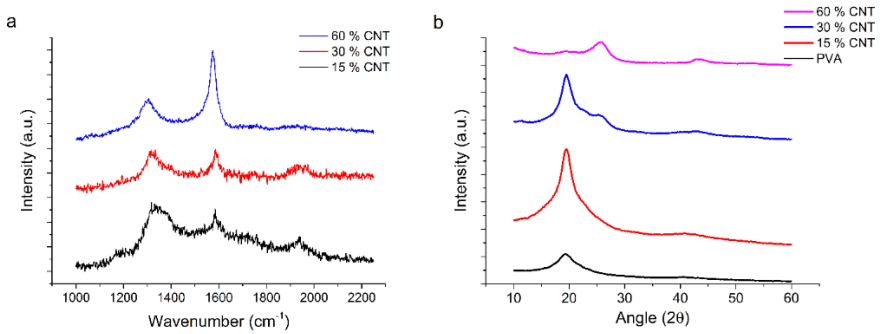

Figure 2-7. a, Raman spectra of composite films with different CNT contents. **b**, XRD patterns for PVA and composite films with different CNT contents.

Figure 2-7a is the Raman spectra of 15 wt.%, 30 wt.% and 60 wt.% CNTs composites. The spectra mainly containing the D band at ~1340 cm^{-1} and G band at ~1580 cm^{-1} originating from the MWNTs. The presence of D band indicates the disorders and defects in CNTs, and the G band is an intrinsic vibration feature of sp^2 hybridized carbon materials.[111] The broadening and red shift (towards low-frequency) of G band peak have been observed from 1584.5 cm^{-1} in the 15 wt.% CNTs composite to 1574.5 cm^{-1} in the 60 wt.% CNTs composite. We explain these phenomena are correlated to a relatively high Seebeck coefficient in well-dispersed composite with low CNTs content (e.g. 25 wt.%), and supressed Seebeck coefficient when CNT content continues to increase.[112]

Figure 2-7b shows the XRD patterns of pure PVA and CNTs/PVA composites. After adding 15 wt.% of CNT into pure PVA polymer, the characteristic peak of PVA at 2θ = 19.5° becomes stronger and sharper. The full widths at half-maximum (FWHM) of this peak shows significant sharpening with increasing CNTs content within composite: 4.2° for pure PVA, 3.3° for 15 wt.% CNTs composite, 2.8° for 30 wt.% CNTs composite and 2.7° for 60 wt.% CNTs composite. This indicates increasingly ordered arrangement of the

polymer molecular chains,[30], [113] i.e. enhanced PVA crystallinity at increasing CNTs content.

2.3 Graphene/PEDOT: PSS nanocomposite

PEDOT: PSS and graphene nanoplatelets composite has been fabricated as light absorbing and thermoelectric material in the 2nd generation planar-structured photodetector.

2.3.1 Synthesis of graphene/PEDOT: PSS composite

0.5 mL Dimethyl sulfoxide (purchased from Sigma-Aldrich, product ID: D4540) which acts as electrical conductivity enhancer is first added into 10 mL PEDOT: PSS water solution (1.3 wt.%, purchased from Sigma-Aldrich, product ID: 483095, and the ratio between PEDOT and PSS is 5:8). Next, graphene nanoplatelets (7 nm thickness, 2 μm diameter, purchased from Kennedy Labs) with different loadings within the composite (0 wt.%, 1 wt.%, 3 wt.%, 5 wt.%, 7.5 wt.%, 10 wt.%, 12.5 wt.%) are added into PEDOT: PSS solution. The mixed solution is dispersed by magnetic stirring at room temperature for 3 hours and placed in an ultrasonic bath (50 W) for 15 min in order to reduce the π-π stacking between graphene flakes. Dispersed solution is then transferred onto Kapton substrate (polyimide, ~100 μm thick) that has been pre-treated by 10% HCl solution for 1 hour to improve the hydrophilicity. A typically 3~4 μm thick and non-transparent graphene/PEDOT: PSS film can be obtained through drop-casting followed by 1 hour annealing at 150 ℃ on hot-plate.

For a transparent and highly flexible composite (film thickness 0.1~1 μm), the synthesis process is shown in Figure 2-8. Dispersed PEDOT: PSS/graphene solution is first

spin-coated onto HCl treated Kapton substrate at 500 ~ 2000 rpm speed followed by 10 min annealing at 150 ℃. Next, a relatively sticky PVA (100,000 molecular weight, 87% hydrolyzed, purchased from Fischer Scientific) water solution is drop casted onto the dry PEDOT: PSS/graphene composite surface. The hybrid material is left drying in ambient condition for over 48 hours. Finally, the PEDOT: PSS/graphene will stick with the PVA sheet and easily peel off the Kapton substrate attributed to the similar hydrophilic properties of PVA and PEDOT: PSS.

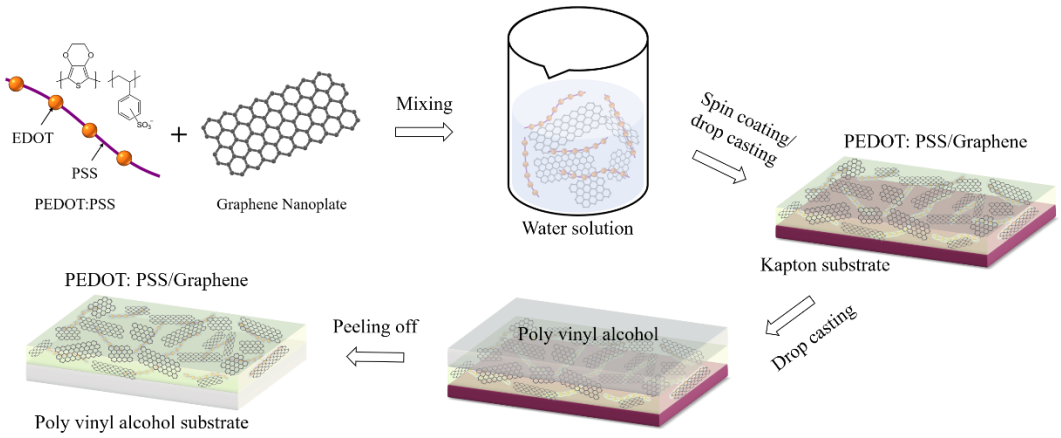

Figure 2-8. Fabrication process of PEDOT: PSS/graphene composite on a flexible substrate.

2.3.2 Characterization of graphene/PEDOT: PSS composite

Scanning electron microscopy (SEM) images was taken in a JEOL JSM 7200F field emission SEM at 10 kV voltage and 9 nA beam current. The Fourier Transform Infrared Spectroscopy (FTIR) spectra were measured in Bruker Tensor 27 FTIR system. The Raman spectra were obtained in Bruker Senterra-2 Raman spectrometer. The UV-Vis spectra of PEDOT: PSS/graphene composite were obtained in a PerkinElmer Lambda 35 &1050 UV-Vis spectrometer.

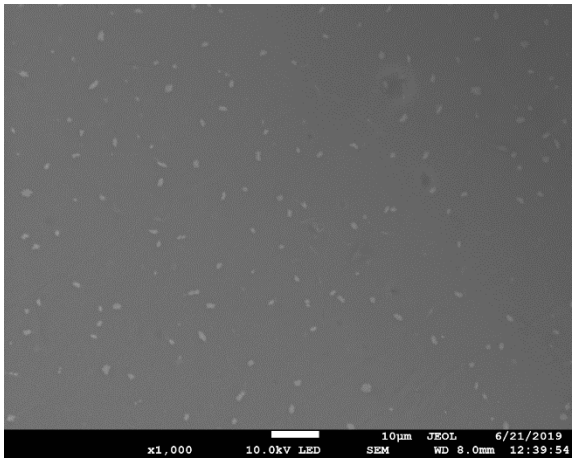

Figure 2-9. SEM image of PEDOT: PSS/3 wt.% graphene composite.

The as-dispersed PEDOT: PSS/graphene composite with graphene loading of 3 wt.% is shown in Figure 2-9. It can be seen that the micron-scale graphene nanoplatelets are well-dispersed within the polymer matrix.

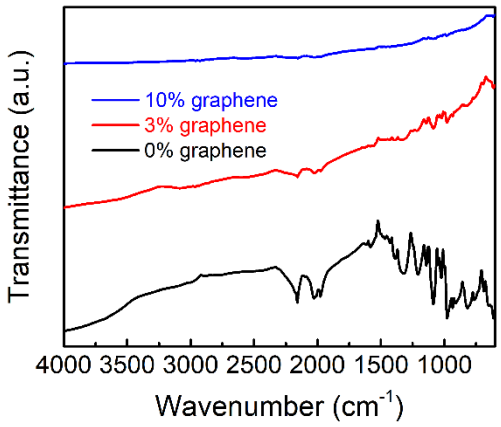

Figure 2-10. FTIR spectra of PEDOT: PSS/graphene composites.

FTIR spectra of 0 wt.%, 3 wt.%, and 10 wt.% graphene loading composites are shown in Figure 2-10. The vibrational bands at ~1325 cm^{-1} is attributed to the C−C stretching vibration of the thiophene ring.[114] The bands at ~1204 cm^{-1}, ~1141 cm^{-1}, and ~1086 cm^{-1} are brought by the C−O−C bond stretching in the ethylene alkylene dioxy group.[115]

The bands at ~976 cm^{-1} and ~819 cm^{-1} indicate the presence of C−S bond in the thiophene ring from PEDOT: PSS.[115] The characteristic peaks of PEDOT: PSS become weaker and weaker after the formation of PEDOT: PSS/graphene composite in 3 wt.% and 10 wt.% graphene composite due to the broadband light absorption in graphene.[116] No resonant absorption peaks originating from the micron-size graphene platelets have been observed, probably because the graphene nanoplatelets are distributed within the polymer matrix at various orientations and angles with regard to the incident light.

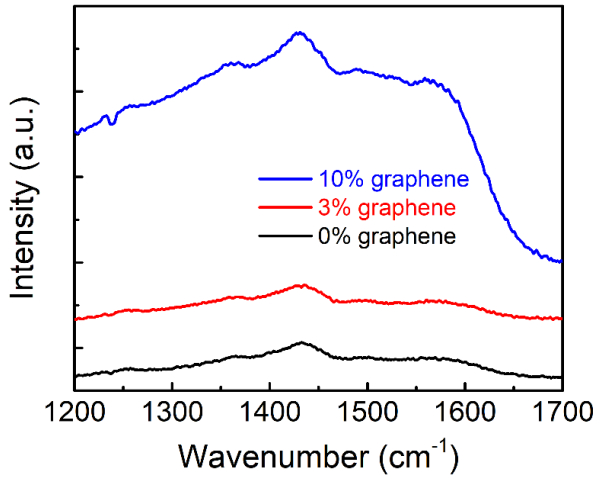

Figure 2-11. Raman spectra of PEDOT: PSS/graphene composites.

The Raman spectra of 0 wt.%, 3 wt.%, and 10 wt.% graphene loading composites are shown in Figure 2-11. Five bands shows on the spectra which can be interpreted as the C–C inter-ring stretching band (1258.0 cm^{-1}), the C–C single bond band (1364.5 cm^{-1}), the C=C symmetric stretch band (1433.0 cm^{-1}), the C=C asymmetric stretch band (1500.0 cm^{-1}), and the C=C anti-symmetric stretch band (~1571.0 cm^{-1}).[114] The C=C symmetric stretch peak shifts slightly from 1433.0 cm^{-1} in 0 wt.% graphene composite to 1430.0 cm^{-}

[1] in 10 wt.% graphene composite. This red-shift indicates an enhanced π-π interaction between the graphene nanoplatelets and PEDOT chains.[115]

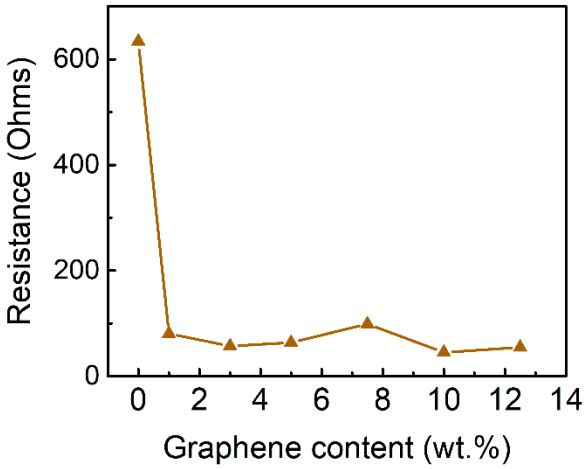

Figure 2-12. Electrical resistances of the composite at different graphene loadings. The electrodes are 200 nm Al and 25 nm ITO.

Figure 2-12 shows the electrical resistances of the composites at different graphene loadings. Pure PEDOT: PSS shows high resistance of 624 Ω. With 1 wt.% ~ 12.5 wt.% loadings of graphene nanoplatelets, the resistance becomes lower and varies around 67 Ω.

Chapter 3 Vertically aligned carbon nanotubes integrated anti-reflecting photo-thermoelectric architecture

3.1 Background and motivations

Beyond semiconductor bandgaps, mid-wave infrared (MWIR, 3-5 μm) and long-wave infrared (LWIR, 8-12 μm)[80] absorptions in most solid-state matters are fairly low compared to the visible range. This has been a main obstacle in the development of room-temperature mid-infrared optoelectronics which share broad applications in biomedical imaging,[76] industrial monitoring, and Internet of Things, etc. Although strong light-matter interaction in low-dimensional materials have largely improved detector performance,[117], [118] the portions of light getting absorbed by most 2D materials are rather low - up to 2.3% in single-layer graphene[42] and around 3% in black phosphorus.[118] The advent of plasmon resonant structures including grated electrodes[119] and patterned light-active materials[89], [120] have greatly increased light absorption at certain wavelengths. Resonant absorption around 10 μm are observed in graphene nanoribbons, achieving a photoresponsivity of 0.4 A W^{-1}.[121] However, expensive electron-beam lithography (EBL) fabrication keeps these subwavelength structures from large-area and low-cost application. With solution-processing advantage, quantum-dot based photodetectors also exhibit high photosensitivity from visible to mid-infrared range even at room-temperature.[81] Whereas the drawbacks include high toxicity

in these heavy-metal materials (HgTe/HgCdTe) as well as narrow responsive spectra restricted by the finite bandgap and resonant particle size. Besides, synthesized by scalable methods (vapor-liquid-solid growth or wet-etching), vertically aligned nanowire arrays such as Si,[122] SiO_2,[123] ZnO,[124] GaN[54], GaAs[125] and InAsSb[126] have been widely studied as anti-reflecting absorbers in the visible and infrared range. As a representative, carbon nanotube forest (CNTF), a self-aligned and densely-packed 3D architecture of carbon nanotubes (CNTs), is renowned for nearly perfect light absorption in an ultrabroad infrared range beyond far-infrared.[53], [127], [128]

However, one problem with long-wave infrared photodetectors using narrow- or zero-bandgap materials (such as CNTs and graphene) is the pronounced dark-current and low signal-to-noise ratio under DC biases. In this sense, recent intensive reports on photo-thermoelectric (PTE) effect have exemplified that photodetection utilizing photons induced thermoelectric effect at zero-bias can reduce the dark current effectively by avoiding $1/f$ noise and shot noise in circuits.[90]–[92], [129], [130]. PTE photodetection, on the other hand, also benefit from the enhanced thermoelectric effects in low-dimensional materials, attributed to the reduced thermal to electrical conductivity ratio κ/σ and strong electron density-of-states dependence on energy levels $dg(E)/dE$.[68] The demonstration of mid-infrared and far-infrared imaging with PTE photodetectors was firstly achieved by Suzuki et al. with a noise equivalent power of ~1 nW $Hz^{-1/2}$ at CNT/metal interface under ambient conditions.[90] Prior to that, Walia et al. discovered efficient photo-thermal conversion in vertical GaAs nanowires array under external light illumination and revealed a thermal gradient along the nanowires.[125]

To date, novel mid-wave and long-wave infrared photodetectors are still hampered by several challenges towards realistic applications. 1) High infrared reflection in low-dimensional materials due to high conductivities along zig-zag direction of 2D materials and the axis direction of 1D nanowires. 2) Field-effect photodetectors have ~μm scale channel lengths and limited detectivity so that focused high power-density lasers are needed as the actuating light source. 3) Most current PTE photodetectors are designed bulky for effective heat dissipation but require precise illumination on p-n junctions or the interfaces for photodetection.

In this work, we demonstrate a self-powered, large-area and broadband mid-infrared photodetector as well as energy harvester by exploiting the temperature gradient in a CNTF black-body absorber. Light reflection is suppressed by 99.4% in the self-assembled CNTF due to nanotube homogenous sparseness and vertical alignment.[53] To the best of our knowledge, this is the first macroscopic photodetector which employs the vertical photo-thermoelectric effect of an anti-reflecting nanowire array.[123], [125] This photojunction architecture enables the device to be responsive to an unfocused and broadband infrared light as low as 6.8 μW mm^{-2}, akin to the real-world illumination. We find an optimized PTE performance can be yielded in the top conductive layer (could be patterned) which has an appropriate thickness and low contact-resistance. A responsivity of 6 V W^{-1} and a detectivity of 2.2×10^{7} cm $Hz^{1/2}$ W^{-1} at 2.5~25 μm spectral range are observed in the non-lithographic CNTF photodetector with much room for optimization.

3.2 Photodetector architecture and light absorption

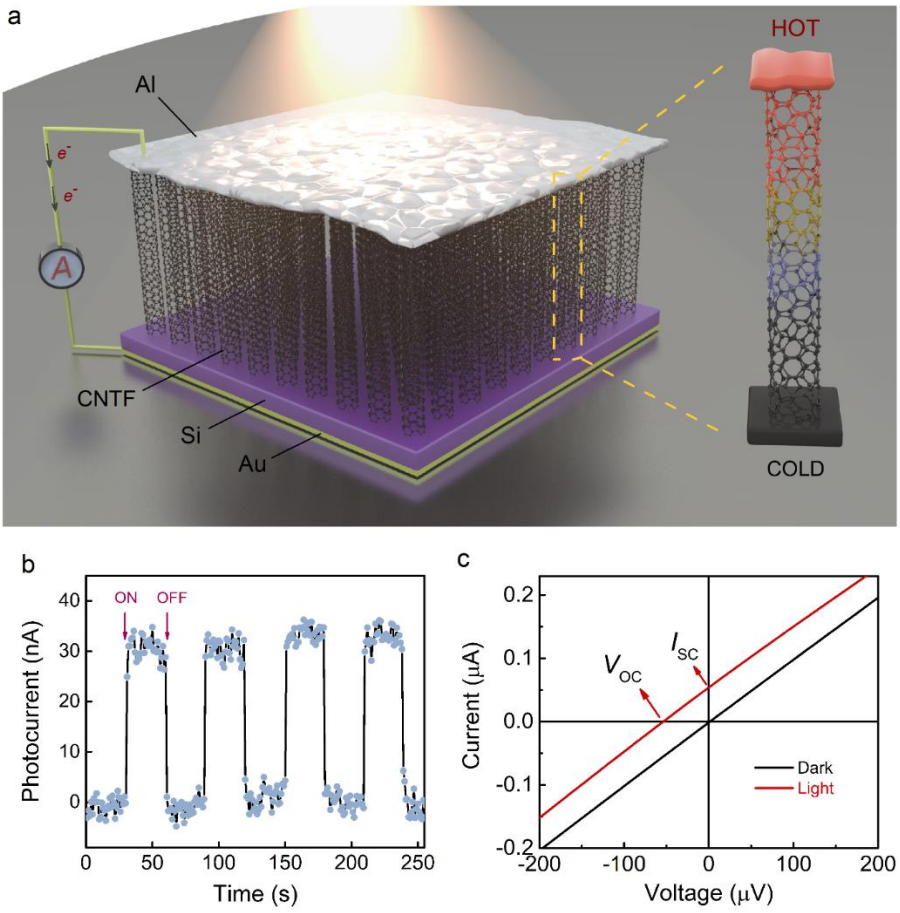

Figure 3-1. CNTF photo-thermoelectric photodetector. **a**, Schematic of the self-powered photodetector. A CNTF covered by top conductive layer (Al) is mounted on a doped-Si substrate with Au back-metallization. The zoom-in carbon nanotube on the right illustrates the temperature gradient of the photodetector induced by infrared illumination. Black arrows on the left indicate the electrons moving direction due to thermoelectric effect. **b**, Temporal response of the unfiltered photocurrent at zero-biased with the blackbody illumination on and off. The sampling rate is 1 s. **c**, Ohmic current-voltage characteristics under illumination and dark and conditions. Open-circuit voltage V_{OC} and short-circuit current I_{SC} are indicated. The top-electrode thickness and photosensitive area of the device in b, c) are 25 nm and 1 mm^2, respectively.

The photodetector schematic diagram is illustrated in Figure 3-1a. A densely packed CNTF grown by low pressure chemical vapor deposition (LPCVD) is sandwiched by the top and the bottom electrodes on a Si substrate. The top-electrode layer connecting individually self-standing CNTs is deposited by magnetron sputtering due to the conformal step-coverage on CNTs tips and better electrical contact compared to evaporation. Finally, the device is glued to the cathode on a chip carrier, and a thin gold-wire connected to anode pin is then glued onto CNTF top-electrode by silver conductive epoxy. A broadband, unfocused black-body radiation source (Newport Oriel 67030) was used to imitate real-world mid-infrared emission when measuring the detector photo response. The black-body temperature is set from 373 K to 973 K with an opening spot diameter of 0.5 cm, and photodetectors to be measured are placed 25 mm away. I−V characteristics and currents with and without black-body illumination were measured by a Keithley 6487 pico-ammeter. The photo-thermoelectric voltages at zero-bias were calculated from measured photocurrents by $V = IR$, where R represents resistance of the device.

The photodetection is based on photo-thermoelectric effect that accumulated p-type carriers from the cold bottom of CNTF diffuse towards the illuminated top surface, as evidenced by zero-bias photocurrent direction shown in Figure 3-1a-c. To be specific, incident light waves will be absorbed by CNTF/top-electrode interface and trapped at upper region of the photodetector because our CNTs height (~100 μm) exceeds typical CNTF perfect absorbers (~10 μm).[127], [128] The top of the photodetector therefore becomes hot via electron excitation while the substrate serve as heat sink, leading to a thermoelectric voltage as per equation (3-1) due to the temperature gradient.

$$V = \int_{bottom}^{top} S(z)\nabla T(z)dz = \int S_{Al}(z)\nabla T_{Al}(z)dz + \int S_{CNTs}(z)\nabla T_{CNTs}(z)dz \quad (3\text{-}1)$$

Figure 3-1b indicates that under broadband radiation emitted from a black-body source, the device photocurrent exhibits a sub-second temporal behavior in response to the light switching on and off, which is satisfying as a room-temperature PTE photodetector. Figure 3-1c presents the ohmic current-voltage characteristics for the photodetector at dark and light conditions where a net photocurrent is measured at zero external-bias. Under thermal radiation of 514.9 μW mm^{-2} for 973 K source temperature, an open-circuit voltage of 44 μV and a short-circuit current 58 nA are generated. This self-power merit thus enabled the device an extra function as energy harvester, which can find applications in industrial waste-heat recycling and wearable human-body radiation collection.

The scanning electron microscope (SEM) morphologies of pristine and metal-covered CNTFs are presented in Figure 3-2 and Figure 3-3a-d. Figure 3-3a shows the intersection of upper surface and side wall in the CNTF/Al junction, and Figure 3-3b-d show the top-viewed CNTFs morphologies with increased Al coverage. As the metal thickness increases, nanotube interspace becomes narrower and the diameter grows larger which is roughly equal to the metal deposited as shown in Figure 3-2.

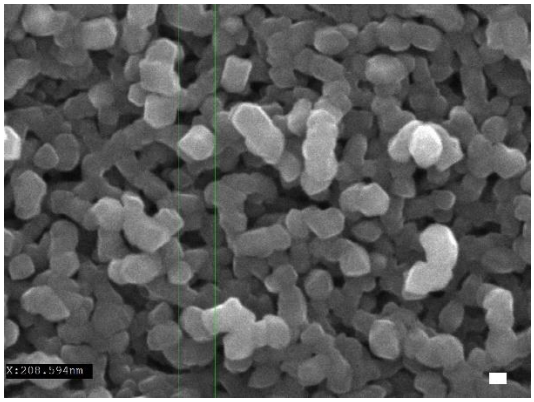

Figure 3-2. Top-viewed SEM image of a 200 nm Al covered CNTF. The diameter of each individual CNT expands to ~209 nm after Al sputtering. With the knowledge that pristine CNTs diameter is 8~10 nm, the actual metal coverage (~100 nm) on each CNT is in fact half of the sputtered thickness. Scale bar is 100 nm.

This sparse and vertical alignment of CNTs leads to a very efficient interaction with light waves (Figure 3-3e), which is confirmed via infrared reflectance measured by Fourier-transform infrared spectroscopy (FTIR). The FTIR spectrum is obtained by FTIR spectrometer (Nicolet iS50R FT-IR Thermo Scientific), and the 2.5~25 μm averaged reflectance is calculated by wavenumber. As shown in Figure 3-3f, throughout the 2.5~25 μm spectral range, relatively low reflectance of 0.6%, 11%, and 50% are observed in the pristine CNTF, 25 nm Al covered CNTF, and 100 nm Al covered CNTF, respectively. Compared to flat CNTs thin-films and bulk Al, the significant reflectance suppression in pristine/metal covered CNTFs is because: 1) The homogenous sparseness of CNTF has induced ideal refractive-index matching at the interface. 2) The slightly tilted CNTs alignment allows light waves bounce back and forth several times without escaping.[53] The lithography-free CNTF provides an efficient light-absorbing platform for broadband infrared photodetection.

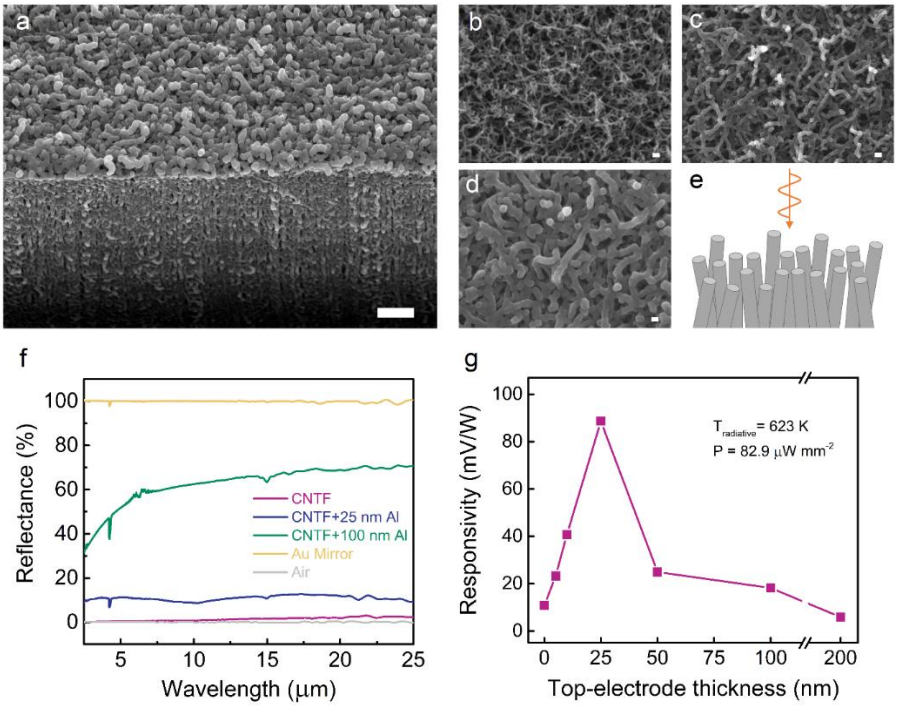

Figure 3-3. Morphology, infrared reflection and photoresponse of CNTFs covered by various metal thicknesses. **a**, Scanning electron microscope (SEM) image of a CNTF/Al junction (200 nm Al) taken at 35° tilted angle. The scale bar is 1 μm. **b-d**, SEM images of top-viewed 25 nm, 50 nm, and 100 nm Al covered CNTFs. The scale bar is 100 nm. **e**, Schematic of CNTFs under infrared irradiation. **f**, Infrared reflectance spectrum of air, pristine CNTF, 25 nm Al covered CNTF, 100 nm Al covered CNTF, and gold in 2.5~25 μm spectral range. The reflectance of air (0.03 %) and gold mirror (100.0%) are measured for reference. **g**, The photoresponsivity relation with increasing Al coverage on the CNTF. The device photosensitive areas are 1 mm^2.

3.3 PTE engineering of CNTF top conductive layer

The primary task of constructing a PTE detector is to effectively collect and convert the light-induced temperature gradient in vertically aligned CNTs. When a pristine CNTF top and bottom sides are directly connected by lead wire, measured photoresponsivity is fairly low (11 mV W^{-1}). Whereas after depositing an Al layer on CNTFs and increasing the thickness (5 nm, 10 nm, and 25 nm), the photoresponsivity has witnessed a rise of eight-

folds (89 mV W^{-1}) in the 25 nm Al covered CNTF as shown in Figure 3-3g. We explain this phenomenon in two aspects. First, since the electrical conductivity of CNTF in the vertical direction is much higher than that in horizontal direction,[131] only a small portion of photocurrent under silver paste can be collected and other CNTs are short-circuited. Thus, even though light absorption is maximized in pristine CNTF, a lateral top-electrode is critical for photocurrent collection. Second, the presence of Al on CNTF has constituted an interface which improves the localized Seebeck coefficient as a result of abrupt carrier concentration change between the hole-transporting CNTs and electron-transporting metal.[132] It has been considered that in vicinity of CNTs/metal contact, the Seebeck coefficient becomes significantly larger due to the chiral fermion interference resonance, taking place in conditions of Klein tunneling.[133] The continuous photoresponse improvement as Al increases from 5 nm to 25 nm follows the growing trend of Seebeck coefficient in bulk metals compared to thin-films.[134] An asymptotic expression of pure metal Seebeck coefficient at room temperature between the thin-film (S_{thin}) and bulk (S_{bulk}) morphologies can be given by the free-electron size effect theory show in equation (3-2)[135]

$$S_{thin} = S_{bulk}\left[1-\frac{3}{8}\left(\frac{l}{t}\right)(1-p)\frac{U}{1+U}\right] \tag{3-2}$$

Where t is metal thickness, l is electron mean free path, p is the fraction of carriers reflected at the film surface specularly, and $U=\left(\frac{\partial \ln l}{\partial \ln E}\right)_{E=\varepsilon}$ where ε is the Fermi level. By assuming $P=0$, $l=100$, and $U=2$ (i.e. $l \propto E^2$) according to Bloch quantum theory, a

notable reduction of S_{thin} compared to S_{bulk} is measured when the metal thickness is below 30 nm,[135] which is well consistent with our results. As the top-electrode becomes thicker, however, photoresponsivity exhibits a decay due to the stronger light reflection in metal which offsets other factors if the skin-depth of Al (7.5~24 nm at 2.5~25 μm spectral range) is considered.

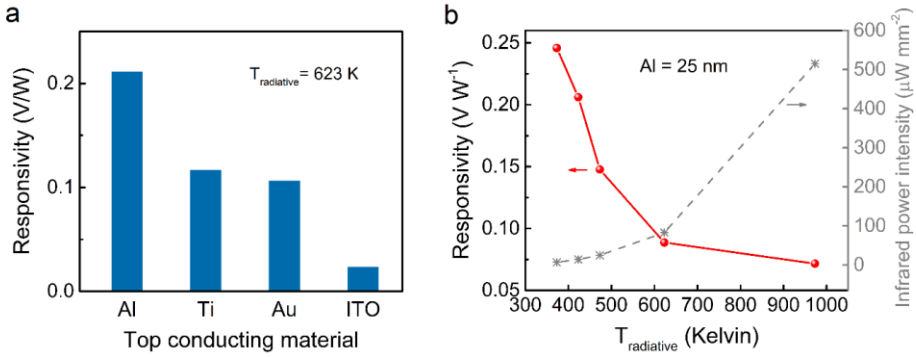

Figure 3-4. PTE response for different top-electrode materials and illumination conditions. **a**, Photoresponse of CNTF detectors covered by 4 kinds of conductive materials. The top-electrode thicknesses are 25 nm and photosensitive areas are 1 mm^2. The photoresponse of each junction is an averaged value by two devices. **b**, Photoresponse (in red dots) of a 25 nm Al covered CNTF detector under different radiative temperature, i.e. different incident power-density. The detector received illumination power intensities (the grey stars) are 514.9 μW mm^{-2} (973 K), 82.9 μW mm^{-2} (623 K), 24.6 μW mm^{-2} (473 K), 14.2 μW mm^{-2} (423 K), and 6.8 μW mm^{-2} (373 K), respectively.

With these knowledge in minds, we fabricate photodetectors with various top-electrode materials to investigate the PTE response properties.[90], [91], [96] Four kinds of CNTF/conductive material junctions with equal thickness of 25 nm are formed: CNTF/Al, CNTF/Ti, CNTF/Au, and CNTF/ITO. Figure 3-4a shows the photodetector response trend in these junctions where CNTF/Al junction owns the highest value followed by CNT/Ti, CNTF/Au, and CNTF/ITO. It has been recognized that thermal as well as electrical contact

quality of a junction have significant impacts on thermoelectric efficiency:[136]–[138] high thermal barrier resistance leads to reduced temperature gradient and high electrical contact resistance results in lower Seebeck coefficient in the vicinity of the interface.[137], [139] Here, we attribute these different PTE responses to a mutual effect of Seebeck coefficient offset and interface induced thermal gradient (physical parameters of the 4 junctions are reviewed in Table 3-1). Low PTE response in CNTF/Au junction and CNTF/ITO junction are considered correlated to the typically poor thermal and electrical contacts of Au and ITO.

Table 3-1. Physical properties of four CNTF/top-electrode junctions.

Junction Properties	Al	Ti	Au	ITO
Seebeck coefficient	-1.7 μV K^{-1}	9.1 μV K^{-1}	1.9 μV K^{-1}	-29 μV K^{-1}
Thermal barrier resistance with CNTs[140]	0.81	0.74	1.06	-
Electrical contact resistance with CNTs[141]–[143]	Low	Low	Medium	Generally high

Note: The Seebeck coefficient of CNTs are usually in the range of 20~50 μV K^{-1}.

Next, the photoresponse correlation with illumination power-density is obtained by adjusting the black-body source temperature from 973 K to 373 K (700℃ to 100 ℃). When source temperature decreases, the peak wavelength of radiative spectrum is shifted from 3.0 μm to 7.8 μm accordingly while the total power-density received by photodetectors is also decreased as shown in Figure 3-5.

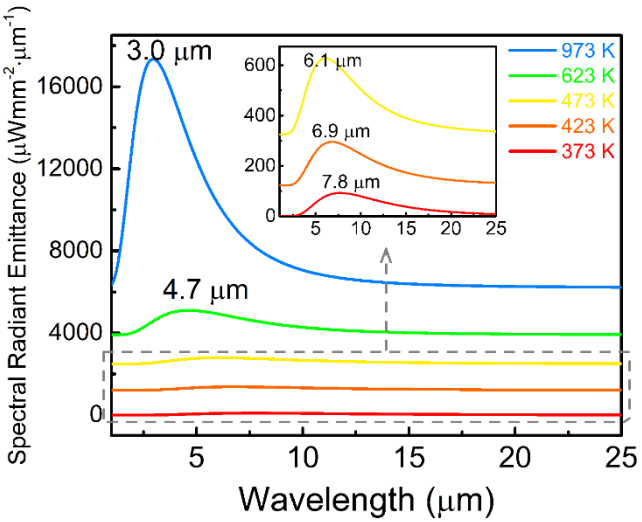

Figure 3-5. Calculated black-body spectral radiant emittances at temperature of 373 K, 423 K, 473 K, 623 K, and 973 K. The peak wavelength of the emittance spectrum increases from 3.0 μm to 7.8 μm as the black-body radiant temperature decreases from 973 K to 373 K.

As the detector received power-density changes from 514.9 μW mm^{-2} (973 K) to 6.8 μW mm^{-2} (373 K) shown in Figure 3-4b, we observe the photo detectivity increase from 0.07 V W^{-1} to 0.25 V W^{-1}. It reveals an improved photoresponse at lower illumination power-density in the 2.5~25 μm spectral range (~90% of the black-body radiation is situated in this band). The photoresponse nonlinearity mostly originates from temperature saturation at increased illumination power due to the less efficient cold-end (substrate) cooling. As shown in Table 3-2, we found as illumination power density increases, the substrate is heated up simultaneously with CNTF top surface, leading to a non-linear temperature gradient increase and non-linear photoresponsivity. This is because the CNTF are still too short for effective heat dissipation, and the silicon substrate is seated on a thermally insolating Teflon board which lacks effective cooling. Therefore, a more rational

choice of substrate material and additional bottom cooling layer are preferred to further improve device performance.

The calculated ΔT is estimated by $V = \int S \nabla T$ assuming S_{CNTF} = 30 μV K^{-1}. The difference between measured ΔT and calculated ΔT is probably caused by two reasons: 1) the relatively large measurement focal spot size of infrared thermometer compared to the device vertical dimension, 2) the emissivity difference between CNTs and silicon,[53] which leads to inevitable errors in non-contact measurement.

Table 3-2. Infrared thermometer measured and calculated device temperature under global illumination of IR source.

Temperature		Device top surface	Substrate sidewall	Measured ΔT	Calculated ΔT
Illumination Power	90 μW mm^{-2}	29.1 ℃	28.4 ℃	0.7 ℃	0.26 ℃
	350 μW mm^{-2}	32.0 ℃	31.1 ℃	0.9 ℃	0.42 ℃

Note: The device temperature without illumination is measured as 23.2 ℃ in ambient conditions.

A zero-bias photocurrent of 1.5 nA is measured under a quite low illumination of 6.8 μW mm^{-2}, which is probably the lowest power-density used for room-temperature PTE detectors. The weak-power sensitivity is considered benefited from the efficient light absorption and effective heat dissipation in the vertical metal/CNTF junction.[125] This feature could find practical significance in real-world photodetection where the infrared radiation to be detected/harvested is usually much weaker than a laser output. Moreover, this architecture might possibly pave the way to mid-infrared single-photon detection while a vertical InP nanowire array has recently been used to achieve room-temperature single-photon detection in visible range.[144]

3.4 Patterned top-electrode

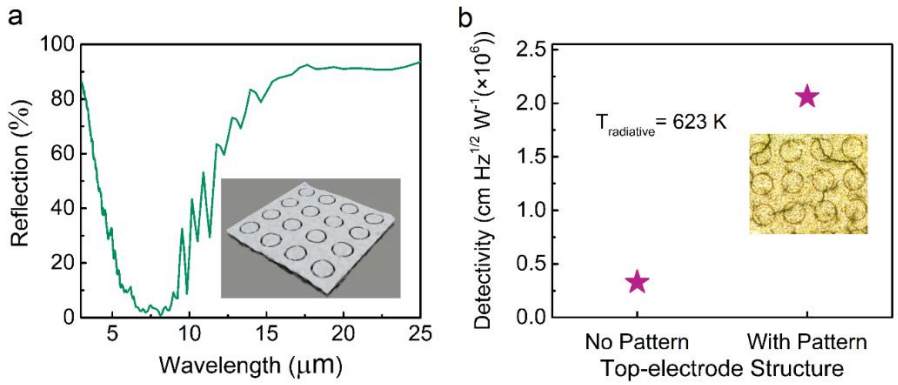

Figure 3-6. Patterned top-electrode. **a**, Simulated reflectance spectrum of a CNTF photodetector with periodic ring-shape patterns, showing a dip between 5 to 10 μm wavelength. The inset shows the schematic of the patterns whose period, outer diameter, and inner diameter are 50 μm, 38 μm, and 32 μm, respectively. **b**, Photoresponse comparison of two CNTF photodetectors with and without periodic patterns in the 200 nm Al top-electrode. Inset: optical image of the ring-shape patterned top-electrode.

As a pathway to improve light absorption in the presence of a top metallic layer, we design and fabricate microscale (Figure 3-6a inset) and nanoscale periodic patterns in the top-electrode (Al) to mitigate reflection. The optical simulation is carried out by finite element method in COMSOL Multiphysics. Periodic boundary conditions were established in *x* and *y* directions, and perfectly matched layer was placed in *z* direction above detector surface. The top (200 nm Al) and bottom (10 nm Al and 20 nm Ti) layers were treated as perfect electric conductor (PEC) layers, and the electrical conductivity of CNTF was modelled as (1, 1, 300) S/m along *x*-*y*-*z* axis.[131] The light wave in a frequency range of 10~100 THz (3 μm~30 μm) is normally incident onto the detector surface. Polarization-independent ring-shape patterns with 50 μm period, 38 μm outer diameter and 32 μm inner

diameter are chosen through impedance matching to minimize infrared reflection. Simulated reflection spectrum in Figure 3-6a shows that these patterns exhibit a reflection dip at around 4~12 μm spectral range where most of black-body radiation is situated. Here the light transmittance is treated as zero due to the presence of bottom metallic layers, and infrared absorption of the photodetector is $A(\omega)=1-R(\omega)-T(\omega)=1-R(\omega)$, where A, R, and T are the absorption, reflectance and transmittance, respectively. The 3 μm feature-size and 130 nm feature-size periodic patterns in Al top-electrodes were etched by inductively coupled plasma - reactive ions etching (Oxford Plasma lab). Etching masks were patterned by UV lithography (Suss MA6 Mask Aligner) with S1811 as positive-tone photoresist, and by electron beam lithography (RAITH150-TWO) with ZEP-520A as positive-tone e-beam resist, respectively. The measured photo detectivity demonstrates 6-fold increase after patterning the Al layer on CNTF (Figure 3-6b). These results demonstrate the possibility of photoresponse improvement by patterning the infrared-reflecting metallic layer on CNTF.

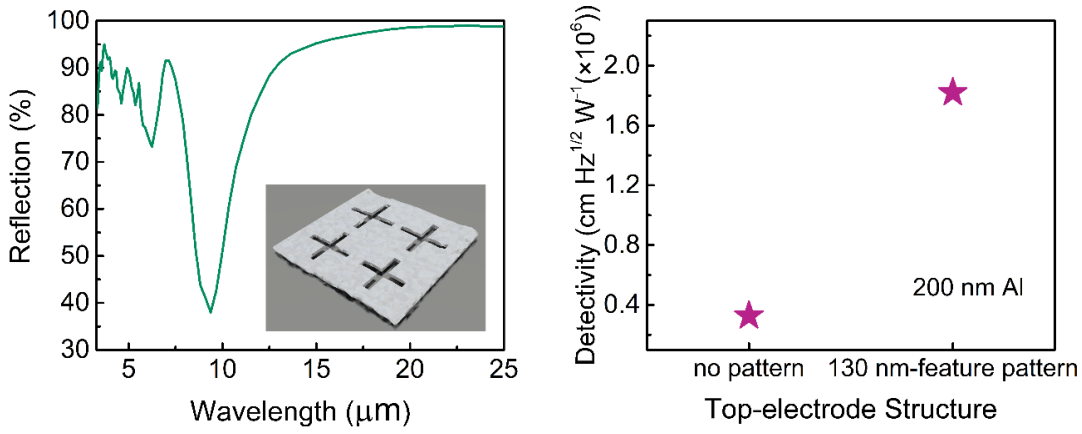

Figure 3-7. The device with EBL patterned top-electrode.

Figure 3-7 shows a CNTF photodetector with electron-beam lithography (EBL) patterned Al top-electrode. Simulated reflectance spectrum of a CNTF detector covered by 200 nm Al with periodic cross-shape pattern is shown in Figure 3-7a. The reflection dip is designed to be 9.3 μm, which is identical to infrared radiation from a human body, demonstrating the capability of a photodetector for body temperature monitoring and harvesting. The inset shows the schematic diagram of the patterns. Each period (3.7 μm) consists of 4 crosses with the same width of 130 nm, but different lengths: 1.67 μm (left top), 1.60 μm (right top), 1.53 μm (left bottom), and 1.46 μm (right bottom). The patterns are chosen to reduce the light reflection at the designed wavelength. Here, the SEM image of the pattern is not shown to avoid the damaging and doping effect by high-energy electrons at high-resolution mode.[121] Figure 3-7b shows the photoresponse comparison of a CNTF photodetector with and without the periodic patterns, showing ~5 times improvement.

3.5 Performance optimization and discussion

The best observed photo responsivity R_V and detectivity D^* are 6 V W^{-1} and 2.2×10^7 cm $Hz^{1/2}$ W^{-1}, respectively, in a zero-biased 25 nm Al covered CNTF device at 2.5~25 μm spectral range. Detectivity D^* which indicates capability of identifying the weakest illumination from noise is calculated by $D^*=R_v\sqrt{A}/\sqrt{4k_BTR}$ where A is photosensitive area, k_B is Boltzmann constant, T is temperature, and R is resistance. This performance rivals other PTE based photodetectors (the comparison is shown in Table 3-3) and the possibilities for further improvement are indicated in Figure 3-8.

Table 3-3. Comparison between this work and representative PTE photodetectors.

Photosensitive Materials	Photosensitive area	Light-source	Responsive wavelength	Responsivity	Detectivity	Ref.
Metal covered CNTF	0.05 mm^2	6.8 $\mu W\ mm^{-2}$	2.5~25 μm	6 $V\ W^{-1}$	2.2×10^7 $cm\ Hz^{1/2}\ W^{-}$	This work
Black phosphorus	7.2 μm^2	325 μW	0.26~0.38 THz	0.15 $V\ W^{-1}$	-	[130]
Nanoporous silicon	100 mm^2	500 μW mm^{-2}	476~514 nm	-	-	[145]
Bi_2Te_3/Sb_2Te_3 nanowires	0.0025 mm^2	~10^4 μW mm^{-2}	0.5~0.75 μm	38 $V\ W^{-1}$	6.1×10^5 $cm\ Hz^{1/2}\ W^{-}$	[89]
$SrTiO_3$	planar junction	≥11.6 mW	0.33~10.67 μm	1.18 $V\ W^{-1}$	-	[98]
Graphene	<1 μm^2	10 μW	0.5~0.9 μm	0.12 $V\ W^{-1}$	-	[120]
Graphene ribbons	4.2 μm^2	0.75 μW	119 μm	10 $V\ W^{-1}$	~2×10^6 $cm\ Hz^{1/2}\ W^{-}$	[91]
CNT fiber PN junction	p-n junction	-	0.41~ 216 μm	0.17 $V\ W^{-1}$	2.2×10^6 $cm\ Hz^{1/2}\ W^{-}$	[146]
Graphene PN junction	several μm^2	a few hundred μW	0.45~1.55 μm	0.19 $V\ W^{-1}$	-	[147]

As longer channel is considered to sustain elevated temperature gradient,[92], [99] an enhanced PTE response is observed with increased CNTF height as shown in Figure 3-8a. The estimated PTE response may increase nearly an order of magnitude if the CNTF could achieve ~mm height as in ref [108] - the typical size of a thermoelectric component. Figure 3-8b shows the measured and predicted photo responsivity R_V correlation with decreasing photosensitive area A (the lateral size of CNTF). It is found that as A decreases from 6 mm^2 to 0.05 mm^2, the photovoltage only sees a slight variation within 7.08 μV to 7.89 μV, but the R_V increases enormously from 14 mV W^{-1} to 1.7 V W^{-1} as calculated by equation (3-3)

$$R_V = \frac{V}{P} = \frac{\int_{bottom}^{top} S(z)\nabla T(z)dz}{A \cdot p_{uniform}} \tag{3-3}$$

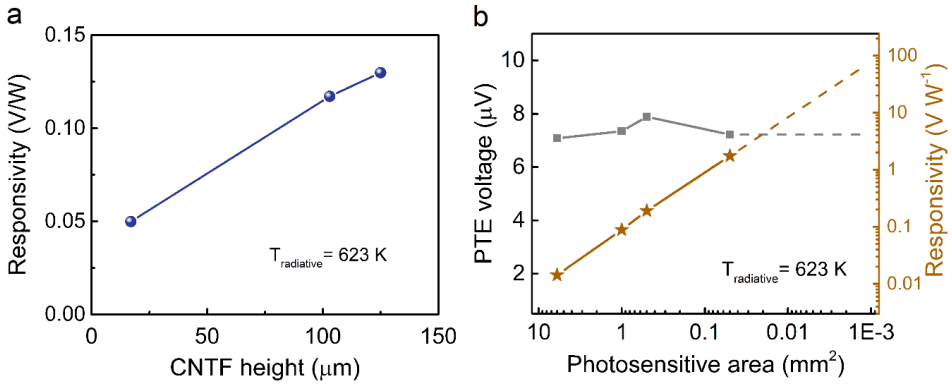

Figure 3-8. Photoresponsivity improvement by optimizing CNTF height and photosensitive area. **a**, Detector responsivity improves with increasing CNTF height. The CNTF heights are 17 μm, 103 μm, and 125 μm, respectively determined by SEM. **b**, The PTE voltage has seen small variation between 7.89 μV and 7.08 μV by decreasing the photosensitive area from 6 mm^2 to 0.05 mm^2, and calculated photoresponsivity increases by 123-folds to 1.7 V W^{-1} correspondingly. Dash lines show the predicted PTE response for even smaller photosensitive areas.

This is because the PTE photovoltage is basically determined by thermal gradient in *z* direction instead of *x*-*y* plane in this 3D architecture. The equivalent circuit of the photodetector is shown in Figure 3-9. The Al covered CNTF acts as a voltage power source, and the whole resistance of the device is the sum of three resistances: $R_{parasitic}$, $R_{substrate}$, and R_{CNTF}. While the PTE voltage is relatively constant as the photosensitive area decreases, we measure an increase in the device resistance: 644 Ohms in 6 mm^2 device, 1084 Ohms in 1 mm^2 device, and 2369 Ohms in 0.05 mm^2 device. This is because less individual CNTs are involved for charge transporting in the circuit-loop after shrinking the CNTF lateral size, leading to higher resistance and reduced photocurrent. Considering the photosensitive

area in this work is much larger than most state-of-the-arts, the photoresponsivity is predicted to further increase in even smaller size device although several reasons could lead to its final degradation.

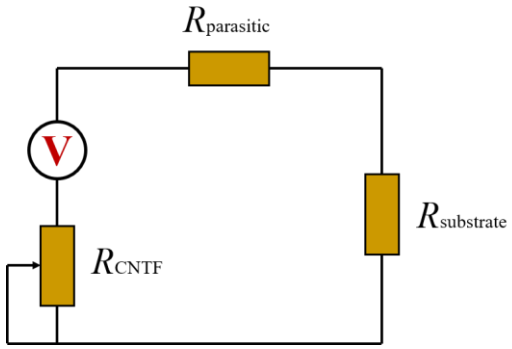

Figure 3-9. Equivalent circuit of the photodetector.

For a broader interest, this photodetector architecture is applicable to the combination of other nanowire arrays (e.g. semiconducting nanowires with higher Seebeck coefficients) and top conductive layers (e.g. MoS_2, black phosphorus) providing a good contact can be formed. Advantages of this vertical PTE junction architecture are in three folds. First, compared to a planar interface PTE detector, the photoresponse in a vertical photojunction is relatively insensitive to illumination spot position, mitigating the optical alignment and focusing requirement. Second, the device compactness is less likely to be compromised when the PTE channel can be extended in vertical direction for heat dissipation, facilitating the integration of a compact detector array. Third, for infrared energy harvesting purpose, the ease of expanding the light-harvesting area brings convenience for enhanced photocurrent collection.

3.6 Conclusion

In summary, we demonstrate a self-powered, large-area and broadband mid-infrared photodetector by employing vertical PTE effect of high-density CNTF with nearly unity black-body absorption properties. A photo detectivity of 2.2×10^{7} cm $Hz^{1/2}$ W^{-1} at 2.5~25 μm spectral range is achieved under weak, unfocused, and broadband infrared illumination (as low as 6.8 μW mm^{-2} at 373 K) akin to realistic world. The photodetectors are implemented through delicate engineering of the top-electrode layer whose material, thickness, and pattern are systematically investigated regarding the PTE effect, while further improvement is possible by increasing CNTF height and decreasing the area. These findings open up possibilities in self-powered, broadband room-temperature infrared detection and energy harvesting for real-time health condition monitoring, low-cost industrial inspection, and distributed sensing/power supplying in Internet of Things.

Chapter 4 Flexible carbon nanotubes/poly vinyl alcohol composite with stable infrared response for wearable imaging

4.1 Background and motivations

Photo-detection technologies are faced with performance degradation and cooling requirement when it comes to mid-infrared (3 μm<λ<50 μm) and Terahertz region (30 μm<λ<3000 μm) where human-body broadband radiation (peak λ=9.3 μm) is located. Room-temperature thermal imaging, which finds growing needs in flexible sensing, energy harvesting and wearable biomedical electronics,[76], [90], [148], [149] has seldom been accomplished, due to the bandgap limit in colloidal quantum-dots[150] (for λ<2.2 μm) and the high frequency roll-off in field-effect transistors[151] (for λ>300 μm). Recently, photo-thermoelectric (PTE) effect detectors have seen rapid progress towards sensitive and room-temperature detection[51], [87], [90], [91], [129], [152], [153] in mid-infrared and THz region, and low-dimensional nanostructured silicon,[145] carbon nanotubes,[97] graphene,[154]–[156] and black phosphorus[130] have been used as PTE conversion materials due to their enhanced photon absorption and thermoelectric conversion.[68] The self-powered, battery-free PTE detectors are in particular desirable as wearable electronics compared to transistors or bolometers[119] since modern wearable systems[150], [157]–[159] are required to be light-weight and miniaturized. Nevertheless, at its infant stage,

current PTE detectors are still limited by the low detectivity, light polarization sensitiveness[51], [91] and poor flexibility.

Herein, we have combined PVA with CNTs to investigate the photo-thermoelectric characteristics of PVA/CNTs composites as mid-infrared detectors using low-cost, lithography-free fabrication methods. Compared to the latest unary nanomaterial detectors,[51], [130], [145], [154] there are certain advancements by utilizing the binary CNTs/PVA composite for a wearable detector. First, the introduction of PVA chains, which wrap around the randomly aligned CNTs network, has effectively reduced the composite thermal conductivity and improved the thermoelectric efficiency by creating phonon scattering sites at PVA/CNTs boundaries.[160], [161] Hence the composite detectors show better biocompatibility,[162]–[164] higher compactness[97] and relatively improved PTE performance,[87], [130], [165]–[170] paving paths to the successful passive body thermal imaging in this work, as well as potential biomedical applications including breast cancer early diagnosis and foot ulcers inspection for diabetic patients.[149] Second, the moderate crystallinity of PVA polymer around CNTs has yielded a balance of mechanical property between the regional rigidity around CNTs and the macroscopic flexibility of composite film.[171], [172] Therefore, the detector's response stability to infrared radiation has been improved compared to pure CNTs or graphene detectors[87], [173] under dramatic and bi-directional bending deformation, which is the top requisite for a flexible sensing or clothes-embedded device that gets bent/wrinkled quite often.

4.2 Photodetector architecture and photoresponse

A symmetric device is first formed by pasting a PVA/CNTs composite thin film (20 wt% CNTs, resistance 81 kΩ, thickness=150 μm, width=2.5 mm, channel length=10 mm) onto two Aluminum plates. By illuminating the left, right, and central part of the channel, ±1.9 nA and 0 nA photocurrents are generated at zero bias, respectively. This is consistent with photo-thermoelectric phenomenon, and to the best of our knowledge, it is the first time found in polymer/carbon nanomaterial composite. However, because this position-dependent detector is bulky and not desired for compact array, asymmetric electrode designs[90], [91], [174] have mitigated this problem by realizing uniform illumination on detector channel. Here, we use low-toxicity and low-cost Al/Ti as electrodes, schematic drawn in Figure 4-1a. 200 nm Aluminum and Titanium electrodes are formed by shadow mask pattern and electron beam evaporation. Lead wires are connected onto electrodes using silver conductive epoxy. Instead of using high-power laser, we use low-intensity blackbody radiation source (Newport Oriel 67030) placed 20 mm away from detectors in order to imitate real-world broadband thermal emission.[152] Blackbody is set from 373 K to 523 K and output power is shown in Figure 4-1a. I-V curves with and without black body illumination are measured by Keithley 6487 pico-ammeter, and photo-voltages are calculated out of measured photocurrents by $V=IR$ for the convenience of comparison.

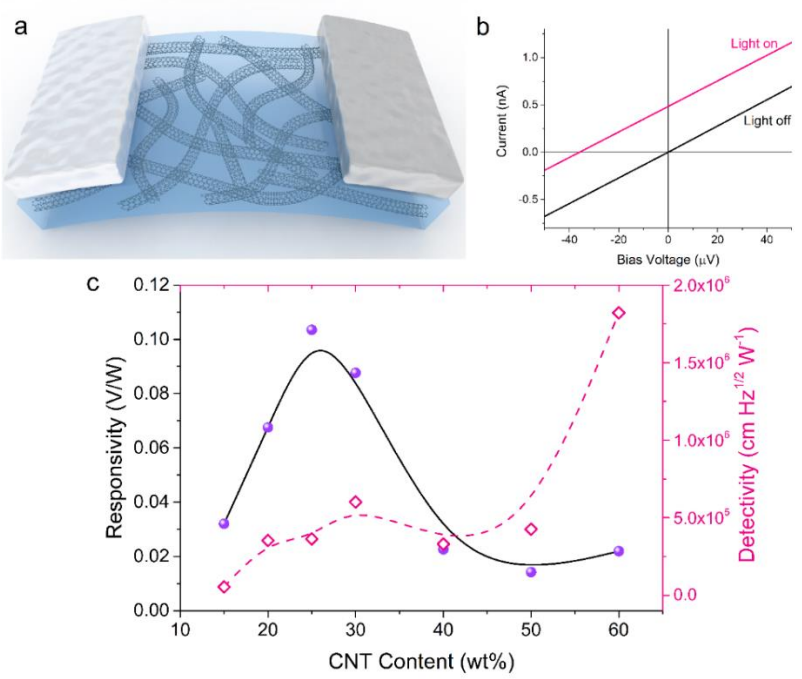

Figure 4-1. a, Scheme of asymmetric electrode detector: Al (left electrode) and Ti (right electrode) formed on bendable PVA/CNTs composite film. **b**, Current-voltage curve with (red) and without (black) 523 K black body illumination in 25 wt.% CNTs device. **c**, Responsivity and detectivity trends with changing CNTs contents. Responses are measured on glass substrate, and all devices are with 0.5 mm channel length.

The current - voltage response curve with and without blackbody irradiation is shown in Figure 4-1b, indicating a net photocurrent under zero-bias condition. Figure 4-1c shows the detector responsivity R_V and detectivity D^* trends with increasing CNTs content among PVA/CNTs composites. The responsivity $R_V = V_{ph} / P_{in}$ reaches a peak of 0.10 V W^{-1} at 25 wt.% CNTs followed by a decline when CNTs content continue to increase. The initial increase of R_V at low CNTs content occurs for two possible reasons: 1) With increasing CNTs content, photon absorption enhancement leads to a higher temperature gradient in the detector channel, and therefore the response is increased; 2) Thermoelectric conversion

efficiency (figure of merit)[166] $ZT = \frac{S^2 \sigma T}{\kappa}$ has been improved due to an increase in electrical conductivity σ, an enhancement of S due to energy filtering effect and the stagnancy of thermal conductivity κ due to interfacial phonon scattering.[175], [176] The following decrease in R_V curve after 25 wt.% CNTs content occurs because of the CNTs aggregation induced ZT reduction.[166] Detectivity is another performance parameter for photodetectors:

$$D^* = R_V \sqrt{A} \sqrt{4 k_B \Delta f T R} \propto R_V \sqrt{A / R} \tag{4-1}$$

Here A is detector area, k_B is the Boltzmann constant, Δf is frequency bandwidth, T is temperature, and R is zero-bias resistance. We can find from equation (4-1) that D^* is proportional to responsivity and inversely proportional to square root of resistance. The pink curve in Figure 4-1c shows the D^* peaks at the 30 wt.% CNTs device, and this is likely to be related to the very high responsivity for this CNTs content. On the other hand, dramatically reduced resistance is assumed the key factor on the major D^* increase for the 60 wt.% CNTs photodetector.

Apart from CNTs content, possible factors affecting a PTE detector performance include source power and substrate materials. For different input source power, stable photo-response is desired in photodetectors. Figure 4-2a shows the constant responsivity (V W^{-1}) of the detector observed under black-body radiation of 373 K, 423 K and 473 K. Corresponding power intensities received by the detector are 40.5 μW mm^{-2}, 84.0 μW mm^{-2} and 146.0 μW mm^{-2}, respectively, and the radiation peak wavelength also shifts from 7.8 μm to 6.1 μm accordingly (indicated in inset of Figure 4-2a).

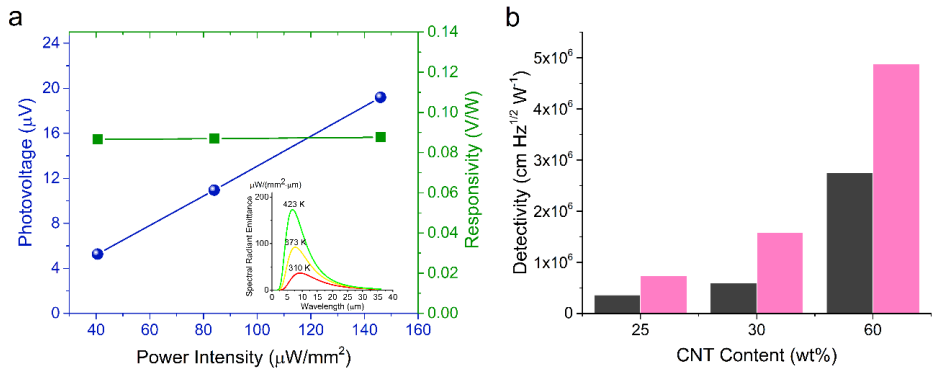

Figure 4-2. a, Responsivity of increasing incident power intensity for 30 wt.% CNTs device (insert shows the black body output intensity at different temperature). **b**, Detectivity comparison between placing detectors on glass substrate and suspending them in air.

Heat dissipation from the channel towards substrate is supposed to influence the performance of PTE detectors due to hot electron cooling effect via substrate surface phonons.[51], [154] Now that previous results were measured by placing devices on glass substrates (thermal conductivity 1.05 W m^{-1} K^{-1}), we expect that thermal conduction loss could be minimized by letting the detectors work as substrate-free. The measurement is carried out by suspending detector channel over 3 mm in air (0.024 W m^{-1} K^{-1}). Figure 4-2b shows that detectivities for 25 wt.%, 30 wt.%, and 60 wt.% devices have increased to 177%, 263% and 203% respectively after suspension. The optimum D^* reaches 1.6×10^6 cm $Hz^{1/2}$ W^{-1} in 30 wt.% CNTs device, and 4.9×10^6 cm $Hz^{1/2}$ W^{-1} in 60 wt.% CNTs device (noise equivalent power is 35 nW $Hz^{-1/2}$), which is comparable or higher than previous room-temperature mid-infrared or THz detector.[51], [97], [130], [153] Orders of magnitude improvement could still be achieved after integrating appropriate antenna[153] and being tested in vacuum.[90]

4.3 Channel length affected photoresponse

There have been debates on asymmetrical structured PTE detectors working mechanism. Herein, we explain that CNTs composite channel as well as metal electrode contributes to the PTE effect: When photons impinge onto the detector, PVA/CNTs composite absorbs photon energy and gets heated up rapidly, while two metal electrodes act as heat sink for being infrared reflective; Because Ti (κ_{Ti}=22 W m^{-1} K^{-1}, S_{Ti}~7 μV K^{-1}) thermal conductivity is a lot lower than Al (κ_{Al}=205 W m^{-1} K^{-1}, S_{Al}~-2 μV K^{-1}), Ti/CNT interface would have higher temperature drop than Al/CNTs interface,[90], [96], [140] and asymmetric temperature gradient is created along the channel. Device temperature $T(x)$ and Seebeck coefficient $S(x)$ profiles is drawn as Figure 4-3a, and photo-voltage is the integration of $S(x)\nabla T(x)$ along device:

$$V_{ph}=\int S_{Al}(x)\nabla T_{Al}(x)dx+\int S_{CNTs}(x)\nabla T_{CNTs}(x)dx+\int S_{Ti}(x)\nabla T_{Ti}(x)dx \qquad (4\text{-}2)$$

Therefore, channel photo-response equals to the net area enclosed by the curve and x axis across the detector: $A+B+C+D$, and A has opposite sign to B, C and D (shown in the bottom drawing in Figure 4-3a).

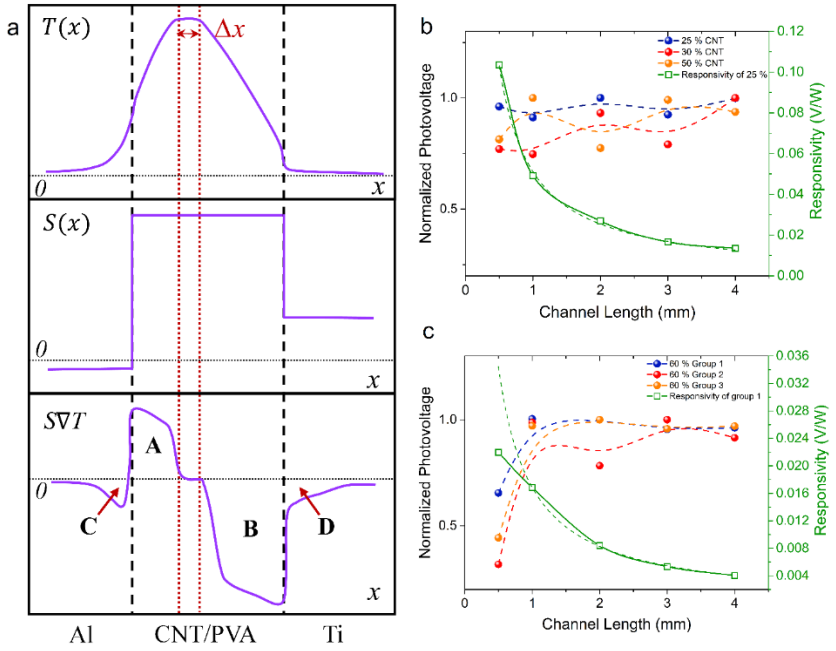

Figure 4-3. a, PTE voltage schematic drawing along device channel position *x*. A, B are areas enclosed by the curve and axis. **b**, **c**, Photo-response dependence on channel lengths for 25 wt%, 30 wt%, 50 wt% and 60 wt% CNTs content (3 groups) detectors.

To figure out the way channel length is affecting PTE performance, we fabricated detectors with five channel lengths: 4 mm, 3 mm, 2 mm, 1 mm, 0.5 mm. For 25 wt.%, 30 wt.%, and 50 wt.% CNTs detectors, stable voltage responses are observed in all channel lengths (as shown in Figure 4-3b). However, for 60 wt.% CNTs detector, photo-voltage shows obvious decrease when it comes to 0.5 mm channel (for all 3 groups, shown in Figure 4-3c). According to $R_v \propto V_{ph}/P_{in}$, the responsivity should be proportional to L^{-1} (channel length) when illumination intensity per area is constant. All experiment results are consistent with the theory, fitted as $R_v \propto L^{-1.01}$ and $R_v \propto L^{-1.03}$ in 25 wt.% and 60 wt.% devices for 4 mm, 3 mm, 2 mm, and 1 mm channel length except for the deviation found for 0.5 mm channel device with 60 wt.% CNTs. We explain this degradation originates

from the incapability of a short channel to maintain high temperature gradient when composite thermal conductivity $\kappa_{channel}$ is increased: When $\kappa_{channel}$ is low (e.g. 15 wt.% CNTs composite), temperature of the channel central region Δx could be constant ($\nabla T=0$, shown in Figure 4-3a) under certain light intensity; When $\kappa_{channel}$ gets higher (for 60 wt.% CNTs composite), the channel peak temperature would be pinned relatively low due to a shorter channel length (0.5 mm), resulting in smaller *A*, *B* areas, and smaller $V_{ph}=A+B+C+D$. One can speculate that for even higher CNTs content or pure CNTs film, detector voltage will be much more restricted by the channel length as well as light intensity. As a result of the low thermal conductivity in a lower CNTs loading detector, however, the pixel size could be made smaller by improving its compactness but without sacrificing performance.

4.4 Flexibility and passive imaging

The combined properties of high flexibility and high response-stability of the detector have been revealed in Figure 4-4, showing stable photo-response at a quite small bending radius. In general, low CNTs content composites demonstrate better flexibility than high CNTs content composites which has intensive porosity. It is also worthy noted that the detector photo-response shows little difference between concave and convex bending[177] (Figure 4-4a), being an important feature for wearable electronics especially for the places like inner and outer elbows. Smallest bending radius we achieve without performance degradation is 3.5 mm in 25 wt.% and 30 wt.% CNTs detectors; 200 bending cycles of 60 wt.% CNTs detector to a 15 mm radius finally prove unaffected performance (Figure 4-4b).

These results show significant improvement compared to a pure CNTs detector,[87] whose CNTs network gets disconnected easily due to weak Van der Waals force, leading to a reduced figure of merit ($ZT \propto \sigma$) and degraded detector response. PVA-CNTs interaction, however, is much stronger than CNT-CNT counterpart as PVA crystallization is moderately enhanced (shown from XRD patterns in Figure 2-7b) in the vicinity of CNTs.[34], [171] The CNTs network is consequently immobilized by its surrounding crystallized PVA, while the rest of uncrystallized PVA chains are functioning to assure the composite flexibility and excessive amount of crystallinity can reduce the flexibility.[172] We interpret it is the moderate crystallinity of PVA in an appropriate CNTs content device (e.g. 25 wt.% CNTs) that enables the high photo-response stability as well as good flexibility for dramatic bending.

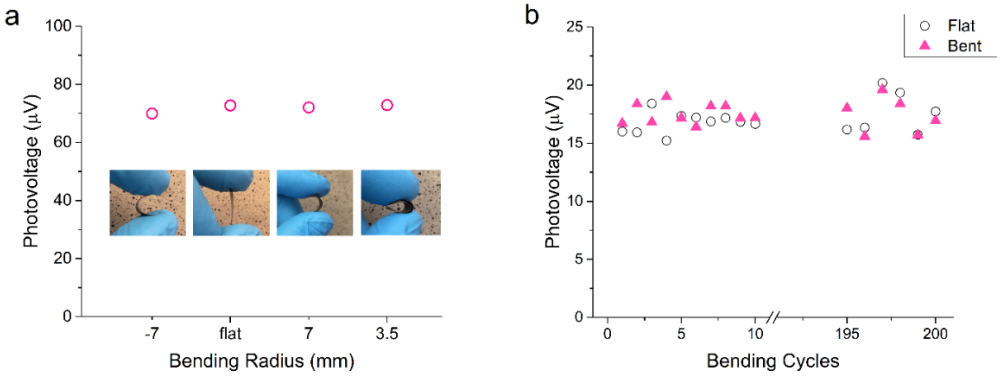

Figure 4-4. Bending response. **a**, Highly-stable photo-response with various bending radius using 25 wt% detector. Negative sign means concave bending and positive sign means convex bending. **b**, 60 wt% CNT detector response under multiple flat and bent cycles at 15 mm bending radius.

Finally, Human-body thermal detection (peak wavelength λ=9.3 μm) is performed using the detector at non-contact mode. By holding a fingertip ~2 mm away from the composite surface, obtained detector response (Figure 4-5a) is relatively fast, and the

thermal emission induced signals, which are comparable to contact-mode temperature sensors,[178] are significantly higher than noise level. Furthermore, Figure 4-5b shows a passive thermal image of two fingers acquired by moving a single pixel detector in a step motor in X-Y plane over a stationary hand. Margin of fingertips could be clearly identified, demonstrating our detector's capability for wearable thermal imaging.

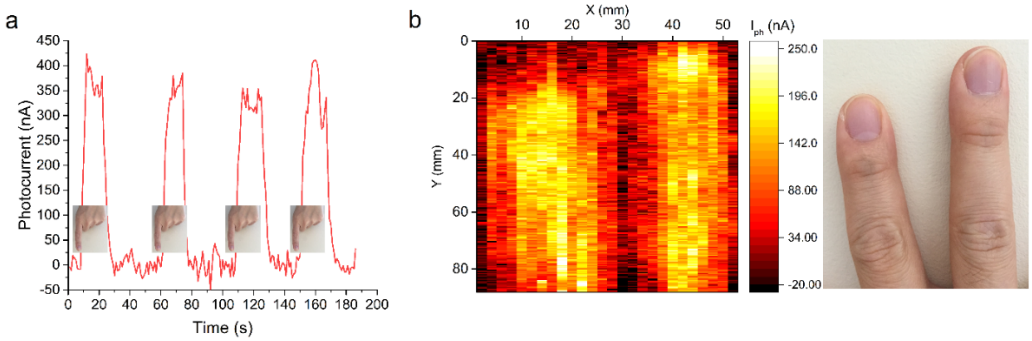

Figure 4-5. a, Repeatable detection of human fingertip radiation placed above detector surface. **b**, Scanned thermal image of the first and middle fingers. The step size in X axis is 2 mm, and scanning speed in Y axis is 0.4 mm/s.

4.5 Conclusion

In summary, PVA/CNTs nanocomposites have been investigated as mid-infrared detectors using simple fabrication method. Detector channel length is found to have influence on the photo-response through Seebeck effect. Stable response is maintained under extreme bending conditions due to immobilized CNTs network supported by PVA crystallization. Bending radius reached 3.5 mm in 30 wt.% CNTs device with a detectivity of 1.6×10^6 cm $Hz^{1/2}$ W^{-1}, and 15 mm in 60 wt.% CNTs device with 4.9×10^6 cm $Hz^{1/2}$ W^{-1}. Finally, a clear image of human fingers is acquired by a passive scanning. This self-

powered and highly flexible thermal detector will find application in wearable electronics, especially real-time health monitoring and fast skin cancer THz imaging.

Chapter 5 A flexible, scalable, and self-powered mid-infrared detector based on transparent PEDOT: PSS/graphene composite

5.1 Background and motivations

Portable and low-cost mid-wave infrared (MWIR, 3–5 μm) and long-wave infrared (LWIR, 8–12 μm) photodetectors meet forthcoming applications in wearable health monitoring electronics, distributed sensor networks in Internet-of-things, and autonomous driving assistants. Traditional mercury cadmium telluride mid-infrared detectors suffer from high material toxicity and fabrication complexity, and state-of-the-art quantum-well photodetectors need be cooled at cryogenic conditions to operate. The advent of novel nanomaterials such as graphene,[91], [179] black phosphorus[118], [180] and molybdenum disulfide[80] have achieved room-temperature photodetection via mechanisms including bolometric effect,[181] photovoltaic effect,[182] photo-thermoelectric effect (PTE),[183]–[185] and plasmon detection.[186] As the first 2-D material, graphene exhibits broadband light absorption due to zero bandgap structure and enhanced thermoelectric properties by virtue of low-dimensionality.[32,33] Based on PTE effect, single-layer graphene achieved photo detectivity of ~2×10^{6} cm $Hz^{1/2}$ W^{-1} at 119 μm, and reduced graphene oxide detector exhibited a maximum 4.6×10^{5} cm $Hz^{1/2}$ W^{-1} detectivity in a broadband range from 0.37 to 118 μm.[91], [185] Even though large-area

graphene growth can be achieved by chemical vapor deposition,[187] high-quality single-layer graphene is expensive for scalable fabrication and fragile to manipulate. CNTs are also ideal PTE materials[26,36–39] and Suzuki *et al.* exemplified a CNT based 1-D detector array for far-infrared imaging with a noise equivalent power less than 1 nW $Hz^{-1/2}$.[90] But drawbacks of pure CNT film detectors are the visible opacity and unstable photocurrent under deformation due to weak Van der Waals interaction between nanotubes.[92]

Modern optoelectronic system expect photodetectors to be low cost and have novel functionalities to accommodate broader applications.[25], [40], [188] Polymer based photodetectors are therefore receiving growing attentions in visible and near-infrared range by now due to solution processability, high flexibility, and good transparency.[189]–[191] PTE conversion is proved with 0.9 mV photovoltage output under 2.3 W cm^{-2} near-infrared excitation in a flexible and transparent hexyl-3,4-ethyl-enedioxyselenophene,[192] - the derivative of PEDOT: PSS which is also investigated as thermoelectric material.[28], [193] For MWIR/LWIR regimes, however, polymer based PTE detectors had been vacant until the report of PVA/CNT composite detector by our group in 2018.[92] The rationales of polymer composite based detectors include facile fabrication, improved sensitivity and better flexibility: the composite detector exhibits negligible response variation at 3.5 mm bending radius while the responsivity sees several times improvement with detectivity of 4.9×10^{6} cm $Hz^{1/2}$ W^{-1}, attributed to the interface phonon scattering and energy filtering effects.[35], [73], [194]–[196] However, PVA/CNT composite is opaque and unoptimized due to aggregation induced high CNT loading.[32], [92], [197]

In this work, we have developed a unique and facile fabrication technique towards a flexible, scalable, self-powered, and semi-transparent mid-infrared photodetector using PEDOT: PSS/graphene composite. An optimized photoresponse is achieved at a low loading of graphene (3 wt.%) in polymer composite and 1.4×10^{7} cm $Hz^{1/2}$ W^{-1} photo detectivity under broadband mid-infrared radiation has been measured in an asymmetric PTE architecture. To the best of our knowledge, this is the firstly demonstrated flexible, semi-transparent, and self-powered mid-infrared photodetector to date.

5.2 Photodetector fabrication and photoresponse

On top of the PEDOT: PSS/graphene composite we described in chapter 2.3, 200 nm Aluminum and 25 nm ITO (indium tin oxide) electrodes are formed via shadow mask patterning and magnetron sputter deposition, as shown in Figure 5-1a. No photo lithography or e-beam lithography has been used. For the semi-transparent devices, thinner electrode layers - 25 nm or 15 nm Al, and 25 nm ITO are used instead. A 13×13 pixeled detector array has been fabricated using this shadow mask technique and the pixel size (period) is 2.8 mm. The electrodes in the array are 15 nm Al and 25 nm ITO. Instead of using high-power laser, we use low-intensity, broadband blackbody radiation source (Newport Oriel 67030) in order to imitate the real-world mid-infrared emission. The black-body temperature is set from 373 K to 573 K with an opening spot diameter of 0.5 cm or 1 cm, and the photodetectors to be measured are placed 25 mm away. The I−V characteristics with and without black-body illumination were measured by a Keithley 6487 pico-ammeter.

The photo-thermoelectric voltages at zero-bias were calculated from measured photocurrents by $V = IR$ where R represents resistance of the device.

Figure 5-1a, c illustrates the fabrication process and schematic of PEDOT: PSS/graphene composite based mid-infrared photodetector. The temporal response of the device on Kapton substrate is shown in Figure 5-1b. The blackbody source is set at 573 K and the detector received power density is 225 μW mm^{-1}. As our detector is in a large physical scale and based on thermal mechanism[92], a relatively long photocurrent transition time of 15 ~30 s is measured. A stable photocurrent response can be achieved when a thermal gradient has been established among the device channel, the substrate and the environment. Figure 5-1d shows the current-voltage curves of the photodetector under dark condition and under 573 K blackbody illuminated condition, and a net photocurrent can be observed at zero-bias.

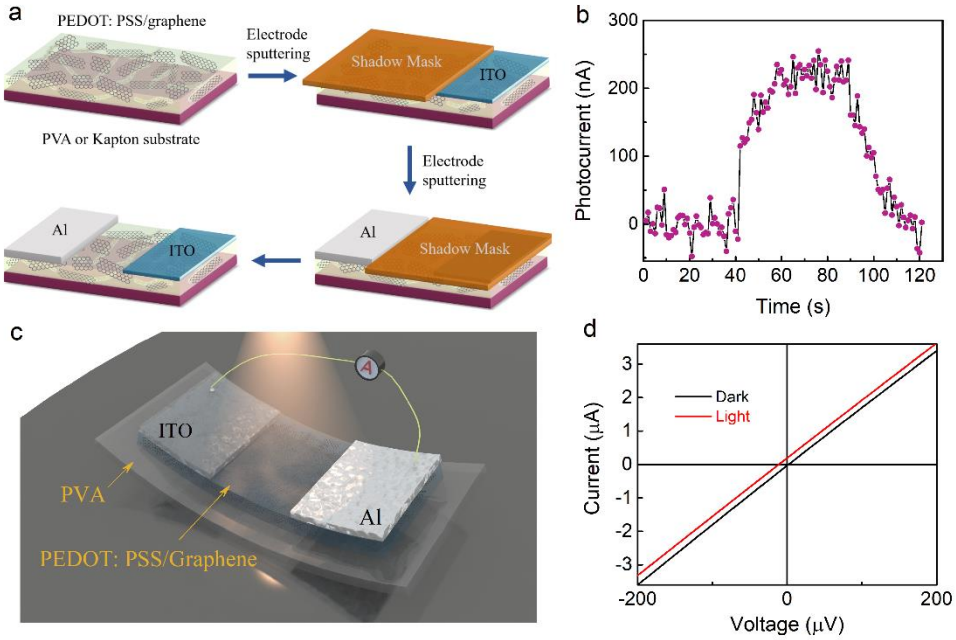

Figure 5-1. a, Non-lithographic fabrication processes of the PEDOT: PSS/graphene based photodetector. **b**, Temporal response of 3 wt.% graphene loading photodetector under 225 μW mm^{-1} blackbody radiation. **c,** Schematic of the flexible, semi-transparent infrared detector. **d**, I-V curves of the photodetector measured in the dark and under blackbody illumination.

The photo-thermoelectric characteristics of PEDOT: PSS/graphene detectors have been investigated by tuning the graphene nanoplatelets content within composite. As shown in Figure 5-2a, detectivity $D^*=R_v\sqrt{A}/\sqrt{4k_BTR}$ is used to evaluate the photodetector performance where A is photosensitive area, k_B is Boltzmann constant, T is temperature, and R is resistance. D^* represents the capability of detector to identify the weakest photo signal from the noise. For a pure PEDOT: PSS (0 wt.% graphene) device, the detectivity is measured to be only 5.9×10^5 cm Hz$^{1/2}$ W^{-1} at 55 μW mm^{-1} radiation. By increasing the graphene content to 3 wt.%, the detectivity increases by 22 folds to 1.3×10^7 cm Hz$^{1/2}$ W^{-1} under the same illumination condition. We explain this phenomenon to be the result of the

enhanced photo absorption at elevated graphene content, and the optimized thermoelectric efficiency at 2~3 wt.% graphene loading as reported by literature of PEDOT: PSS composite.[114], [197], [198] When the graphene content increases from 3 wt.% to 12.5 wt.%, a reduced photoresponse is observed attributed to a lower Seebeck coefficient due to increased carrier concentrations[114], [197] as illustrated by equation (5-1).

$$S = \frac{8L}{h^2} m^* T \left(\frac{\pi}{3n} \right)^{2/3} \tag{5-1}$$

where $L = \pi^2 k_B{}^2 / 3e^2$ is the Lorentz number, h is Planck constant, m^* is effective mass of the carrier, and n is carrier concentration. The optimized PTE performance can be achieved at such low graphene content because the PEDOT: PSS chains have facilitated the dispersion of graphene. A strong π-π interaction exists between the 2-D graphene nanoplatelets and the planar backbone of PEDOT, and an intermolecular electrostatic repulsive force also exists between PSS and the graphene.[197] As a comparison to PEDOT: PSS/CNTs composite, the optimized CNTs loading is much higher - typically 35 wt.%, due to the bundling and aggregation effect of cylindrical CNTs.[27], [197] The low requisite loading for graphene filler not only improves the biocompatibility[164][162] and reduces material cost, but also exhibits great potential in the integration of optically transparent and ultra-flexible devices.

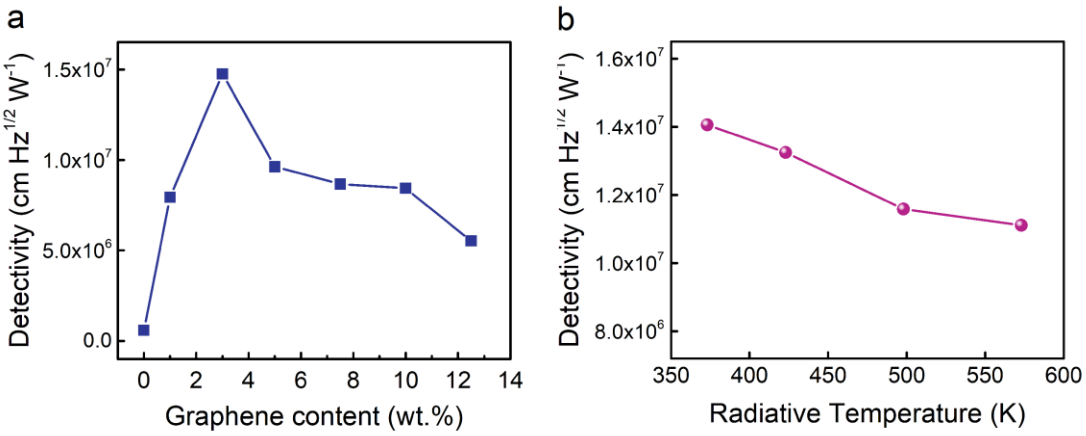

Figure 5-2. a, Photodetector detectivity correlation with the increasing graphene content within the PEDOT: PSS/graphene composite. The graphene nanoplatelets loadings are 0 wt.%, 1 wt.%, 3 wt.%, 5 wt.%, 7.5 wt.%, 10 wt.%, 12.5 wt.%, respectively. **b**, The photoresponse of 3 wt.% graphene photodetector at different blackbody radiation temperatures. While the radiative temperatures are 373 K, 423 K, 498 K, 573 K, the detector received power densities are 26.5 μW mm^{-1}, 54.9 μW mm^{-1}, 121 μW mm^{-1}, 225 μW mm^{-1}, respectively.

Figure 5-2b shows the photodetector responses under different blackbody radiation conditions. As the temperature of blackbody source decreases from 573 K to 373 K, i.e. the detector received power density deceases from 225 μW mm^{-1} to 26.5 μW mm^{-1}, the detector photoresponse sees a slight increase from 1.1 ×10^7 cm Hz$^{1/2}$ W^{-1} to 1.4×10^7 cm Hz$^{1/2}$ W^{-1}. Compared to our previous work which used PVA polymer containing 60 wt.% CNTs, the detectivity here shows an improvement of 2.9 folds. There are two reasons for this credit: 1) The optimized electrode design – substituting 200 nm Ti with 25 nm ITO has enhanced the PTE asymmetry in contrast to the 200 nm Al electrode;[199] 2) The better dispersion of graphene filler within the polymer matrix has contributed to a higher thermoelectric conversion efficiency compared to the CNTs composite.[197]

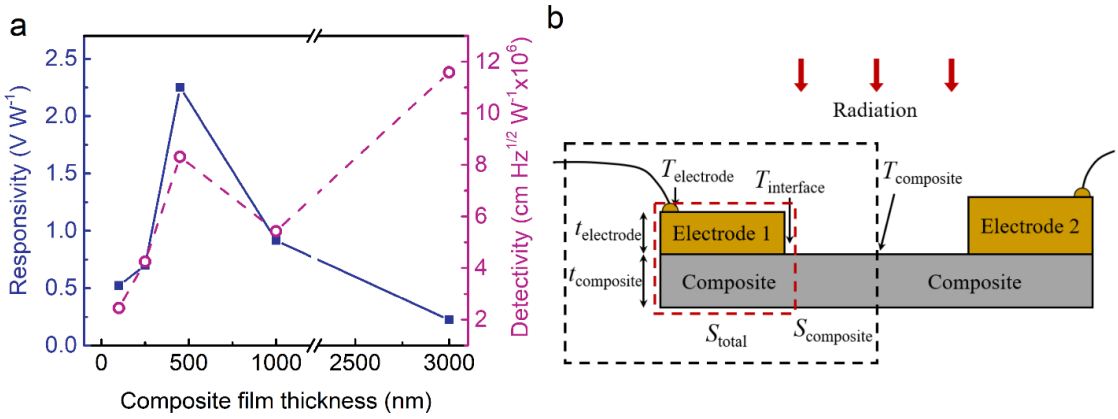

Figure 5-3. a, Photoresponsivity correlation with PEDOT: PSS/graphene composite film thickness. The electrodes are 25 nm Al and 25 nm ITO. **b**, A schematic of the detector response related with some of the physical parameters.

We further investigated the photoresponse of spin-coated PEDOT: PSS/graphene composites on PVA substrate at various spin speeds where different composite film thicknesses are obtained. The as-prepared PEDOT: PSS/3 wt.% graphene solution is spin-coated at speeds of 500 rpm, 100 rpm, 1500 rpm, and 2000 rpm and the corresponding thicknesses are 1 μm, 450 nm, 250 nm and 100 nm, respectively. The film thickness obtained by drop-casting is between 2~4 μm (3 μm is used here). In general, thinner films exhibit higher optical transparency but also higher electrical resistance. Figure 5-3a shows the photoresponse correlation with different thicknesses of the composite. An optimized detector responsivity is found in the 450 nm thick film obtained at 1000 rpm spin coating speed. The responsivity dependence on composite film thickness could be understood by a theoretical model.[199]:

$$V_{half} = S_{\text{total}}(T_{\text{electrode}} - T_{\text{interface}}) + S_{\text{composite}}(T_{\text{interface}} - T_{\text{composite}}) \quad (5\text{-}2)$$

$$S_{\text{total}} = \frac{\sigma_{\text{electrode}} t_{\text{electrode}} S_{\text{electrode}} + \sigma_{\text{composite}} t_{\text{composte}} S_{\text{composite}}}{\sigma_{\text{electrode}} t_{\text{electrode}} + \sigma_{\text{composite}} t_{\text{composite}}} \quad (5\text{-}3)$$

where V_{half} is the photo voltage generated by half of the photodetector as shown in Figure 5-3b, S_{total} is the combined Seebeck coefficient of the electrode and composite underneath (substrate included), $T_{\text{interface}}$ is the temperature at the electrode/composite interface, and $T_{\text{electrode}}$ and $T_{\text{composite}}$ are temperatures at the two farther ends of the electrode and composite, respectively. Equations (5-2) and (5-3) indicate that the thicknesses of the electrode and composite are directly and indirectly correlated to the thermoelectric voltage in several ways – their respective thickness could affect the light absorption and temperature distribution along the channel, and the ratio of them determines the S_{total}. Another possible reason for the low photoresponse in thinner films is the distribution of graphene nanoplatelets (~2 μm diameter) within polymer matrix become worse after spin coating at high speed (i.e. 100 nm thick) and leads to lower photo absorption and thermoelectric conversion. The high detectivity of the 3000 nm thick composite (drop-casted) device is attributed to the much lower electrical resistance due to $D^* \propto R^{-1/2}$.

5.3 Flexible and semi-transparent photodetector

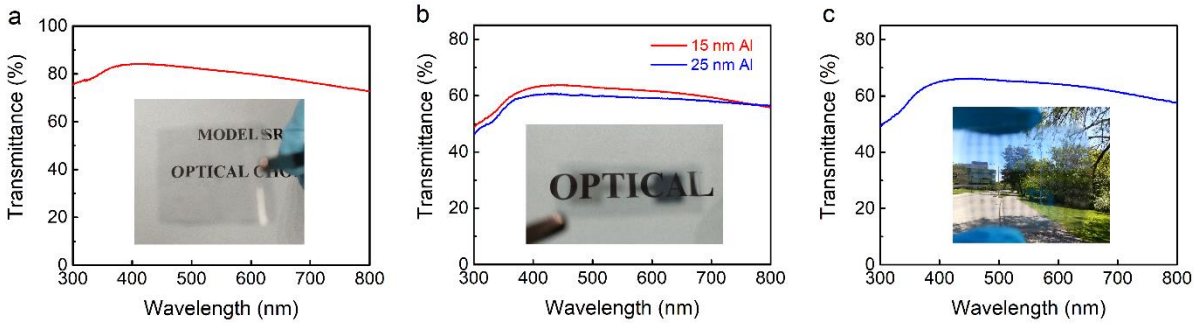

Figure 5-4. Transparent composite and semi-transparent photodetectors. **a**, The UV-Vis spectrum and optical image of the PEDOT: PSS/graphene composite on PVA substrate in visible range. **b**, The UV-Vis spectra of composite based photodetectors with 15 nm/25 nm Al and 25 nm ITO as electrodes. The optical image is the 15 nm Al electrode based device. **c**, The UV-Vis spectrum and optical image of a 13×13 pixeled detector array.

Semi-transparent photodetectors based on transparent composite and substrate are demonstrated by transferring the spin-coated PEDOT: PSS/graphene composite onto PVA substrate and integrating electrodes with reduced thicknesses. An optical image and UV-Vis transmittance spectrum of the PVA supported composite is shown in Figure 5-4a, and the average optical transmittance in the 300 nm ~ 800 nm range is 80%. For photodetector devices with 15 nm and 25 nm Al electrodes (25 nm ITO), the average optical transmittances are 60% and 58%, respectively (Figure 5-4b), and optical transmittance of a 13×13 pixeled detector array is 62% (Figure 5-4c). Considering the Al skin depth of 5 μm infrared waves is around 10 nm, the thinnest Al layer here - 15 nm still functions to block the incident light as a thicker electrode does. However, the optical transmittance of 15 nm Al film is around 10%,[200] which is main limitation of the detector transparency. A possible way to further increase the electrode optical transmittance is to replace the continuous film with conductive nanowires network. As discussed above, various

composite and electrode thickness combinations yield different photoresponse.[90] For thinner Al electrode thickness, the photo detectivity has seen some degradation compared to 1.4×10^7 cm $Hz^{1/2}$ W^{-1} detectivity in the 200 nm Al device, but still achieves 8.3×10^6 cm $Hz^{1/2}$ W^{-1} in the 25 nm Al, 25 nm ITO device and 7.0×10^6 cm $Hz^{1/2}$ W^{-1} in the 15 nm Al, 25 nm ITO device. A comparison between this work and representative room temperature MWIR/LWIR detectors is shown in Table 5-1.

Table 5-1. Comparison between this work and representative MWIR/LWIR photodetectors.

Ref.	Photodetection Materials	Detection Mechanism	Responsive wavelength	Responsivity	Detectivity	Bias Voltage	Flexibility	Transparency
This work	Drop-casted PEDOT: PSS/graphene	PTE	2.5~25 μm (7.8 μm)	0.27 V W^{-1} @2.5~25 μm	1.4×10^7 cm $Hz^{1/2}$ W^{-1}	0	Flexible	-
	Spin-coated PEDOT: PSS/graphene	PTE	2.5~25 μm (7.8 μm)	1.9 V W^{-1} @2.5~25 μm	7.0×10^6 cm $Hz^{1/2}$ W^{-1}	0	Ultra-flexible	63%
[98]	$SrTiO_3$/Ag interface	PTE	0.3~10.7 μm	1.18 V W^{-1} @10.67 μm	-	0	-	-
[185]	Reduced Graphene Oxide/Au interface	PTE	0.37~118 μm	0.09 V W^{-1} @10.67 μm	4.6×10^5 cm $Hz^{1/2}$ W^{-1}	0	-	~2%
[201]	$EuBiSe_3$/Au interface	PTE	0.37~118 μm	~1 V W^{-1} @10.6 μm	$\sim1.7\times10^8$ cm $Hz^{1/2}$ W^{-1}	0	-	-
[202]	Graphene with antenna	Photo-Conductive	4.45 μm	0.4 V W^{-1} @4.45 μm	-	0.6 V	-	-
[118]	Black phosphorus	Photo-Conductive	3.4~7.7 μm	2.2 mA W^{-1} @7.7 μm	-	1.2 V	-	-
[82]	HgTe CQDs	Photo-Conductive	3~5 μm	–	$\sim1\times10^7$ cm $Hz^{1/2}$ W^{-1}	0.5 V	-	-
[91]	Graphene Ribbons	PTE	119 μm	10 V W^{-1} @119 μm	$\sim2\times10^6$ cm $Hz^{1/2}$ W^{-1}	0.2 V	-	-
[146]	CNT Fiber PN junction	PTE	0.4~216 μm	0.17 V W^{-1} @4.53 μm	2.2×10^6 cm $Hz^{1/2}$ W^{-1}	0	Ultra-flexible	-
[92]	CNTs/PVA composite	PTE	2.5~25 μm (7.8μm)	0.10 V W^{-1} @2.5~25 μm	4.9×10^6 cm $Hz^{1/2}$ W^{-1}	0	Flexible	-

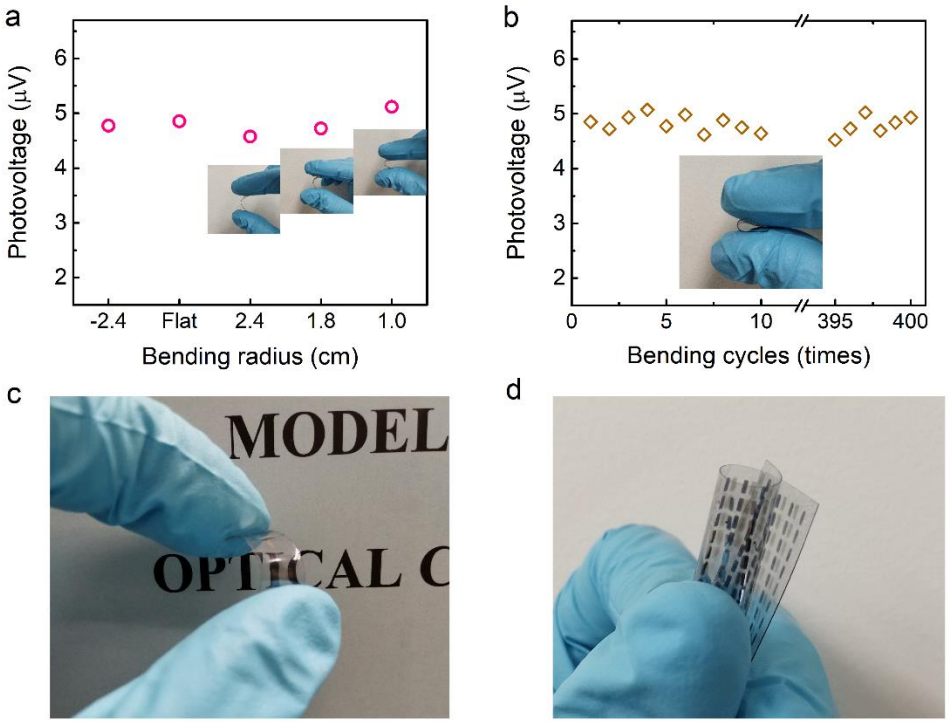

Figure 5-5. Bending properties of PEDOT: PSS/graphene based photodetectors. **a**, The photovoltage outputs of a device on Kapton substrate at convex bending of 2.4 cm, 1.8 cm, 1.0 cm radiuses, and concave bending of 2.4 cm radius. **b**, Some photovoltage outputs during 400 times bending to 1 mm radius. **c**, **d**, Optical images of the flexible detector and array.

The PEDOT: PSS/graphene detector exhibits excellent flexibility and stable photoresponse under bending deformation. Figure 5-5a shows the photoresponse at different bending radius in a 3 wt.% graphene device on Kapton substrate obtained by drop-casting deposition. The photoresponse sees a small variation under bent conditions even for a significant bending of 1 cm radius. The relatively stable response is assumed to originate from the strong interaction between graphene filler and polymer matrix which keeps the electrical and thermal transport paths stable.[92] However, due to the excessive film thickness and weak substrate interaction, some cracks appeared on the composite film

after 100 times bending. This issue has been mitigated in the spin-coating deposited composite film on flexible PVA substrate. Figure 5-5b shows the photoresponse outputs of a spin-coated composite on PVA substrate during 400 times of bending deformation. The flexible substrate and thin composite film have enabled quite small bending radius below 1 mm (Figure 5-5c, d).

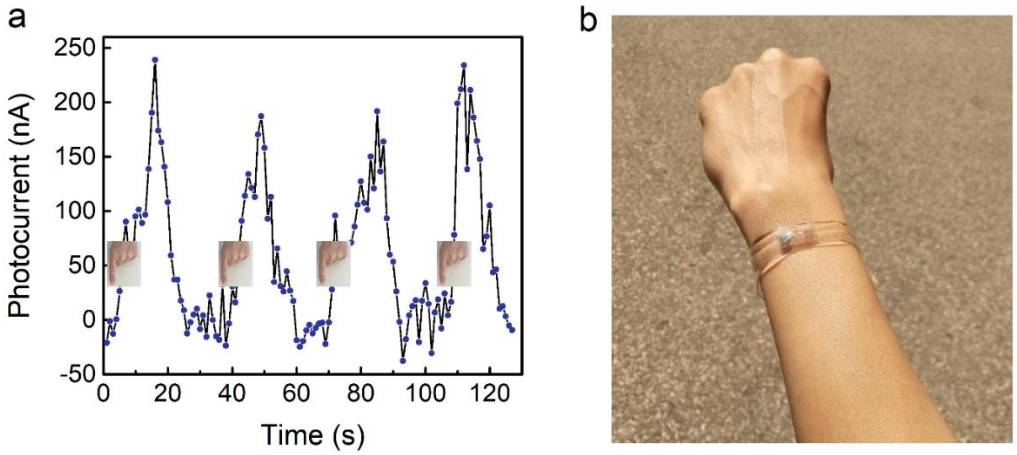

Figure 5-6. a, Repeated detection of a human fingertip radiation placed non-contact above the detector surface. **b**, A flexible photodetector integrated transparent wrist belt.

Finally, human-body passive radiation detection is performed using the PEDOT: PSS/3 wt.% graphene detector. Similar to the blackbody source we use for characterization, thermal emission from human-body is a broadband radiation covering MWIR and LWIR regimes having peak wavelength at 9.3 μm. A notable photocurrent is observed under the unfocused, spontaneous body emission when the fingertip is placed ~2 mm away from the detector as shown in Figure 5-6a. This demonstrates the possible functionality of this device as wearable optoelectronics since the fluctuation of body radiation could be reflected in the change of photocurrent. Figure 5-6b presents a flexible, transparent

wristband integrated with a single-pixel PEDOT: PSS/graphene detector. By tracking the variation of body emission, the wristband can serve as a wearable monitor for the sleep health condition.[203], [204] Wearable MWIR/LWIR detectors can also diagnose breast or skin cancers and foot ulcerations attributed to the infrared radiation change from the body at their very early occurrence.[75], [149] We consider our photodetector have advantages in terms of comfort, convenience, and integration compared to skin-touching, rigid, and battery-driven temperature sensors. Furthermore, Figure 5-7a-c show possible applications of a flexible and semi-transparent 13×13 pixeled detector array, which is proposed as part of the gesture recognition system inside vehicles as a supplement to the current ultrasound transducers, or as photodetector/energy-harvester installed on the car windshield of the environmental MWIR/LWIR radiation. Since the infrared emissivity of various matters such as bio-tissues are different (even under the same temperature), the detector array could also be integrated onto glasses/contact lens and serve as eyeball tracking device under dark conditions.

Figure 5-7. A detector array placed **a**. inside a vehicle, **b**. on the windshield, **c**. on glasses.

5.4 Conclusion

In summary, PEDOT: PSS/graphene composite mid-infrared photodetectors have been demonstrated based on self-powered photo-thermoelectric effect. This flexible, semi-transparent, and sensitive photodetector is fabricated by a unique, scalable method. The best photo detectivity of 1.4×10^{7} cm $Hz^{1/2}$ W^{-1} is achieved at a graphene loading of 3 wt.% within PEDTO: PSS. High flexibility at the bending radius of 1 mm, high optical transmittance - 80% for the composite and 63% for detector array have been achieved. These photodetector functionalities could open new possibilities of next-generation optoelectronics for applications in Internet-of-things sensors, wearable biomedical electronics, and autonomous driving assistants.

Chapter 6 Summary and outlook

6.1 Summary

Room temperature and low-cost MWIR/LWIR photodetectors meet upcoming wearable health condition monitoring, fast industrial inspection and distributed sensors/power-sources for Internet-of-things. The current issues which are hindering these infrared optoelectronics from widespread applications include the material toxicity of heavy element MCT detectors, the cryogenic cooling requirement for III-V semiconductors, the inefficient light-absorption in 2D materials (2.3% in graphene, ~3% in black phosphorus), the expensive photolithography and e-beam lithography patterning of electrodes, the non-scalable production of light sensitive materials, as well as the material and device mechanical rigidity against deformation. In this thesis, we have developed two architectures and three categories of room-temperature MWIR/LWIR photodetectors based on photo-thermoelectric effect, aiming to mitigate above mentioned limitations.

Chapter 2 introduces the synthesis methods we have developed and characterization results of three large-area, scalable, and relatively low-cost light absorbing materials, i.e. the vertically aligned carbon nanotubes forest, the CNTs/PVA composite film, and the PEDOT: PSS/graphene nanoplatelets composite film.

Chapter 3 describes a self-powered, large-area and broadband mid-infrared photodetector by employing vertical photo-thermoelectric effect of high-density CNTF with nearly unity black-body absorption. A photo detectivity of 2.2×10^{7} cm $Hz^{1/2}$ W^{-1} at 2.5~25 μm spectral range is achieved under weak, unfocused, and broadband infrared

radiation akin to the real-world illumination. The photodetectors are integrated through the engineering of the top-electrode layer, the material, thickness, and pattern of which are investigated regarding the PTE effect. A further response improvement is demonstrated by increasing CNTF height and decreasing the photosensitive area. These findings open up new possibilities in broadband infrared detection and energy harvesting for real-time health condition monitoring, low-cost industrial inspection, and distributed sensing/power supplying in Internet of Things.

Chapter 4 presents that PVA/CNTs nanocomposites have been investigated as mid-infrared detectors using solution processing and non-lithographic fabrication method. The detector channel length correlation with the photo-response has been revelled through the Seebeck effect. Stable response is observed under significant convex and concave bending (to 3 mm radius) attributed to the immobilized CNTs network supported by PVA crystallization. An image of human fingers is obtained by a passive scanning the single-pixel detector. This self-powered and highly flexible MWIR/LWIR detector will find application in wearable electronics especially for real-time health monitoring and fast skin cancer THz imaging.

Chapter 5 introduces the PEDOT: PSS and graphene composite based mid-infrared photodetectors, which is the second-generation of the CNTs/PVA composite. The optimized photo detectivity of 1.4×10^{7} cm $Hz^{1/2}$ W^{-1} is achieved at a graphene loading of 3 wt.% within the composite, compared to the 4.6×10^{6} cm $Hz^{1/2}$ W^{-1} in a 60 wt.% CNTs content PVA composite. The low loading of graphene filler has also enabled the realization of a flexible and semi-transparent detector, which has been achieved by spin coating the

composite solution onto a PVA substrate. Good photoresponse stability against bending deformation have been proved due to strong interaction between graphene and PEDOT: PSS matrix. This sensitive, flexible, semi-transparent, and low-cost detector could find a variety of applications as Internet-of-things sensors, wearable biomedical electronics, and autonomous driving assistants.

6.2 Outlook

Currently, the study of our photodetectors is still at early stage and lots of work can be done to further improve the photodetection performance and advance the integration and utilization of these kinds of photodetectors towards practical scenarios.

1) Optimizing the channel dimensions

As discussed before, since increased CNTF height will help improve the PTE response, the CNTF growth parameters can still be optimized in order to extend its height. By introducing small amount of water into the reactor chamber during fabrication or adding a very thin layer of molybdenum on top of the Fe catalyst layer could be two of the possible methods to boost CNTs growth to even millimeter scale.[108], [205]

The optimized channel widths (perpendicular to the carrier transport direction) in CNTs/PVA and PEDOT: PSS/graphene detectors have not been investigated. By referring to the irrelevant correlation between the photosensitive-area and output voltage in CNTF based detector, the channel widths of the planar detector architecture will probably not influence the photo-thermoelectric voltage either.

2) Novel 2D materials as the top-electrode layer

For now, the 25 nm Al top-electrode layer has achieved the best photoresponse in CNTF based detectors. However, strong light reflection and relatively low Seebeck coefficient of metals have probably not made Al the ultimately best option. According to our results that good electrical and thermal contact matter significantly for the PTE response, novel 2D conducting materials who have lower infrared reflection and tunable Seebeck coefficients such as graphene, MoS_2, and black phosphorous could also be utilized as the top-electrode layer should fair contacts can be formed with the CNTF.

3) Integration of focal plane array

While a single-pixel detector has been used in imaging demonstration and a 13 by 13 pixels array has only been fabricated but not packaged or tested yet, the integration and testing work of a focal plane array with readout circuitry needs to be carried out. During this process, there must be some trade-offs among the detector pixel density (period), the photoresponse (as shorter channel probably leads to reduced response), and the shadow mask pattern lower limit.

4) Calibration of the detector output to body temperature

If the flexible photodetectors are to be used as wearable health monitors which constantly measures the infrared/THz radiation from human bodies, the light induced current outputs need to be calibrated to the real body temperature. After doing so, by

reading the photodetector output current, a digital signal processor (DSP) can provide the real-time temperature values of our bodies onto the electronic display.

5) Improve the device endurance

The long-term reliability of this photodetectors needs to be improved. The photoresponse degradation in a CNTs/PVA composite detector is ~35% after 6 months by placing the device under ambient conditions. This is most likely caused by the metal electrode oxidation as evidenced by the visual color change, followed by reason of polymer degradation. Possible measures to slow down the degradation process and improve device endurance may include covering the device with PMMA protection layer or depositing a thin layer of noble metal on top of the two electrodes in order to reduce the moisture and O_2 corrosion.

Bibliography

[1] S. Iijima, "Helical microtubules of graphitic carbon," *Nature*, vol. 354, no. 6348, pp. 56–58, 1991.

[2] K. S. Novoselov *et al.*, "Electric field effect in atomically thin carbon films," *Science*, vol. 306, no. 5696, pp. 666–669, 2004.

[3] C. Lee, X. Wei, J. W. Kysar, and J. Hone, "Measurement of the Elastic Properties and Intrinsic Strength of Monolayer Graphene," *Science*, vol. 321, no. July, pp. 385–388, 2008.

[4] A. A. Balandin *et al.*, "Superior thermal conductivity of single-layer graphene," *Nano Lett.*, vol. 8, no. 3, pp. 902–907, 2008.

[5] K. S. Novoselov *et al.*, "Two-dimensional gas of massless Dirac fermions in graphene," *Nature*, vol. 438, no. 7065, pp. 197–200, 2005.

[6] M. Wilson, "Electrons in atomically thin carbon sheets behave like massless particles," *Phys. Today*, vol. 59, no. 1, pp. 21–23, 2006.

[7] S. V. Morozov *et al.*, "Giant intrinsic carrier mobilities in graphene and its bilayer," *Phys. Rev. Lett.*, vol. 100, no. 1, pp. 11–14, 2008.

[8] K. S. Novoselov, V. I. Fal′ko, L. Colombo, P. R. Gellert, M. G. Schwab, and K. Kim, "A roadmap for graphene," *Nature*, vol. 490, no. 7419, pp. 192–200, 2012.

[9] F. Bonaccorso, Z. Sun, T. Hasan, and a. C. Ferrari, “Graphene Photonics and Optoelectronics,” *Nat. Photonics*, vol. 4, no. August, pp. 611–622, 2010.

[10] X. Lu and Z. Chen, “Curved Pi-conjugation, aromaticity, and the related chemistry of small fullerenes (<C60) and single-walled carbon nanotubes,” *Chem. Rev.*, vol. 105, no. 10, pp. 3643–3696, 2005.

[11] Y. Wu, X. Zhang, A. Y. T. Leung, and W. Zhong, “An energy-equivalent model on studying the mechanical properties of single-walled carbon nanotubes,” *Thin-Walled Struct.*, vol. 44, no. 6, pp. 667–676, 2006.

[12] S. Berber, Y.-K. Kwon, and D. Tomanek, “Unusually high thermal conductivity of carbon nanotubes,” *Phys. Rev. Lett.*, vol. 84, no. 20, pp. 4613–4616, 2000.

[13] J. Hone *et al.*, “Electrical and thermal transport properties of magnetically aligned single wall carbon nanotube films,” *Appl. Phys. Lett.*, vol. 77, no. 5, pp. 666–668, 2000.

[14] A. E. Aliev, M. H. Lima, E. M. Silverman, and R. H. Baughman, “Thermal conductivity of multi-walled carbon nanotube sheets: radiation losses and quenching of phonon modes.,” *Nanotechnology*, vol. 21, no. 3, p. 035709, 2010.

[15] M. Law, H. Kind, B. Messer, F. Kim, and P. Yang, “Transparent, Conductive Carbon Nanotube Films,” *Science*, vol. 305, no. August, pp. 1273–1276, 2004.

[16] T. Chen *et al.*, “Nanotube Fibers for a Highly Efficient Solar Cell **,” *Angew. Chemie - Int. Ed.*, vol. 50, pp. 1815–1819, 2011.

[17] Y. Jia *et al.*, “Achieving High Efficiency Silicon-Carbon Nanotube Heterojunction Solar Cells by Acid Doping,” *Nano Lett.*, vol. 11, pp. 1901–1905, 2011.

[18] M. W. Rowell, M. A. Topinka, M. D. Mcgehee, H. Prall, and G. Dennler, “Organic solar cells with carbon nanotube network electrodes,” *Appl. Phys. Lett.*, vol. 88, p. 233506, 2006.

[19] S. J. Tans, A. R. M. Verschueren, and C. Dekker, “Room-temperature transistor based on a single carbon nanotube,” *Nature*, vol. 393, no. 7, pp. 49–52, 1998.

[20] M. H. Yang, K. B. K. Teo, W. I. Wilne, and D. G. Hasko, “Carbon nanotube Schottky diode and directionally dependent field-effect transistor using asymmetrical contacts,” *Appl. Phys. Lett.*, vol. 87, no. August 2005, p. 253116, 2005.

[21] N. Sinha, J. Ma, and J. T. W. Yeow, “Carbon Nanotube-Based Sensors,” *J. Nanosci. Nanotechnol.*, vol. 6, no. 3, pp. 573–590, 2006.

[22] B. Brett, L. Allen, P. D. Kichambare, and A. Star, “Field-Effect-Transistor-Based Biosensors **,” *Adv. Mater.*, vol. 19, pp. 1439–1451, 2007.

[23] N. Rouhi, D. Jain, and P. J. Burke, “High-Performance Semiconducting Nanotube Inks : Progress and Prospects,” *ACS Nano*, vol. 5, no. 11, pp. 8471–8487, 2011.

[24] Z. Spitalsky, D. Tasis, K. Papagelis, and C. Galiotis, “Carbon nanotube-polymer composites: Chemistry, processing, mechanical and electrical properties,” *Prog. Polym. Sci.*, vol. 35, no. 3, pp. 357–401, 2010.

[25] X. Sun, H. Sun, H. Li, and H. Peng, “Developing polymer composite materials:

Carbon nanotubes or graphene?," *Adv. Mater.*, vol. 25, no. 37, pp. 5153–5176, 2013.

[26] W. Khan, R. Sharma, and P. Saini, "Carbon Nanotube-Based Polymer Composites : Synthesis , Properties and Applications," in *Carbon Nanotubes: Current Progress of Their Polymer Composites*, INTECH, 2016, pp. 1–46.

[27] D. Kim, Y. Kim, K. Choi, J. C. Grunlan, and C. Yu, "Improved thermoelectric behavior of nanotube-filled polymer composites with poly(3,4-ethylenedioxythiophene) poly(styrenesulfonate)," *ACS Nano*, vol. 4, no. 1, pp. 513–523, 2010.

[28] T. G. Novak *et al.*, "Low-Cost Black Phosphorus Nanofillers for Improved Thermoelectric Performance in PEDOT:PSS Composite Films," *ACS Appl. Mater. Interfaces*, vol. 10, no. 21, pp. 17957–17962, 2018.

[29] F.-P. Du *et al.*, "PEDOT:PSS/graphene quantum dots films with enhanced thermoelectric properties via strong interfacial interaction and phase separation," *Sci. Rep.*, vol. 8, p. 6441, 2018.

[30] Q. Yao, L. Chen, W. Zhang, S. Liufu, and X. Chen, "Enhanced thermoelectric performance of single-walled carbon nanotubes/polyaniline hybrid nanocomposites," *ACS Nano*, vol. 4, no. 4, pp. 2445–2451, 2010.

[31] C. Yu, Y. S. Kim, D. Kim, and J. C. Grunlan, "Thermoelectric behavior of segregated-network polymer nanocomposites," *Nano Lett.*, vol. 8, no. 12, pp. 4428–4432, 2008.

[32] T. Ramanathan *et al.*, "Functionalized graphene sheets for polymer nanocomposites," *Nat. Nanotechnol.*, vol. 3, no. 6, pp. 327–331, 2008.

[33] X. Zhang *et al.*, "Poly(vinyl alcohol)/SWNT composite film," *Nano Lett.*, vol. 3, no. 9, pp. 1285–1288, 2003.

[34] K. G. Dassios and C. Galiotis, "Polymer-nanotube interaction in MWCNT/poly(vinyl alcohol) composite mats," *Carbon*, vol. 50, no. 11, pp. 4291–4294, 2012.

[35] Y. Chen, M. He, B. Liu, G. C. Bazan, J. Zhou, and Z. Liang, "Bendable n-Type Metallic Nanocomposites with Large Thermoelectric Power Factor," *Adv. Mater.*, vol. 29, no. 4, p. 1604752, 2017.

[36] P. Verma, P. Saini, R. S. Malik, and V. Choudhary, "Excellent electromagnetic interference shielding and mechanical properties of high loading carbon-nanotubes/polymer composites designed using melt recirculation equipped twin-screw extruder," *Carbon*, vol. 89, pp. 308–317, 2015.

[37] L. Teresa and M. Gámez, "Doctorado en Polímeros y Biopolímeros," *J. Polym. Sci.*, vol. 45, no. April, pp. 2007–2009, 2007.

[38] H. Huang, C. Liu, Y. Wu, and S. Fan, "Aligned carbon nanotube composite films for thermal management," *Adv. Mater.*, vol. 17, no. 13, pp. 1652–1656, 2005.

[39] K. Kobashi, S. Ata, T. Yamada, D. N. Futaba, M. Yumura, and K. Hata, "A dispersion strategy: Dendritic carbon nanotube network dispersion for advanced

composites," *Chem. Sci.*, vol. 4, no. 2, pp. 727–733, 2013.

[40] X. Zhao, Q. Zhang, D. Chen, and P. Lu, "Enhanced mechanical properties of graphene-based polyvinyl alcohol composites," *Macromolecules*, vol. 43, no. 5, pp. 2357–2363, 2010.

[41] N. Rouhi *et al.*, "Terahertz graphene optics," *Nano Res.*, vol. 5, no. 10, pp. 667–678, 2012.

[42] T. Low and P. Avouris, "Graphene plasmonics for terahertz to mid-infrared applications," *ACS Nano*, vol. 8, no. 2, pp. 1086–1101, 2014.

[43] A. B. Kuzmenko, E. Van Heumen, F. Carbone, and D. Van Der Marel, "Universal optical conductance of graphite," *Phys. Rev. Lett.*, vol. 100, no. 11, pp. 2–5, 2008.

[44] J. Horng *et al.*, "Drude conductivity of Dirac fermions in graphene," *Phys. Rev. B - Condens. Matter Mater. Phys.*, vol. 83, no. 16, pp. 1–5, 2011.

[45] S. Yuan, R. Roldán, H. De Raedt, and M. I. Katsnelson, "Optical conductivity of disordered graphene beyond the Dirac cone approximation," *Phys. Rev. B*, vol. 84, no. 19, pp. 1–11, 2011.

[46] T. Kampfrath *et al.*, "Mechanism of the far-infrared absorption of carbon-nanotube films," *Phys. Rev. Lett.*, vol. 101, no. 26, pp. 1–4, 2008.

[47] A. Ugawa, A. G. Rinzler, and D. B. Tanner, "Far-infrared gaps in single-wall carbon nanotubes," *Phys. Rev. B*, vol. 60, no. 16, pp. R11305–R11308, 1999.

[48] Z. Liu *et al.*, "Plasmonic nanoantenna arrays for the visible," *Metamaterials*, vol. 2,

no. 1, pp. 45–51, 2008.

[49] J. C. Blancon *et al.*, “Direct measurement of the absolute absorption spectrum of individual semiconducting single-wall carbon nanotubes,” *Nat. Commun.*, vol. 4, 2013.

[50] Y. Wang, G. Duan, L. Zhang, L. Ma, X. Zhao, and X. Zhang, “Terahertz Dispersion Characteristics of Super-aligned Multi-walled Carbon Nanotubes and Enhanced Transmission through Subwavelength Apertures,” *Sci. Rep.*, vol. 8, no. 1, pp. 1–10, 2018.

[51] X. He *et al.*, “Carbon nanotube terahertz detector,” *Nano Lett.*, vol. 14, no. 7, pp. 3953–3958, 2014.

[52] J. Lehman, A. Sanders, L. Hanssen, B. Wilthan, J. Zeng, and C. Jensen, “Very black infrared detector from vertically aligned carbon nanotubes and electric-field poling of lithium tantalate,” *Nano Lett.*, vol. 10, no. 9, pp. 3261–3266, 2010.

[53] K. Mizuno *et al.*, “A black body absorber from vertically aligned single-walled carbon nanotubes.,” *PNAS*, vol. 106, no. 15, pp. 6044–6047, 2009.

[54] Y. B. Tang *et al.*, “Vertically Aligned p-Type Single-Crystalline GaN Nanorod Arrays on n-Type Si for Heterojunction,” *Nano Lett.*, vol. 8, no. 12, pp. 4191–4195, 2008.

[55] Z. Yin *et al.*, “Extremely Black Vertically Aligned Carbon Nanotube Arrays for Solar Steam Generation,” *ACS Appl. Mater. Interfaces*, vol. 9, no. 34, pp. 28596–

28603, 2017.

[56] “http://www.jondetech.se/background-of-thermopiles/ http://www.mn.uio.no/fysikk/english/research/projects/bate/thermoelectricity/.” .

[57] J. P. Heremans, “Low-dimensional thermoelectricity,” *Acta Phys. Pol. A*, vol. 108, no. 4 PART 1, pp. 609–634, 2005.

[58] G. J. Snyder and E. S. Toberer, “Complex thermoelectric materials.,” *Nat. Mater.*, vol. 7, no. 2, pp. 105–14, 2008.

[59] V. W. Scarola and G. D. Mahan, “Phonon drag effect in single-walled carbon nanotubes,” *Phys. Rev. B - Condens. Matter Mater. Phys.*, vol. 66, no. 20, pp. 2054051–2054057, 2002.

[60] J. Vavro *et al.*, “Thermoelectric Power of [Formula presented]-Doped Single-Wall Carbon Nanotubes and the Role of Phonon Drag,” *Phys. Rev. Lett.*, vol. 90, no. 6, p. 4, 2003.

[61] M. S. Dresselhaus, “Solid State Physics Part I: Transport Properties of Solids,” *Lect. Course*, 2001.

[62] N. D. M. Neil W. Ashcroft, *Solid State Physics*. Brooks Cole; 1 edition (Jan. 2 1976), 1976.

[63] G. Chen, *Nanoscale energy transport and conversion: a parallel treatment of electrons, molecules, phonons, and photons*. Oxford University Press, 2005.

[64] L. Yan, M. Shao, H. Wang, D. Dudis, A. Urbas, and B. Hu, “High seebeck effects

from hybrid metal/polymer/metal thin-film devices," *Adv. Mater.*, vol. 23, no. 35, pp. 4120–4124, 2011.

[65] B. Poudel *et al.*, "High-thermoelectric performance of nanostructured bismuth antimony telluride bulk alloys.," *Science*, vol. 320, no. 5876, pp. 634–8, 2008.

[66] J. P. Heremans and M. S. Dresselhaus, "Chapter 27 Low-Dimensional Thermoelectricity," in *NANOMATERIALS HANDBOOK*, 2006, p. 741.

[67] A. Mehdizadeh, M. Zebarjadi, J. He, and T. M. Tritt, "Thermoelectric power factor : Enhancement mechanisms and strategies for higher performance thermoelectric materials," *Mater. Sci. Eng. R*, vol. 97, pp. 1–22, 2015.

[68] M. S. Dresselhaus *et al.*, "New directions for low-dimensional thermoelectric materials," *Adv. Mater.*, vol. 19, no. 8, pp. 1043–1053, 2007.

[69] L. D. Hicks, T. C. Harman, and M. S. Dresselhaus, "Use of quantum-well superlattices to obtain a high figure of merit from nonconventional thermoelectric materials," *Appl. Phys. Lett.*, vol. 63, no. 23, p. 3230, 1993.

[70] Y. Zhang, P. Kim, M. Y. Han, and O. Barbaros, "Energy Band-Gap Engineering of Graphene Nanoribbons," *Phys. Rev. Lett.*, vol. 98, no. MAY, p. 206805, 2007.

[71] T. Koga, X. Sun, S. B. Cronin, and M. S. Dresselhaus, "Carrier pocket engineering to design superior thermoelectric materials using GaAs / AlAs superlattices," *Appl. Phys. Lett.*, vol. 73, no. 20, p. 2950, 1998.

[72] Y. Chen, Y. Zhao, and Z. Liang, "Solution processed organic thermoelectrics:

towards flexible thermoelectric modules," *Energy Environ. Sci.*, vol. 8, no. 2, pp. 401–422, 2015.

[73] M. He, F. Qiu, and Z. Lin, "Towards high-performance polymer-based thermoelectric materials," *Energy Environ. Sci.*, vol. 6, no. 5, pp. 1352–1361, 2013.

[74] T. Zhu, Y. Liu, C. Fu, J. P. Heremans, J. G. Snyder, and X. Zhao, "Compromise and Synergy in High-Efficiency Thermoelectric Materials," *Adv. Mater.*, vol. 29, no. 14, 2017.

[75] B. B. Lahiri, S. Bagavathiappan, T. Jayakumar, and J. Philip, "Medical applications of infrared thermography: A review," *Infrared Phys. Technol.*, vol. 55, no. 4, pp. 221–235, 2012.

[76] M. Zhang and J. Yeow, "Nanotechnology-Based Terahertz Biological Sensing," *IEEE Nanotechnol. Mag.*, vol. 10, no. 3, pp. 30–38, 2016.

[77] A. González *et al.*, "Pedestrian Detection at Day / Night Time with Visible and FIR Cameras : A Comparison," *Sensors*, vol. 16, p. 820, 2016.

[78] I. Duling and D. Zimdars, "Terahertz imaging: Revealing hidden defects," *Nat. Photonics*, vol. 3, no. 11, pp. 630–632, 2009.

[79] Z. Liu, H. Ukida, P. Ramuhalli, and K. Niel, *Integrated Imaging and Vision Techniques for Industrial Inspection*. Springer, New York, NY, 2015.

[80] J. Bullock *et al.*, "Polarization-resolved black phosphorus/molybdenum disulfide mid-wave infrared photodiodes with high detectivity at room temperature," *Nat.*

Photonics, vol. 12, pp. 601–607, 2018.

[81] X. Tang, M. M. Ackerman, and P. Guyot-Sionnest, "Thermal Imaging with Plasmon Resonance Enhanced HgTe Colloidal Quantum Dot Photovoltaic Devices," *ACS Nano*, vol. 12, no. 7, pp. 7362–7370, 2018.

[82] X. Tang, M. M. Ackerman, M. Chen, and P. Guyot-Sionnest, "Dual-band infrared imaging using stacked colloidal quantum dot photodiodes," *Nat. Photonics*, vol. 13, pp. 277–282, 2019.

[83] H. C. Liu, *Quantum Well Infrared Photodetectors*. Springer Series in optical sciences, 2007.

[84] D. Palaferri *et al.*, "Room-temperature nine-μm-wavelength photodetectors and GHz-frequency heterodyne receivers," *Nature*, vol. 556, no. 7699, pp. 85–88, 2018.

[85] M. E. Itkis, F. Borondics, A. Yu, and R. C. Haddon, "Bolometric Infrared Photoresponse of Suspended Single-Walled Carbon Nanotube Films," *Science*, vol. 312, pp. 413–416, 2006.

[86] A. El Fatimy, R. L. Myers-Ward, A. K. Boyd, K. M. Daniels, D. K. Gaskill, and P. Barbara, "Epitaxial graphene quantum dots for high-performance terahertz bolometers," *Nat. Nanotechnol.*, vol. 11, no. January, pp. 335–338, 2016.

[87] Z. L. Huang, M. Gao, Z. C. Yan, T. S. Pan, F. Y. Liao, and Y. Lin, "Flexible infrared detectors based on p-n junctions of multi-walled carbon nanotubes," *Nanoscale*, vol. 8, no. 18, pp. 9592–9599, 2016.

[88] X. He *et al.*, “Carbon nanotube terahertz detector,” *Nano Lett.*, vol. 14, no. 7, pp. 3953–3958, 2014.

[89] K. W. Mauser *et al.*, “Resonant thermoelectric nanophotonics,” *Nat. Nanotechnol.*, vol. 12, pp. 770–775, 2017.

[90] D. Suzuki, S. Oda, and Y. Kawano, “A flexible and wearable terahertz scanner,” *Nat. Photonics*, vol. 10, no. November, pp. 809–813, 2016.

[91] X. Cai *et al.*, “Sensitive room-temperature terahertz detection via the photothermoelectric effect in graphene,” *Nat. Nanotechnol.*, vol. 9, no. 10, pp. 814–819, 2014.

[92] M. Zhang and J. T. W. Yeow, “Flexible Polymer - Carbon Nanotube Composite with High Response Stability for Wearable Thermal Imaging,” *ACS Appl. Mater. Interfaces*, vol. 10, no. 31, pp. 26604–26609, 2018.

[93] L. Yang *et al.*, “Efficient photovoltage multiplication in carbon nanotubes,” *Nat. Photonics*, vol. 5, pp. 672–676, 2011.

[94] F. Wang *et al.*, “High Conversion Efficiency Carbon Nanotube-Based Barrier-Free Bipolar-Diode Photodetector,” *ACS Nano*, vol. 10, no. 10, pp. 9595–9601, 2016.

[95] Q. Zeng *et al.*, “Carbon nanotube arrays based high-performance infrared photodetector [Invited],” *Opt. Mater. Express*, vol. 2, no. 6, p. 839, 2012.

[96] S. Nanot *et al.*, “Broadband, polarization-sensitive photodetector based on optically-thick films of macroscopically long, dense, and aligned carbon nanotubes.,” *Sci.*

Rep., vol. 3, p. 1335, 2013.

[97] B. C. St-Antoine, D. Ménard, and R. Martel, "Single-walled carbon nanotube thermopile for broadband light detection," *Nano Lett.*, vol. 11, no. 2, pp. 609–613, 2011.

[98] X. Lu, P. Jiang, and X. Bao, "Phonon-enhanced photothermoelectric effect in SrTiO3 ultra-broadband photodetector," *Nat. Commun.*, vol. 10, no. 1, p. 138, 2019.

[99] X. Deng, Y. Wang, Z. Zhao, Z. Chen, and J.-L. Sun, "Terahertz-induced photothermoelectric response in graphene-metal contact structures," *J. Phys. D. Appl. Phys.*, vol. 49, no. 42, p. 425101, 2016.

[100] C. Hu, C. Liu, L. Chen, C. Meng, and S. Fan, "A Demo Opto-electronic Power Source Based on Single-Walled Carbon Nanotube Sheets," *ACS Nano*, vol. 4, no. 8, pp. 4701–4706, 2010.

[101] S. O. Kasap, *Optoelectronics and Photonics*. 2013.

[102] A. A. Balandin, "Low-frequency 1/f noise in graphene devices," *Nat. Nanotechnol.*, vol. 8, no. 8, pp. 549–555, 2013.

[103] R. Tarkiainen, L. Roschier, M. Ahlskog, M. Paalanen, and P. Hakonen, "Low-frequency current noise and resistance fluctuations in multiwalled carbon nanotubes," *Phys. E Low-Dimensional Syst. Nanostructures*, vol. 28, no. 1, pp. 57–65, 2005.

[104] H. Dai, "Carbon nanotubes: Synthesis, integration, and properties," *Acc. Chem. Res.*,

vol. 35, no. 12, pp. 1035–1044, 2002.

[105] M. Kumar and Y. Ando, “Chemical Vapor Deposition of Carbon Nanotubes: A Review on Growth Mechanism and Mass Production,” *J. Nanosci. Nanotechnol.*, vol. 10, no. 6, pp. 3739–3758, 2010.

[106] R. Zhang, Y. Zhang, Q. Zhang, H. Xie, W. Qian, and F. Wei, “Growth of half-meter long carbon nanotubes based on Schulz-Flory distribution,” *ACS Nano*, vol. 7, no. 7, pp. 6156–6161, 2013.

[107] Y. Zhang *et al.*, “Tailoring the morphology of carbon nanotube arrays: From spinnable forests to undulating foams,” *ACS Nano*, vol. 3, no. 8, pp. 2157–2162, 2009.

[108] K. Hata, D. N. Futaba, K. Mizuno, and T. Namai, “Water-Assisted Highly Efficient Synthesis of Impurity-Free Single-Walled Carbon Nanotubes,” *Science*, vol. 306, no. November, pp. 1362–1365, 2004.

[109] M. MARCHENA, D. JANNER, T. L. CHEN, V. FINAZZI, and V. PRUNERI, “Low temperature direct growth of graphene patterns on flexible glass substrates catalysed by a sacrificial ultrathin Ni film,” *Opt. Mat. Express*, vol. 6, no. 8, pp. 2487–2507, 2016.

[110] J. Masuda and J. M. Torkelson, “Dispersion and major property enhancements in polymer/multiwall carbon nanotube nanocomposites via solid-state shear pulverization followed by melt mixing,” *Macromolecules*, vol. 41, no. 16, pp. 5974–

5977, 2008.

[111] S. COSTA, E. BOROWIAK-PALEN, M. KRUSZYŃSKA, A. BACHMATIUK, and R. J. KALEŃCZUK, "Characterization of carbon nanotubes by Raman spectroscopy," *Mater. Sci.*, vol. 26, no. 2, p. 433, 2008.

[112] M. Nakano, Y. Nonoguchi, T. Nakashima, and T. Kawai, "Flexible thermoelectric rubber polymer composites based on single-walled carbon nanotubes," *Jpn. J. Appl. Phys.*, vol. 54, no. 4S, p. 04DN03, 2015.

[113] N. S. Alghunaim, "Optimization and spectroscopic studies on carbon nanotubes/PVA nanocomposites," *Results Phys.*, vol. 6, pp. 456–460, 2016.

[114] D. Yoo, J. Kim, and J. H. Kim, "Direct synthesis of highly conductive poly(3,4-ethylenedioxythiophene):Poly(4-styrenesulfonate) (PEDOT:PSS)/graphene composites and their applications in energy harvesting systems," *Nano Res.*, vol. 7, no. 5, pp. 717–730, 2014.

[115] J. Zhang and X. S. Zhao, "Conducting polymers directly coated on reduced graphene oxide sheets as high-performance supercapacitor electrodes," *J. Phys. Chem. C*, vol. 116, no. 9, pp. 5420–5426, 2012.

[116] T. Chen *et al.*, "Ultra high permittivity and significantly enhanced electric field induced strain in PEDOT:PSS-RGO@PU intelligent shape-changing electro-active polymers," *RSC Adv.*, vol. 4, no. 109, pp. 64061–64067, 2014.

[117] M. Long *et al.*, "Room temperature high-detectivity mid-infrared photodetectors

based on black arsenic phosphorus," *Sci. Adv.*, vol. 3, no. 6, p. e1700589, 2017.

[118] X. Chen *et al.*, "Widely tunable black phosphorus mid-infrared photodetector," *Nat. Commun.*, vol. 8, no. 1, pp. 1672–1678, 2017.

[119] U. Sassi *et al.*, "Graphene-based, mid-infrared, room-temperature pyroelectric bolometers with ultrahigh temperature coefficient of resistance," *Nat. Commun.*, vol. 8, p. 1433, 2016.

[120] V. Shautsova *et al.*, "Plasmon induced thermoelectric effect in graphene," *Nat. Commun.*, vol. 9, p. 5190, 2018.

[121] X. Yu, Z. Dong, J. K. W. Yang, and Q. J. Wang, "Room-temperature mid-infrared photodetector in all-carbon graphene nanoribbon-C60 hybrid nanostructure," *Optica*, vol. 3, no. 9, pp. 979–984, 2016.

[122] L. W. Chou, N. Shin, S. V. Sivaram, and M. A. Filler, "Tunable mid-infrared localized surface plasmon resonances in silicon nanowires," *J. Am. Chem. Soc.*, vol. 134, no. 39, pp. 16155–16158, 2012.

[123] Y. Cao *et al.*, "Ultra-Broadband Photodetector for the Visible to Terahertz Range by Self-Assembling Reduced Graphene Oxide-Silicon Nanowire Array Heterojunctions," *Small*, vol. 10, no. 12, pp. 2345–2351, 2014.

[124] J. Jean *et al.*, "ZnO nanowire arrays for enhanced photocurrent in PbS quantum dot solar cells," *Adv. Mater.*, vol. 25, no. 20, pp. 2790–2796, 2013.

[125] J. Walia *et al.*, "Enhanced photothermal conversion in vertically oriented gallium

arsenide nanowire arrays," *Nano Lett.*, vol. 14, no. 10, pp. 5820–5826, 2014.

[126] J. Svensson, N. Anttu, N. Vainorius, B. M. Borg, and L. E. Wernersson, "Diameter-dependent photocurrent in InAsSb nanowire infrared photodetectors," *Nano Lett.*, vol. 13, no. 4, pp. 1380–1385, 2013.

[127] N. Selvakumar, S. B. Krupanidhi, and H. C. Barshilia, "Carbon nanotube-based tandem absorber with tunable spectral selectivity: Transition from near-perfect blackbody absorber to solar selective absorber," *Adv. Mater.*, vol. 26, no. 16, pp. 2552–2557, 2014.

[128] Z. Yang, L. Ci, J. A. Bur, S. Lin, and P. M. Ajayan, "Experimental Observation of an Extremely Dark Material Made By a Low-Density Nanotube Array," *Nano Lett.*, vol. 8, no. 2, pp. 446–451, 2008.

[129] K. J. Erikson *et al.*, "Figure of Merit for Carbon Nanotube Photothermoelectric Detectors," *ACS Nano*, vol. 9, no. 12, pp. 11618–11627, 2015.

[130] L. Viti *et al.*, "Black Phosphorus Terahertz Photodetectors," *Adv. Mater.*, vol. 27, p. 5567, 2015.

[131] K. Haddadi *et al.*, "Microwave and Millimeter Wave Properties of Vertically-Aligned Single Wall Carbon Nanotubes Films," *J. Electron. Mater.*, vol. 45, no. 5, pp. 2433–2441, 2016.

[132] H. Lyeo, H. Lyeo, A. A. Khajetoorians, L. Shi, and K. P. Pipe, "Profiling the Thermoelectric Power of Semiconductor Junctions with Nanometer Resolution,"

Science, vol. 816, no. 2004, pp. 816–818, 2009.

[133] S. E. Shafraniuk, "Chapter 3 - Graphene thermoelectric transducers," in *Thermoelectricity and Heat Transport in Graphene and Other 2D Nanomaterials*, S. E. Shafraniuk, Ed. Elsevier, 2018, pp. 125–185.

[134] X. Zhang, H. Choi, A. Datta, and X. Li, "Design, fabrication and characterization of metal embedded thin film thermocouples with various film thicknesses and junction sizes," *J. Micromechanics Microengineering*, vol. 16, no. 5, pp. 900–905, 2006.

[135] K. L. Chorra, *Thin Film Phenomena*. McGraw-Hill Book Company, New York, 1969.

[136] Y. Sungtaek Ju and U. Ghoshal, "Study of interface effects in thermoelectric microrefrigerators," *J. Appl. Phys.*, vol. 88, no. 7, p. 4135, 2002.

[137] L. W. da Silva and M. Kaviany, "Micro-thermoelectric cooler: Interfacial effects on thermal and electrical transport," *Int. J. Heat Mass Transf.*, vol. 47, no. 10–11, pp. 2417–2435, 2004.

[138] F. Hao, D. N. Fang, and J. Y. Li, "Thermoelectric transport in heterogeneous medium: the role of thermal boundary resistance," *Eur. Phys. J. Appl. Phys.*, vol. 58, no. 3, p. 30901, 2012.

[139] S. Wang, T. Xie, and H. Xie, "Experimental study of the effects of the thermal contact resistance on the performance of thermoelectric generator," *Appl. Therm. Eng.*, vol. 130, pp. 847–853, 2018.

[140] Q. Li, C. Liu, and S. Fan, “Thermal boundary resistances of carbon nanotubes in contact with metals and polymers,” *Nano Lett.*, vol. 9, no. 11, pp. 3805–3809, 2009.

[141] A. Zienert, J. Schuster, and T. Gessner, “Metallic carbon nanotubes with metal contacts: Electronic structure and transport,” *Nanotechnology*, vol. 25, no. 42, 2014.

[142] Y. Matsuda, W. Q. Deng, and W. A. Goddard, “Contact resistance properties between nanotubes and various metals from quantum mechanics,” *J. Phys. Chem. C*, vol. 111, no. 29, pp. 11113–11116, 2007.

[143] J. Zhang, A. C. E. Chia, and R. R. Lapierre, “Low resistance indium tin oxide contact to n-GaAs nanowires,” *Semicond. Sci. Technol.*, vol. 29, no. 5, 2014.

[144] S. J. Gibson *et al.*, “Tapered InP nanowire arrays for efficient broadband high-speed single-photon detection,” *Nat. Nanotechnol.*, 2019.

[145] Y.-S. Lai, C.-Y. Tsai, C.-K. Chang, C.-Y. Huang, V. K. S. Hsiao, and Y. O. Su, “Photothermoelectric Effects in Nanoporous Silicon,” *Adv. Mater.*, vol. 28, no. 1, p. 2644, 2016.

[146] A. Zubair *et al.*, “Carbon nanotube woven textile photodetector,” *Phys. Rev. Mater.*, vol. 2, no. 1, p. 015201, 2018.

[147] T. J. Echtermeyer *et al.*, “Photothermoelectric and photoelectric contributions to light detection in metal-graphene-metal photodetectors.,” *Nano Lett.*, vol. 14, no. 7, pp. 3733–42, 2014.

[148] X. He, F. Léonard, and J. Kono, “Uncooled Carbon Nanotube Photodetectors,” *Adv.*

Opt. Mater., vol. 3, no. 8, pp. 989–1011, 2015.

[149] R. Gade and T. B. Moeslund, "Thermal cameras and applications: A survey," *Mach. Vis. Appl.*, vol. 25, no. 1, pp. 245–262, 2014.

[150] F. P. G. De Arquer, A. Armin, P. Meredith, and E. H. Sargent, "Solution-processed semiconductors for next-generation photodetectors," *Nat. Rev. Mater.*, vol. 2, p. 16100, 2017.

[151] M. S. Vitiello *et al.*, "Room-temperature terahertz detectors based on semiconductor nanowire field-effect transistors," *Nano Lett.*, vol. 12, no. 1, pp. 96–101, 2012.

[152] A. L. Hsu *et al.*, "Graphene-Based Thermopile for Thermal Imaging Applications," *Nano Lett.*, vol. 15, no. 11, pp. 7211–7216, 2015.

[153] L. Wang *et al.*, "Toward Sensitive Room-Temperature Broadband Detection from Infrared to Terahertz with Antenna-Integrated Black Phosphorus Photoconductor," *Adv. Funct. Mater.*, vol. 27, p. 1604414, 2017.

[154] M. Freitag, T. Low, and P. Avouris, "Increased responsivity of suspended graphene photodetectors," *Nano Lett.*, vol. 13, no. 4, pp. 1644–1648, 2013.

[155] X. Xu, N. M. Gabor, J. S. Alden, A. M. Van Der Zande, and P. L. McEuen, "Photo-thermoelectric effect at a graphene interface junction," *Nano Lett.*, vol. 10, no. 2, pp. 562–566, 2010.

[156] N. Guo *et al.*, "High-quality infrared imaging with graphene photodetectors at room temperature," *Nanoscale*, vol. 8, no. 35, pp. 16065–16072, 2016.

[157] J. H. Koo *et al.*, "Wearable Electrocardiogram Monitor Using Carbon Nanotube Electronics and Color-Tunable Organic Light-Emitting Diodes," *ACS Nano*, vol. 11 (10), pp. 10032–10041, 2017.

[158] A. Miyamoto *et al.*, "Inflammation-free, gas-permeable, lightweight, stretchable on-skin electronics with nanomeshes," *Nat. Nanotechnol.*, vol. 12, no. July, p. 907, 2017.

[159] C. Wang *et al.*, "Carbonized Silk Fabric for Ultrastretchable, Highly Sensitive, and Wearable Strain Sensors," *Adv. Mater.*, vol. 28, pp. 6640–6648, 2016.

[160] G. Chen, M. S. Dresselhaus, G. Dresselhaus, J.-P. Fleurial, and T. Caillat, "Recent developments in thermoelectric materials," *Int. Mater. Rev.*, vol. 48, no. 1, pp. 45–66, 2003.

[161] R. Venkatasubramanian, E. Siivola, T. Colpitts, and B. O'Quinn, "Thin-film thermoelectric devices with high room-temperature figures of merit," *Nature*, vol. 413, no. 6856, pp. 597–602, 2001.

[162] H. J. Salavagione, A. M. Díez-Pascual, E. Lázaro, S. Vera, and M. a. Gómez-Fatou, "Chemical sensors based on polymer composites with carbon nanotubes and graphene: the role of the polymer," *J. Mater. Chem. A*, vol. 2, no. 35, pp. 14289–14328, 2014.

[163] D. Tasis *et al.*, "Chemistry of Carbon Nanotubes Chemistry of Carbon Nanotubes," *Chem. Rev.*, vol. 106, no. February, pp. 1105–1136, 2006.

[164] A. Bianco, K. Kostarelos, and M. Prato, “Making carbon nanotubes biocompatible and biodegradable,” *Chem. Commun.*, vol. 47, no. 37, pp. 10182–8, 2011.

[165] B. K. Sarker, M. Arif, and S. I. Khondaker, “Near-infrared photoresponse in single-walled carbon nanotube/polymer composite films,” *Carbon*, vol. 48, no. 5, pp. 1539–1544, 2010.

[166] M. Piao *et al.*, “Increasing the thermoelectric power generated by composite films using chemically functionalized single-walled carbon nanotubes,” *Carbon*, vol. 62, pp. 430–437, 2013.

[167] H. Song, C. Liu, J. Xu, Q. Jiang, and H. Shi, “Fabrication of a layered nanostructure PEDOT:PSS/SWCNTs composite and its thermoelectric performance,” *RSC Adv.*, vol. 3, no. 44, p. 22065, 2013.

[168] P. Miaudet *et al.*, “Thermo-electrical properties of PVA-nanotube composite fibers,” *Polymer*, vol. 48, no. 14, pp. 4068–4074, 2007.

[169] W. Zhou *et al.*, “High-performance and compact-designed flexible thermoelectric modules enabled by a reticulate carbon nanotube architecture,” *Nat. Commun.*, vol. 8, p. 14886, 2017.

[170] M. Tonga *et al.*, “Thermoelectric Enhancement by Compositing Carbon Nanotubes into Iodine-Doped Poly[2-methoxy-5-(2-ethylhexyloxy)-1,4-phenylenevinylene],” *ACS Appl. Mater. Interfaces*, vol. 9, no. 10, pp. 8975–8984, 2017.

[171] W. Chen, X. Tao, P. Xue, and X. Cheng, “Enhanced mechanical properties and

morphological characterizations of poly(vinyl alcohol)-carbon nanotube composite films," *Appl. Surf. Sci.*, vol. 252, no. 5, pp. 1404–1409, 2005.

[172] J. Xu *et al.*, "Highly stretchable polymer semiconductor films through the nanoconfinement effect," *Science*, vol. 355, no. January, pp. 59–64, 2017.

[173] X. Yang, A. Vorobiev, A. Generalov, M. A. Andersson, and J. Stake, "A flexible graphene terahertz detector," *Appl. Phys. Lett.*, vol. 111, no. 2, pp. 2–6, 2017.

[174] Y. Liu *et al.*, "Room Temperature Broadband Infrared Carbon Nanotube Photodetector with High Detectivity and Stability," *Adv. Opt. Mater.*, vol. 4, no. 2, pp. 238–245, 2016.

[175] C. Yu, K. Choi, L. Yin, and J. C. Grunlan, "Light-Weight Flexible Carbon Nanotube Based Organic Composites with Large Thermoelectric Power Factors," *ACS Nano*, vol. 5, no. 10, pp. 7885–7892, 2011.

[176] C. Meng, C. Liu, and S. Fan, "A promising approach to enhanced thermoelectric properties using carbon nanotube networks," *Adv. Mater.*, vol. 22, no. 4, pp. 535–539, 2010.

[177] N. Luo, Y. Huang, J. Liu, S.-C. Chen, C. P. Wong, and N. Zhao, "Hollow-Structured Graphene-Silicone-Composite-Based Piezoresistive Sensors: Decoupled Property Tuning and Bending Reliability," *Adv. Mater.*, vol. 11, p. 366, 2017.

[178] W. Honda, S. Harada, S. Ishida, T. Arie, S. Akita, and K. Takei, "High-Performance, Mechanically Flexible, and Vertically Integrated 3D Carbon Nanotube and

InGaZnO Complementary Circuits with a Temperature Sensor," *Adv. Mater.*, vol. 27, no. 32, pp. 4674–4680, 2015.

[179] L. Vicarelli *et al.*, "Graphene field-effect transistors as room-temperature terahertz detectors," *Nat. Mater.*, vol. 11, no. 10, pp. 865–871, 2012.

[180] M. Long *et al.*, "Room temperature high-detectivity mid-infrared photodetectors based on black arsenic phosphorus," *Sci. Adv.*, vol. 3, no. 6, 2017.

[181] J. Yan *et al.*, "Dual-gated bilayer graphene hot-electron bolometer," *Nat. Nanotechnol.*, vol. 7, no. 7, pp. 472–478, 2012.

[182] X. Yu *et al.*, "Narrow bandgap oxide nanoparticles coupled with graphene for high performance mid-infrared photodetection," *Nat. Commun.*, vol. 9, no. 1, p. 4299, 2018.

[183] S. Castilla *et al.*, "Fast and Sensitive Terahertz Detection Using an Antenna-Integrated Graphene pn Junction," *Nano Lett.*, vol. 19, p. 2765−2773, 2019.

[184] M. Badioli *et al.*, "Phonon-mediated mid-infrared photoresponse of graphene," *Nano Lett.*, vol. 14, no. 11, pp. 6374–6381, 2014.

[185] J. Wen *et al.*, "Ultra-broadband self-powered reduced graphene oxide photodetectors with annealing temperature-dependent responsivity," *Carbon*, vol. 153, pp. 274–284, 2019.

[186] Q. Guo *et al.*, "Efficient Electrical Detection of Mid-Infrared Graphene Plasmons at Room Temperature," *Nat. Mater.*, vol. 17, pp. 986–992, 2018.

[187] T. Wu *et al.*, “Fast Growth of Inch-sized Single Crystalline Graphene from a Controlled Single Nucleus on Cu-Ni Alloy,” *Nat. Mater.*, vol. 15, pp. 43–47, 2015.

[188] H. Kim and J. H. Ahn, “Graphene for flexible and wearable device applications,” *Carbon*, vol. 120, pp. 244–257, 2017.

[189] S. F. Leung *et al.*, “A Self-Powered and Flexible Organometallic Halide Perovskite Photodetector with Very High Detectivity,” *Adv. Mater.*, vol. 30, no. 8, pp. 1–8, 2018.

[190] G. Pace *et al.*, “All-organic and fully-printed semitransparent photodetectors based on narrow bandgap conjugated molecules,” *Adv. Mater.*, vol. 26, no. 39, pp. 6773–6777, 2014.

[191] H. Zhang *et al.*, “Transparent organic photodetector using a near-infrared absorbing cyanine dye,” *Sci. Rep.*, vol. 5, pp. 1–6, 2015.

[192] B. Kim, H. Shin, T. Park, H. Lim, and E. Kim, “NIR-sensitive poly(3,4-ethylenedioxyselenophene) derivatives for transparent photo-thermo-electric converters,” *Adv. Mater.*, vol. 25, no. 38, pp. 5483–5489, 2013.

[193] Z. Fan and J. Ouyang, “Thermoelectric Properties of PEDOT:PSS,” *Adv. Electron. Mater.*, vol. 1800769, pp. 1–23, 2019.

[194] M. Ibáñez *et al.*, “High-performance thermoelectric nanocomposites from nanocrystal building blocks,” *Nat. Commun.*, vol. 7, no. May 2015, p. 10766, 2016.

[195] B. T. McGrail, A. Sehirlioglu, and E. Pentzer, “Polymer composites for

thermoelectric applications," *Angew. Chemie - Int. Ed.*, vol. 54, no. 6, pp. 1710–1723, 2015.

[196] K. Suemori, Y. Watanabe, and S. Hoshino, "Carbon nanotube bundles/polystyrene composites as high-performance flexible thermoelectric materials," *Appl. Phys. Lett.*, vol. 106, no. 11, p. 113902, 2015.

[197] G. H. Kim, D. H. Hwang, and S. I. Woo, "Thermoelectric properties of nanocomposite thin films prepared with poly(3,4-ethylenedioxythiophene) poly(styrenesulfonate) and graphene," *Phys. Chem. Chem. Phys.*, vol. 14, no. 10, pp. 3530–3536, 2012.

[198] F. Li, K. Cai, S. Shen, and S. Chen, "Preparation and thermoelectric properties of reduced graphene oxide/PEDOT:PSS composite films," *Synth. Met.*, vol. 197, pp. 58–61, 2014.

[199] D. Suzuki, Y. Ochiai, and Y. Kawano, "Thermal Device Design for a Carbon Nanotube Terahertz Camera," *ACS Omega*, vol. 3, pp. 3540–3547, 2018.

[200] G. W. J. E. Hass, "Optical Constants and Reflectance and Transmittance of Evaporated Aluminium in the Visible and Ultraviolet," *J. Opt. Soc. Am.*, vol. 51, no. 7, pp. 719–722, 1961.

[201] Y. Wang *et al.*, "Ultrabroadband, Sensitive, and Fast Photodetection with Needle-Like EuBiSe 3 Single Crystal," *ACS Photonics*, vol. 6, no. 4, pp. 895–903, 2019.

[202] Y. Yao *et al.*, "High-responsivity mid-infrared graphene detectors with antenna-

enhanced photocarrier generation and collection," *Nano Lett.*, vol. 14, no. 7, pp. 3749–3754, 2014.

[203] J. A. Sarabia, M. A. Rol, P. Mendiola, and J. A. Madrid, "Circadian rhythm of wrist temperature in normal-living subjects. A candidate of new index of the circadian system," *Physiol. Behav.*, vol. 95, no. 4, pp. 570–580, 2008.

[204] A. Sano, R. W. Picard, and R. Stickgold, "Quantitative analysis of wrist electrodermal activity during sleep," *Int. J. Psychophysiol.*, vol. 94, no. 3, pp. 382–389, 2014.

[205] S. K. Youn and H. G. Park, "Morphological evolution of Fe-Mo bimetallic catalysts for diameter and density modulation of vertically aligned carbon nanotubes," *J. Phys. Chem. C*, vol. 117, no. 36, pp. 18657–18665, 2013.